

pubs.acs.org/CR Review

Single-Crystalline Anode Materials: Growth, Applications, Fabrication, and Recycling

Published as part of Chemical Reviews special issue "Single Crystal Materials for Energy Solutions: From Materials Chemistry to Manufacturing Science".

Dong Ju Lee, Qingyang Yin,* Dapeng Xu, and Zheng Chen*



Cite This: Chem. Rev. 2025, 125, 9332-9381

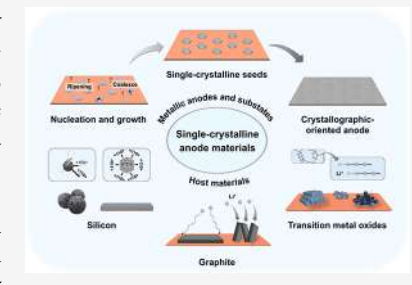


ACCESS

Metrics & More

Article Recommendations

ABSTRACT: Single-crystalline materials have attracted broad interest in advanced battery applications due to their inherent crystallographic characteristics. Their continuous, defect-free atomic arrangement contributes to improved interfacial stability, mechanical integrity, and charge transfer properties, ultimately leading to superior electrochemical performance compared to those of the polycrystalline counterparts. Despite their growing importance, a comprehensive review of single-crystalline anode materials has been lacking. In this review, we provide an overview of single-crystalline anode materials on their growth, applications, fabrications, and recycling for both metal and ion batteries. Starting from a theoretical understanding of electro-crystallization of metals, we discuss recent strategies for the growth and application of single-crystalline metals and substrates in various chemistries including



lithium, zinc, sodium, aluminum, and magnesium, as well as single-crystalline host materials such as silicon, graphite, and transition metal oxides, alongside their failure mechanisms and associated challenges. Lastly, we discuss the fabrication and recycling of single-crystalline anode materials for a closed-loop life cycle of batteries. This review aims to provide insight into the crystallographic understanding and design of single-crystalline anodes for advanced and sustainable next-generation batteries.

CONTENTS

. Introduction	9333
2. Crystal Nucleation, Incubation, and Growth	
Theories	9334
2.1. Nucleation	9334
2.1.1. Homogeneous Nucleation Theory	9334
2.1.2. Heterogeneous Nucleation Theory	9334
2.2. Incubation and Growth	9335
2.2.1. Classical Growth Theory	9335
2.2.2. Ostwald Ripening and Digestive Ripen-	
ing	9336
2.2.3. Coalescence	9336
2.3. Critical Determinants in Practical Electro-	
Crystallization	9337
2.3.1. Impact of Overpotential	9337
2.3.2. Substrate Effect	9337
2.3.3. Temperature Effect	9338
2.3.4. Pressure Effect	9339
8. Li Metal Anode	9339
3.1. Li Substrates for Li Crystal Growth	9339
3.1.1. Single-Crystalline Li: Growth and Facets	9339
3.1.2. Surface Effect on Li Crystal Growth	9340
3.1.3. Li-Alloy Substrates	9341
3.2. Li-Free Substrates for Li Crystal Growth	9343
3.2.1. Single-Crystalline Cu Substrate: Facets	9343

3.2.2. Single-Crystalline Cu Substrate: SEI	9345
3.2.3. Other Substrates	9345
3.3. Effect of Operation Conditions	9346
3.3.1. Current Density	9346
3.3.2. Temperature	9347
3.3.3. Pressure	9348
3.4. Impact of Electrolyte Systems on Li Crystal	
Growth	9349
3.4.1. Liquid Electrolyte	9349
3.4.2. Solid Electrolyte	9351
4. Zn Metal Anode	9351
4.1. Epitaxial Zn Growth on Textured Interlayer	9351
4.2. Zn Growth on Single-Crystalline Substrates	9352
4.2.1. Single-Crystalline Zn Substrate	9352
4.2.2. Single-Crystalline Cu Substrate	9354
4.3. Electrolyte Engineering	9355
4.3.1. Electrolyte-Facilitated Zn(002) Growth	9355

Received: April 14, 2025 Revised: August 23, 2025 Accepted: September 2, 2025 Published: September 29, 2025





4.3.2. Electrolyte-Facilitated Zn(101)/(100)	
Growth	9356
4.4. Effect of Operation Conditions	9356
5. Other Metal Anodes	9357
5.1. Na Metal Anade	9358
5.2. Al Metal Anode	9358
5.3. Mg Metal Anode	9358
6. Single-Crystalline Host Materials	9360
6.1. Si	9360
6.1.1. Single-Crystalline Si	9360
6.1.2. Crystal Plane-Dependent Structure Deg-	0266
radation	9360
6.1.3. Limitations and Prospects	9361
6.2. Graphite	9362
6.2.1. Crystal Structure of Graphite	9362
6.2.2. Single-Crystalline and Polycrystalline	0265
Graphite	9363
6.2.3. Toward Fast-Charging Single-Crystalline	0265
Graphite	9363
6.3. Transition Metal Oxides	9364
7. Fabrication and Recycling	9366
7.1. Fabrication of Single-Crystalline Anodes	9366
7.1.1. Accumulative Roll Bonding	9366
7.1.2. Annealing	9366
7.1.3. Electrolysis and Selective Etching	9367
7.2. Recycling of Single-Crystalline Anodes	9367
7.2.1. Degradation	9367
7.2.2. Separation	9367
7.2.3. Recycling	9367
8. Conclusion and Outlook	9368
Author Information	9369
Corresponding Authors	9369
Authors	9369
Author Contributions	9369
Notes	9369
Biographies	9369
Acknowledgments	9370
Abbreviations	9370
References	9370

1. INTRODUCTION

Single-crystalline materials make up a class of solids distinguished by their continuous and defect-free atomic arrangement throughout the entire structure. Unlike polycrystalline materials, which consist of multiple crystallographic textures separated by grain boundaries, single crystals offer superior mechanical, electrical, and optical properties due to the absence of these boundaries. These exceptional characteristics make them highly valuable for various technological applications, including semiconductors, lasers, and photonic devices. 3,4

Beyond their traditional applications, single-crystalline materials have gained significant interest in the field of energy storage, particularly in battery technology. In battery research, single-crystalline materials are typically defined on the scale of individual particles. For example, single-crystalline cathode materials have micron-sized intact primary particles with consistent lattice orientation that significantly enhances their structural stability, alleviating particle fracture and mechanical degradation during cycling. ⁵⁻⁷ This improved stability mitigates undesirable parasitic side reactions at the electrode—electrolyte interface, leading to improved electrochemical performance. ^{8,9} Additionally, some nanostructured electrode materials also

exhibit single-crystalline characteristics, where the significantly shortened ion diffusion pathways contribute to enhanced capacity and high-rate performance in batteries. These materials can be engineered into various forms, such as nanowires, nanotubes, and nanosheets, optimizing electrode functionality by adjusting surface energy and diffusion pathways. ^{10–13}

In the pursuit of advanced energy storage solutions, lithium metal batteries (LMBs) have gained significant attention as promising alternatives to conventional lithium-ion batteries (LIBs). Due to their substantially higher energy densities, LMBs are promising candidates for next-generation energy storage systems, with potential applications spanning portable electronics, electric vehicles, and the aviation and aerospace sectors. ^{14–16} In addition, alternative metal battery chemistries such as zinc (Zn), 17-19 sodium (Na), 20,21 aluminum (Al), 22,23 and magnesium (Mg)^{24,25} have also been explored due to their cost-effectiveness, natural abundance, and improved safety profiles. However, the commercialization of metal batteries is hindered by several critical challenges, including nonuniform metal deposition, dendrite formation, and unstable solidelectrolyte interphase (SEI), which eventually lead to capacity degradation, short circuits, and battery failure, posing serious safety risks. $^{26-28}$

To address these issues, single-crystalline materials have emerged as crucial components, particularly as anodes or substrates for metallic deposition. Their highly ordered crystallographic orientation ensures a uniform and stable interface, which is vital in controlling metal nucleation and growth. Unlike polycrystalline substrates, which contain grain boundaries and structural inconsistencies that promote uncontrolled metal growth, single-crystalline substrates offer a more uniform deposition environment, mitigating dendrite formation. Furthermore, their coherent surfaces facilitate dense metal deposition, suppressing parasitic reactions, improving ion transport kinetics, and promoting the development of a more stable SEI layer. These advantages collectively contribute to enhanced cycling efficiency and a prolonged battery lifespan in next-generation metal battery systems.

In this review, we aim to provide a comprehensive understanding of the rationale and mechanisms behind the effective utilization and advancement of single-crystalline anodes for metal battery configurations as it is becoming a frontier of research (Figure 1). The definition of "single-crystalline" in this context does not strictly follow the classical definition of materials with a perfectly continuous lattice and

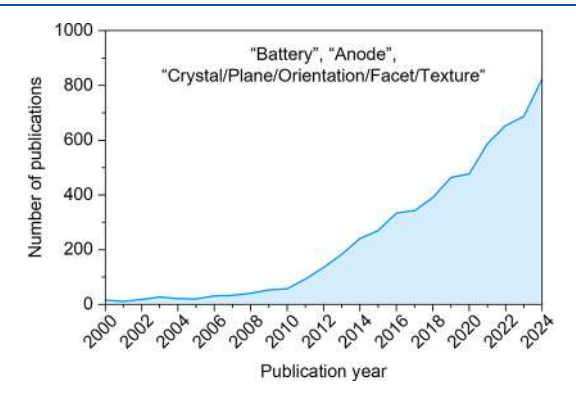


Figure 1. Number of publications each year from 2000 to 2024 based on search results of "battery", "anode", and "crystal/plane/orientation/facet/texture" according to Web of Science.

absence of grain boundaries. Rather, we adopt a broader and more practical interpretation spanning multiple scales: from atomic-level facet alignment to nano- or microscale particles exhibiting a dominantly uniform crystallographic orientation and even extending to bulk materials—such as metal foils—that can directly function as anode substrates. To provide insights into how single-crystalline materials improve the electrocrystallization process of metal batteries, we start from the crystal nucleation and growth theory and decipher the relationship between the theory and practical electrodeposition processes. Based on this understanding, we summarize the current research progress on the growth and application of single-crystalline materials in metal batteries, including Li, Zn, Na, Al, and Mg chemistries. Additionally, we discuss the application and challenges of single-crystalline host materials, such as silicon, graphite, and transition metal oxides, which have been widely studied or applied in LIBs. Finally, we present our perspective on the fabrication and recycling of single-crystalline materials, which are essential for realizing the sustainable roadmap toward the practical implementation of large-scale energy storage applications.

2. CRYSTAL NUCLEATION, INCUBATION, AND GROWTH THEORIES

In metal batteries, during the charging process, the reduction of desolvated metal ions leads to metal deposition on the anode side, which can be regarded as an electro-crystallization process. Therefore, within this section we start with the theories of crystal nucleation and growth, with a focus on the mechanisms that dominate the electrodeposition process in operating metal batteries. It is worth clarifying that the practical battery is a complicated system with a lot of inhomogeneity. The theories below mainly focus on specific particles or clusters under certain conditions, but the real situation can involve a variety of determinant factors; the actual electrodeposition process could be governed by multiple mechanisms. Therefore, at the end of the section, we will also discuss practical operating conditions that have a significant influence on the nucleation and growth of electrodeposits.

2.1. Nucleation

2.1.1. Homogeneous Nucleation Theory. When investigating metal electrodeposition, classical nucleation theory is often employed to understand the process. ^{33–35} Starting with the classical Gibbs equation, the total free energy change of a particle system is the sum of free energy change of forming a new surface, ΔG_s and forming the bulk crystal, ΔG_v (eqs 1 and 2):

$$\Delta G = \Delta G_s + \Delta G_\nu = 4\pi r^2 \gamma + \frac{4}{3}\pi r^3 \Delta g_\nu \tag{1}$$

$$\Delta g_{\nu} = \frac{-k_{\rm B}T \ln(S)}{V_{m}} \tag{2}$$

where r is the radius of spherical nuclei, γ is interfacial free energy, Δg_{ν} the difference of free energy per unit volume between the nuclei phase and ambient phase, V_m the molar volume of nucleus, k_B the Boltzmann's constant, T the absolute temperature, and S the supersaturation of solution.

The surface term, ΔG_s , is proportional to the surface area of the nucleus and represents the energetic penalty associated with overcoming interfacial tension to enlarge the nucleus and create a new interface. The bulk term, ΔG_v , is proportional to the nucleus volume, serving as the thermodynamic driving force that

promotes the nucleation of solvated ions under conditions of supersaturation (or under an applied overpotential in the case of electrodeposition). Since ΔG_s is always positive and the ΔG_v is always negative, we can define the critical nuclei size at the maximum free energy by making $\frac{d\Delta G}{dr}=0$, and the critical nuclei size can be defined in eq 3:

$$r_{crit} = \frac{2\gamma V_m}{k_{\rm B}T \ln(S)} \tag{3}$$

Critical nuclei size is generally used as a standard to reveal the thermodynamic status of a specific nucleus.³⁶ If the size of the nucleus is smaller than the critical size, it is likely to redissolve in the solution due to its thermodynamically unstable nature; otherwise, it would survive and form a stable nucleus (Figure 2).

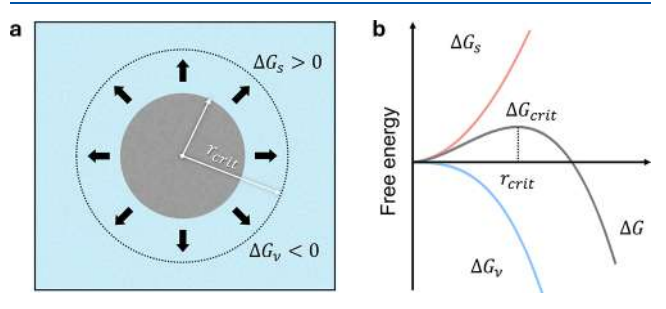


Figure 2. (a) Schematic of the homogeneous nucleation process. (b) Free energy profile and critical nucleation size in homogeneous nucleation theory.

2.1.2. Heterogeneous Nucleation Theory. While homogeneous nucleation is simpler and easier to understand, it is very rare in practical electrodeposition processes since it assumes that the nucleus is spherical. However, in a battery system, the desolvated metal ions are deposited on the electrode surface, forming a spherical cap-shaped nucleus with a contact angle (Figure 3). Therefore, the heterogeneous nucleation theory is usually applied to decipher metal electroplating on the substrate.

When considering the spherical cap with a contact angle θ , the volumetric shape factor and surface shape factor, respectively, can be written as eqs 4 and 5:³⁷

$$\nu(\theta) = \frac{(2 + \cos \theta)(1 - \cos \theta)^2}{4} \tag{4}$$

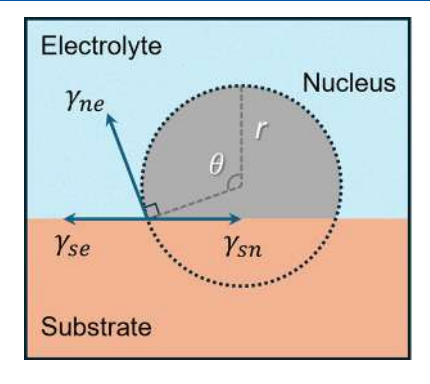


Figure 3. Schematic of the heterogeneous nucleation of a spherical cap nucleus on the substrate. θ is the contact angle, γ_{ne} is the interfacial free energy between the nucleus and electrolyte, γ_{sn} is the interfacial free energy between the substrate and nucleus, and γ_{se} is the interfacial free energy between the substrate and electrolyte.

$$s(\theta) = \frac{1 - \cos \theta}{2} \tag{5}$$

And the expression for Gibbs free energy in heterogeneous nucleation process is given as eq 6:³⁸

$$\Delta G^{hetero} = s(\theta) 4\pi r^2 \gamma_{ne} + \nu(\theta) \frac{4}{3} \pi r^3 \Delta g_{\nu} + \pi (r \sin \theta)^2$$

$$(\gamma_{sn} - \gamma_{se}) \tag{6}$$

According to Young's equation in eq 7:

$$\cos\theta = \frac{\gamma_{se} - \gamma_{sn}}{\gamma_{ne}} \tag{7}$$

The eq 6 can be rewritten as eq 8:

$$\Delta G^{hetero} = \nu(\theta) \left(4\pi r^2 \gamma_{ne} + \frac{4}{3}\pi r^3 \Delta g_{\nu} \right) \tag{8}$$

Further combination of eq 4 leads to eq 9:

$$\Delta G^{hetero} = \nu(\theta) \Delta G^{homo} \tag{9}$$

Considering that $v(\theta)$ is always less than one, the energy barrier of homogeneous nucleation is always larger than heterogeneous nucleation (Figure 4a). The decrease in

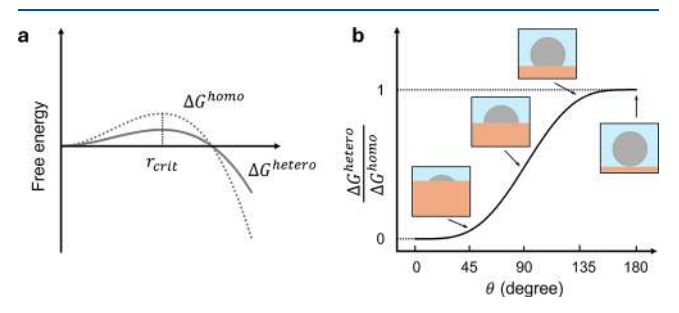


Figure 4. (a) The free energy profile of homogeneous nucleation vs heterogeneous nucleation. (b) The decrease in nucleation energy barrier of heterogeneous nucleation as a function of contact angle.

nucleation energy barrier of heterogeneous nucleation is also represented as a function of contact angle, as shown in Figure 4b. However, it is worth noting that the critical nuclei size for heterogeneous nucleation does not change when making $\frac{d\Delta G^{hetero}}{dr}=0.$

While classical nucleation theory offers fundamental thermodynamic insights, it has notable limitations: it does not incorporate electrochemical kinetics or reactions occurring during deposition. To bridge these gaps, several theoretical models have been developed to better describe the metal nucleation during electrodeposition. For example, the Scharifker–Hills model is among the first to incorporate kinetics and suggests whether the nucleation is instantaneous or progressive, which determines the deposit morphologies. Building upon this, the Li-SEI model further explicitly captures the influence of SEI fracture and reformation currents during Li metal nucleation. More detailed discussions of these models and their applications can be found elsewhere.

2.2. Incubation and Growth

2.2.1. Classical Growth Theory. The classical model of crystallization considers growth essentially as an amplification process in which stable nuclei are simply enlarged by monomer-by-monomer attachment without incurring structural changes in

the bulk or at the surface. Even though the metal electrodeposition process does not follow such a growth pattern, the fundamental kinetics can be quite similar. Thus, it is helpful to understand the growth behavior by starting from the classical growth model.

Based on the theoretical study conducted by Weller et al. and Hyeon et al., ^{42,43} the growth of spherical crystal particles into the solution can be divided into two steps: (1) the transport of the monomers from the bulk solution onto the crystal surface and (2) the reaction of the monomers on the surface (Figure 5).

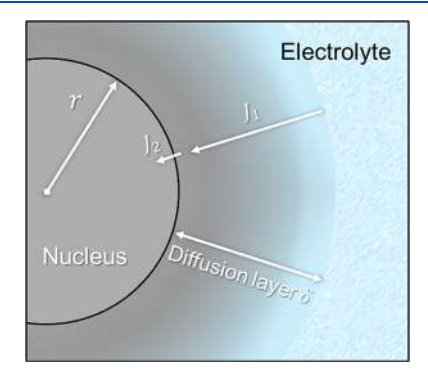


Figure 5. Schematic illustration of the growth of a spherical crystal particle in the solution.

Beginning with Fick's law of diffusion, two limiting kinetic factors were identified: diffusion of monomers to the surface (J_1) and the rate of reaction of these monomers on the surface (J_2) . The growth rate can be expressed as eq 10:

$$\frac{dr}{dt} = \frac{DV_m(C_{r+\delta} - C_r)}{r + D/k} \tag{10}$$

where r is the nucleus radius, D the diffusion constant, V_m the molar volume, k the reaction constant, $C_{r+\delta}$ the monomer concentration in the bulk electrolyte, C_s the monomer concentration at the nucleus surface, C_r the solubility of the nucleus, and δ the thickness of diffusion layer.

According to the Gibbs—Thomson effect, the particle radius also has a significant impact on growth rate, where the large particles grow faster than the smaller ones with higher solubility. For a spherical particle with a radius of r and extra chemical potential ($\Delta \mu = \frac{2\gamma V_m}{r}$), C_r is expressed as eq 11:

$$C_r = C_0 \cdot \exp\left(\frac{2\gamma V_m}{rRT}\right) \tag{11}$$

where C_0 is the solubility of the monomer in equilibrium. By inserting the expression into eq 10, the growth rate can be rewritten as eq 12:

$$\frac{dr}{dt} = \frac{DV_m C_0}{r + \frac{D}{k}} \left[\frac{C_{r+\delta}}{C_0} - \exp\left(\frac{2\gamma V_m}{rRT}\right) \right]$$
(12)

By making $\frac{dr}{dt} = 0$, the critical nuclei size is obtained as eq 13:

$$r_{crit} = \frac{2\gamma V_m}{RT \ln\left(\frac{C_{r+\delta}}{C_0}\right)}$$
(13)

Based on the definition of supersaturation *S*, eq 13 can be further simplified to eq 14:

$$r_{crit} = \frac{2\gamma V_m}{RT \ln(S)} \tag{14}$$

which is the same as expression of critical nuclei size in eq 3. Therefore, from a kinetic perspective, Gibbs—Thomson effect will lead to the dissolution of the small nucleus for $r < r_{crit}$, while the nucleus is kinetically stable for further growth for $r > r_{crit}$.

To further identify the two distinct models, two dimensionless variables were introduced (eqs 15 and 16):⁴²

$$r^* = \frac{RT}{2\gamma V_m} r \tag{15}$$

$$Da = \frac{2\gamma V_m}{RT} \frac{k}{D} \tag{16}$$

where r^* is the capillary length, a measure of the size effect on the chemical potential of a particle, and Da the Damköhler number, a descriptor to relate reaction kinetics with mass transport. As a result, the growth process is reaction-controlled for a small nucleus $(r^**Da \ll 1)$, while the growth gradually transits to a diffusion-controlled as the nucleus radius increases $(r^**Da \gg 1)$.

It has been well-recognized that the two growth models can lead to distinct deposition morphology. Exemplified using Li metal electrodeposition, a diffusion-controlled process is not favored to achieve a dendrite-free morphology, since the low diffusion process may lead to the accumulation of Li ions and induce the generation of local electric field/current density. 28

Beyond the single-step process of monomer attachment, crystal growth can also involve multistep pathways. For example, intraparticle growth has been used to describe the crystal growth behavior of quantum rods; 45 a self-assembly process has been synergistically performed for the synthesis of organic semiconductors. 46 Herein, we would like to focus on two nonclassical growth mechanisms, ripening and coalescence, which are closely related to the electrodeposition process, especially with respect to battery chemistry.

2.2.2. Ostwald Ripening and Digestive Ripening. After the initial nucleation of the metal ions on the substrate, the nuclei can undergo an incubation period before further growth to the bulk crystals. Since the nucleation rate is highly dependent on the local physicochemical properties such as solution concentration and substrate surface morphology, the as-formed nuclei are likely to be polydisperse.

Considering that the system remains thermodynamically unstable until it reaches the minimum free energy, a redissolution—deposition process may occur for stabilization through decreasing the total surface area of the nuclei. The radius difference of polydisperse nuclei leads to solubility fluctuation and local concentration gradient, which acts as the driving force for the growth of the large particles at the expense of the redissolution of smaller ones (Figure 6a). The process was first described by Wilhelm Ostwald, and more details of the above theory on the calculation of the critical particle radius, thermodynamics, and kinetics were described by Lifshitz—Slyozov—Wagner (LSW) theory.

For the metal electrodeposition process inside a battery, when applying a moderate current density or achieving a relatively low local overpotential, the growth of the metal nuclei is generally governed by Ostwald ripening.⁵⁰ In the previous literature, it is quite common to observe large, sparsely distributed nuclei on the substrate at the early stage of the deposition, which serves as evidence of minimized local overpotential.^{51–53} With the

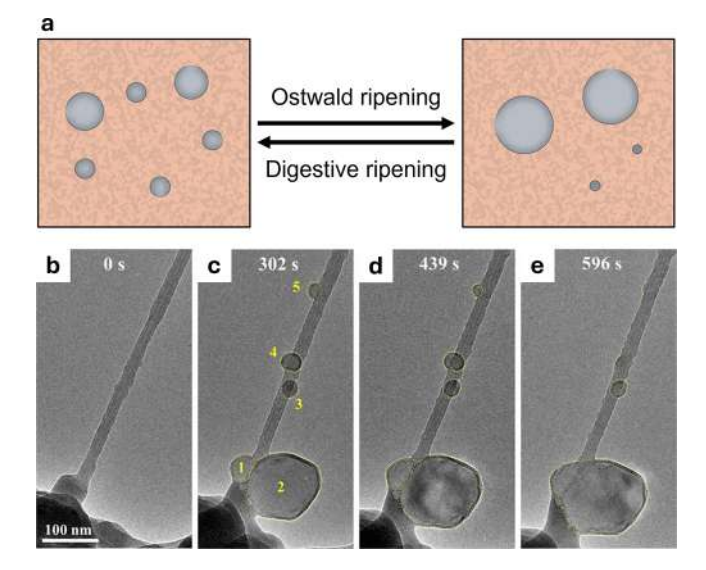


Figure 6. (a) Schematic illustration of Ostwald ripening-dominated growth and digestive ripening-dominated growth. (b–e) Timeresolved TEM images of Na metal deposition at the MWCNT/ Na_2CO_3/CO_2 triple point via Ostwald ripening. Reproduced with permission from ref 54. Copyright 2022 Springer Nature.

development of advanced operando characterization techniques, the Ostwald ripening process has been directly observed in Li/Na plating processes. As shown in Figure 6b—e, the *in situ* transmission electron microscopy (TEM) images suggest the Ostwald ripening dominated Na incubation at the multiwall carbon nanotube (MWCNT) substrate. After the initial nucleation of the Na, five Na crystals are observed on the MWCNT. As more charges pass, small Na crystals shrink continuously until they almost disappear, while large Na crystals experience continued growth.

Digestive ripening is exactly the opposite of Ostwald ripening, where the small nuclei grow at the expense of larger ones with the aid of an organic ligand/surfactant. The method, commonly named solvated metal atom dispersion, is widely used for producing monodisperse nanoparticles of metals and metal alloys from polydisperse raw materials. To the best of our knowledge, digestive ripening is barely reported in a typical electrodeposition process inside a battery configuration.

2.2.3. Coalescence. Coalescence, an aggregation-induced crystal growth, is commonly observed in nucleus growth during electrodeposition. The coalescence of deposited Li nuclei was directly observed using time-resolved operando TEM. The driving force of coalescence is quite the same as that of ripening, which is the reduction of surface free energy by decreasing the surface area of the nuclei. However, the difference is that the redissolution of deposits no longer occurs during coalescence since the nuclei at this stage are thermodynamically stable. As shown in Figure 7a, the coalescence of spherical Li nuclei was found to occur through fusion on the carbon surface as indicated by yellow arrows.

It is also worth noting that coalescence growth shows no preferential attachment of crystal lattice, which leads to the formation of grain boundaries after the fusion. Figure 7b shows the snapshots of rearrangement of Li clusters during coalescence using the molecular dynamics (MD) method coupled with Monte Carlo (MC), where small clusters are captured by the large one and migrate toward each other, followed by particle fusion. The small cluster B rearranged itself

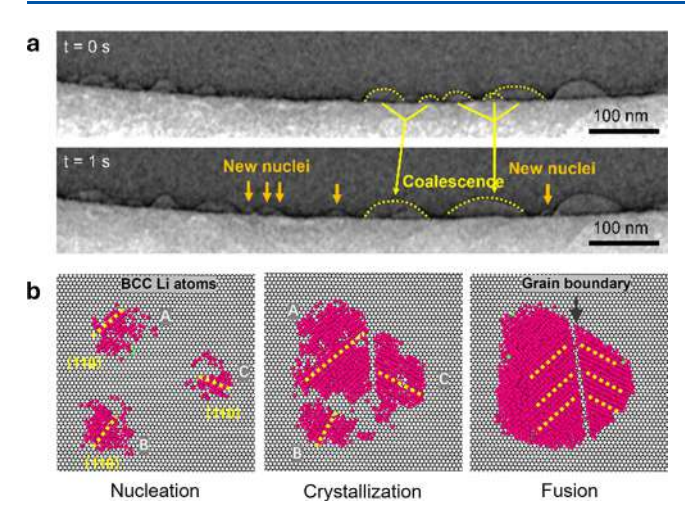


Figure 7. (a) Time-resolved bright field (BF)-TEM images (contrast inverted) showing the *in situ* nucleation and coalescence of Li nuclei upon deposition. (b) Snapshots of atomistic simulations showing the rearrangement of Li clusters during coalescence and the resultant bicrystal. Reproduced with permission from ref 57. Copyright 2023 American Chemical Society.

to align with the crystallographic orientation of the larger cluster A, while cluster C retained its orientation, resulting in the formation of a bicrystal containing a grain boundary.

It has been demonstrated that coalescence kinetics are influenced by many factors such as physicochemical properties of the parent phase, size distribution and morphology of the nuclei, and surface tension at the grain boundary interface. For example, the deposition behavior of metals can be significantly improved on highly textured substrates through facilitated coalescence, ^{59,60} and the coalescence stability can be modulated by employing various electrolyte additives. ^{61,62}

2.3. Critical Determinants in Practical Electro-Crystallization

In practical battery systems, crystal nucleation and growth occur in a more complex manner. As shown in Figure 8, metal cations

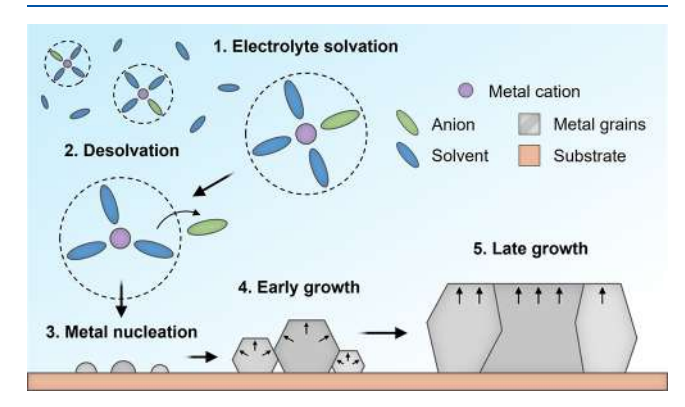


Figure 8. Schematic showing metal electrodeposition process in practical battery systems containing a liquid electrolyte and substrate.

are solvated by the solvent and coordinate with salt anions to form a solvation shell. During the charge-transfer process, metal cation is desolvated with repulsion of anion, depositing a metal nucleus on a substrate. Upon continuous deposition, these nucleated seeds grow and coalesce with each other, eventually forming a dense deposit in an ideal scenario. In this section, to correlate the crystal nucleation and growth theory to the

practical situation for the heterogeneous nucleation and growth of metal electrodeposits on electrodes, we identify several key determinants, with the focus on elucidating how they influence the nucleation and/or the growth kinetics.

2.3.1. Impact of Overpotential. Overpotential is a measurable physical parameter used to evaluate the electrodeposition dynamics. Ely and García⁵⁰ analyzed the thermodynamic and kinetic influence of overpotential in heterogeneous nucleation and growth of electrodeposits. The difference in free energy per unit volume between the nuclei phase and ambient phase, Δg_{v} is given as eq 17:

$$\Delta g_{\nu} = \Delta g_f + \frac{zF\eta}{V_m} \tag{17}$$

where Δg_f is the bulk free energy of transformations, z the valence of electrodepositing ion, F the Faraday's constant, η the overpotential, and V_m the molar volume of electrodeposits. The expression of thermodynamic critical nuclei size for nucleation can be rewritten in eq 18:

$$r_{crit,t} = -\frac{2\gamma_{ne}}{\Delta g_f + \frac{zF\eta}{V_m}} \tag{18}$$

Considering the growth of a single, isolated, spherical capshaped electrodeposit, its growth dynamic is given by the kinetic equation in eq 19:

$$\frac{dr}{dt} = j_0 V_m \left(\frac{zF\eta}{RT} + \frac{2\gamma_{ne}V_m}{rRT} \right) \tag{19}$$

where j_0 is the exchange current density, γ_{ne} the nucleus-electrolyte interfacial free energy, R the gas constant, and T the absolute temperature. Therefore, the expression of critical nuclei size regarding kinetic descriptors (eq 20) is obtained by making $\frac{dr}{dt} = 0$:

$$r_{crit,k} = -\frac{2\gamma_{ne}V_m}{zF\eta} \tag{20}$$

It can be concluded from eq 20 that the increase in overpotential results in a reduced thermodynamic and kinetic critical nuclei size. 64,65

After thermodynamic and kinetic principles were combined, five regimes were identified. As shown in Figure 9, 50 the blue line marks the boundary of thermodynamic stability of the nucleating phase. The nuclei formed during the initial stages, which lie in the nucleation suppression regime (below the blue line), are thermodynamically unstable and tend to redissolve. The following embryo incubation stage is divided into two regimes, depending on the local overpotential. The long incubation regime with small overpotential is dominated by Ostwald ripening kinetics, where small embryos dissolve and redeposit on the larger ones, promoting their steady growth approaching the critical radius. Conversely, a large overpotential in the short incubation regime results in accelerated growth, facilitating small-sized nuclei formation with a monodispersed distribution. Above the black curve lies the growth regime, where kinetically favored nuclei grow steadily during the early stage, followed by a transition to the late growth regime in which dendritic growth may occur due to inhomogeneous topography and localized electric fields.

2.3.2. Substrate Effect. For the heterogeneous nucleation process, the lattice constants of the substrate and deposits are usually different, which may induce inhomogeneity at the

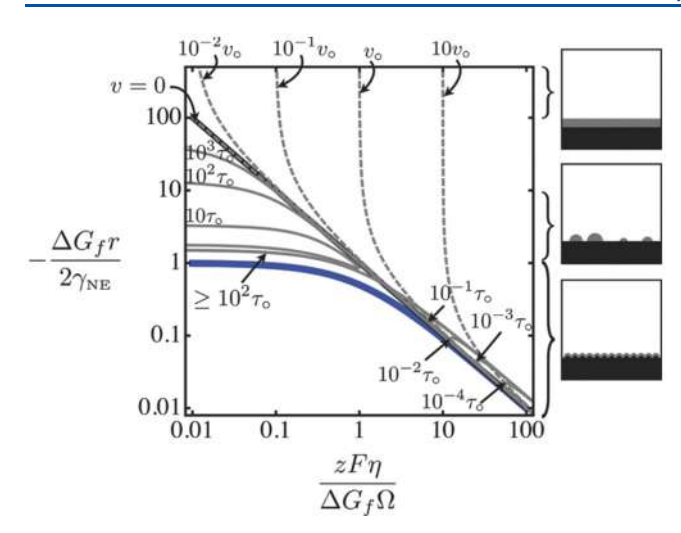


Figure 9. Regimes of the Deposition Behavior during the initial stages of nucleation and growth. The solid gray curves embody locus of incubation time of fixed value, and the dotted gray curves show the initial growth velocities of the stable nuclei. The x-coordinate denotes normalized critical overpotential, and the y-coordinate denotes normalized electrodeposit size. v_0 is the characteristic growth velocity, and τ_0 the characteristic incubation time. Reproduced with permission from ref 50. Copyright 2013 The Electrochemical Society.

interface. Therefore, lattice mismatch δ can be calculated to evaluate the coherence of the interface using eq 21:⁶⁶

$$\delta = \frac{|\alpha_d - \alpha_s|}{\alpha_s} \times 100\% \tag{21}$$

where α_d is the in-plane lattice constant of deposits, and α_s the in-plane lattice constant of substrate.

For a fully coherent interface, as shown in Figure 10, the lattice constants of substrate and precipitation are identical, which

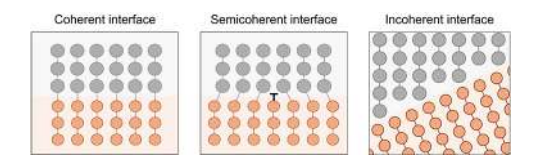


Figure 10. Schematic illustration of coherent, semicoherent, and incoherent interfaces of two distinct phases.

leads to a δ equal to 0. The change of the interfacial free energy would be entirely attributed to the chemical bonding transformation: substrate—substrate and deposits—deposits to substrate—deposits. When the lattice constants of two phases differ slightly, a semicoherent interface is formed. For example, if $\alpha_d=1.05$ Å and $\alpha_s=1$ Å, the lattice mismatch is $\delta=5\%$, meaning that a misfit dislocation forms every 20 planes in the substrate phase to accommodate the lattice mismatch. This would lead to a higher interfacial free energy barrier compared to that of a coherent interface because the misfit also contributes to free energy changes. ⁶⁷

However, as the lattice mismatch keeps increasing, the dislocation and defects are forming more frequently at the interface, until a δ > 25%. By then, a dislocation happens every 4 continuous planes in the substrate phase, resulting in a very different lattice configuration, and the interface would become incoherent. The big misfit can also lead to a significantly higher

interfacial free energy, increasing the nucleation energy barrier ΔG and hindering nucleation kinetics.

2.3.3. Temperature Effect. As mentioned earlier, the growth process involves two steps: diffusion and a surface reaction. Considering both are temperature-dependent processes, an elevated temperature undoubtedly accelerates the dynamic of the whole process. Therefore, based on a steady-state diffusion-reaction mathematical model, Akolkar defined a dendrite growth rate ratio $(\frac{i_t}{i_f}$ in eq 22) to describe the impact of temperature to Li deposition (Figure 11a):

$$\frac{i_{t}}{i_{f}} = \left\{ -\frac{1}{bC_{0}} \ln \left[e^{-bC_{0}} + \frac{i_{f}(1 - t_{+})b\delta}{nFa} \right] \right\}^{-(\frac{a_{c}}{n})}$$
(22)

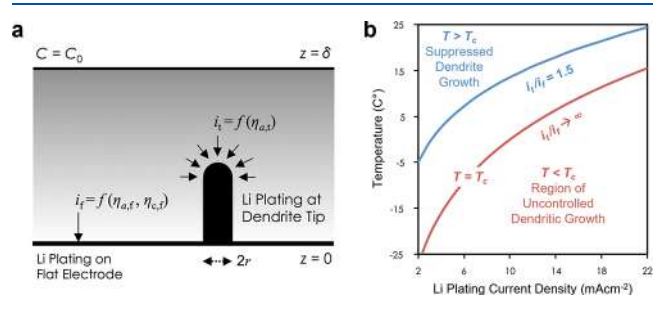


Figure 11. (a) Schematic of the electrode surface on which Li is electrodeposited. The dendrite growth rate ratio $\binom{i_t}{i_f}$ can be employed to study the temperature-dependence of the dendritic growth process. (b) Variation of the dendrite growth rate ratio $\binom{i_t}{i_f}$ with temperature and Li plating current density. Reproduced with permission from ref 69. Copyright 2014 Elsevier.

where i_f is the Li plating current density on a flat surface, a the diffusion pre-exponent, b a transport-dependent constant, C_0 the bulk concentration, t_+ the Li⁺ transference number, δ the thickness of diffusion boundary layer, n the electron transfer number, F the Faraday constant, and a_c the cathodic charge-transfer coefficient. In this equation, there are factors following the Arrhenius-type temperature-dependence, which can be expressed as eqs 23 and 24:

$$a = a_0 \cdot \exp\left\{\frac{E_D}{R} \left(\frac{1}{T_0} - \frac{1}{T}\right)\right\} \tag{23}$$

$$a_{c} = a_{c}^{0} \cdot \exp\left\{-\frac{E}{2R}\left(\frac{1}{T_{0}} - \frac{1}{T}\right)\right\}$$
(24)

where T_0 is the reference temperature, a_0 the pre-exponent at T_0 , a_c^0 the cathodic charge-transfer coefficient at T_0 , E_D the solution phase diffusion activation energy, E the solid phase (i.e., SEI) diffusion activation energy, and E the gas constant. Therefore, decreasing the temperature results in a lower diffusion pre-exponent E0, which hinders diffusion, and an elevated cathodic transfer coefficient E0, which can be attributed to the reduced surface reaction resistance on a thinner SEI layer. This eventually leads to an increased dendrite growth rate ratio, which agrees with empirical studies.

The temperature-current density profile was obtained using parameter values in the system of 1 M LiPF $_6$ salt in ethylene carbonate (EC)/dimethyl carbonate (DMC), and a critical

temperature T_c $(\frac{i_t}{i_f} \to \infty)$, red curve) was defined to assess the dendritic suppression, below which uncontrolled dendritic growth is initiated (Figure 11b). In contrast, the region above the blue curve $(\frac{i_t}{i_f} = 1.5)$ is favorable for dendrite inhibition and stable battery operation.

2.3.4. Pressure Effect. For the practical application of batteries with a pouch configuration, applying external pressure is generally believed to extend the battery life, which has been demonstrated in numerous studies. For example, Meng et al. ⁷⁴ elucidated that applying an optimized stack pressure can finetune the Li nucleation and growth direction toward a dense deposition, staying away from the dendrite growth caused by mass transport limitations. Dahn et al. ⁷⁵ also demonstrated the impact of varying the applied mechanical pressure to the capacity retention and life span of the pouch cells.

To explain this phenomenon, Harris et al. ⁷⁶ developed a three-dimensional (3D) electrochemical-contact model. Their study suggests that when applying moderate (hundreds of kPa or less) pressures, most of the Li surface feels no force at all. Instead, the inhibition of dendritic growth could be attributed to the avoidance of Li plating at the tips under sufficient local stress at the tip. This hypothesis was further confirmed by Zhang et al., ⁷⁷ where mechano-electrochemical phase field model was proposed to mimic the multiphysics processes (Figure 12). The

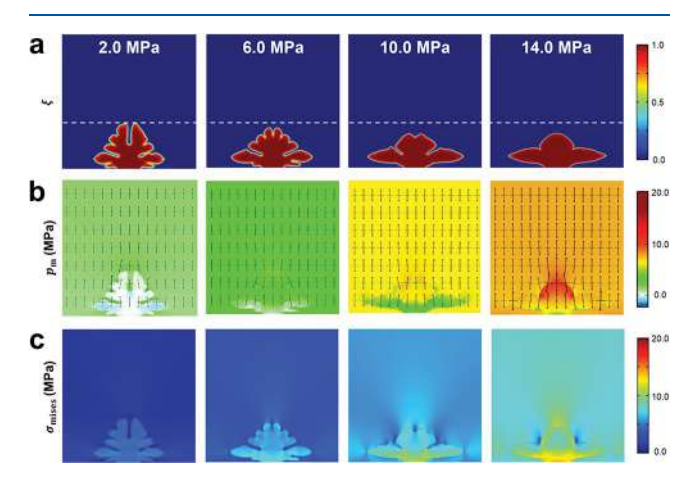


Figure 12. Simulated results of (a) dendritic morphology, (b) principal stress and hydrostatic pressure, and (c) von Mises stress evolution of Li dendrites under an external pressure ranging from 2.0 to 14.0 MPa. Reproduced with permission from ref 77. Copyright 2021 John Wiley and Sons.

impacts of external pressure on electroplating are outlined as (1) inhibiting the progress of electroplating reaction and (2) shaping the morphology of Li dendrites to be smooth and dense under the rise of local hydrostatic pressure.

Overall, numerous efforts have been devoted to deciphering how practical factors—such as overpotential, substrate, temperature, and pressure—affect the nucleation and growth of metals, offering valuable insights into understanding of electrodeposition. However, it is worth noting that most of the above discussions are rooted in theoretical models that typically focus on idealized cases, such as the behavior of a single nucleus or an isolated dendrite, which may have limited applicability in a practical scenario. The real electrodeposition is a complex, collective process in which the inhomogeneity of the system and interactions across multiple nucleation sites

necessitate a macroscopic perspective to fully capture the observed phenomena. Using operando reflection interference microscope (RIM), Shan et al.81 directly observed that Li heterogeneous nucleation also possesses a progressive nature, where the formation of initial Li nuclei is not at the exact same time. After this stage, the Li nuclei size increases collectively and the total number of Li nuclei is relatively stable, which is a characteristic of the instantaneous nucleation process. In addition, the nucleation and crystal growth processes could show significant temporal overlap or even competitiveness. The ultimate morphology of the deposits would be significantly influenced by complicated factors both thermodynamically and kinetically. Lee et al. 82 investigated the impact of competitive mechanisms between nucleation and growth on the Li metal deposition morphology. Three reaction steps (heterogeneous Li nucleation on the substrate, Li growth, and homogeneous Li nucleation on the Li metal) were identified, and the rates of each step were controlled by adjusting the current collector, electrolytes, and electroplating conditions. The results suggested that columnar Li metal formed when Li nucleated on the substrate outpaced Li growth and self-deposits, while multilayers of Li metal spheres were observed with fast Li growth kinetics.

In summary, starting from classical models of crystal nucleation and growth, we identify and summarize critical determinants (overpotential, substrate, temperature, and pressure) in practical metal deposition during battery operation. Based on these theoretical frameworks, we introduce and summarize key recent strategies and understandings on electrocrystallization of different metal chemistries in the following sections.

3. LI METAL ANODE

The Li metal anode has been the most promising anode candidate due to its high theoretical gravimetric and volumetric capacities (3861 mAh g⁻¹ and 2061 mAh cm⁻³, respectively) and the lowest redox potential (-3.04 V vs standard hydrogen electrode). Despite these advantages, its practical implementation has been plagued by uncontrollable growth and deposition of Li, known as dendrites, resulting in increased side reactions with electrolyte, low electrochemical reversibility, and even safety concerns from short-circuits. ^{15,83}

Various research directions, such as electrolyte additives, ^{84–86} interfacial coatings, ^{87–89} and 3D current collectors, ^{53,90,91} have been explored to control and stabilize the growth of Li metal. Although these works successfully demonstrated outstanding improvements on performance and cycle life, recent works have pivoted toward understanding and controlling growth of Li at a crystallographic level. This section aims to provide a comprehensive discussion of considerations and strategies for crystalline growth of Li metal under various practical conditions.

3.1. Li Substrates for Li Crystal Growth

3.1.1. Single-Crystalline Li: Growth and Facets. Understanding the structural and chemical identities of Li metal with atomic resolution has been challenging due to its chemically reactive and beam-sensitive nature. Cui et al. successfully identified the atomic resolution of structures and SEI of electrochemically deposited single-crystalline Li dendrites by employing cryogenic TEM (cryo-TEM). The electrochemically deposited Li metal on a copper (Cu) grid was cooled below –170 °C by liquid nitrogen, in which the temperature was maintained during the electron beam exposure (Figure 13a). From selected-area electron diffraction (SAED) analyses, single-

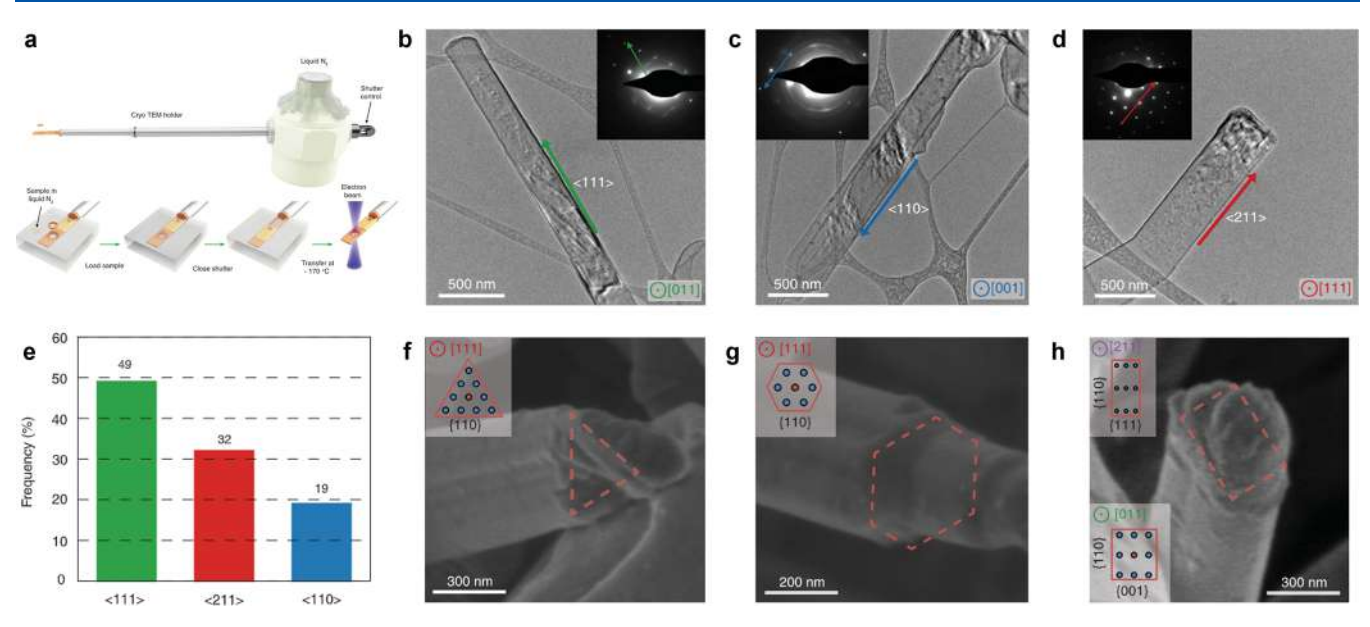


Figure 13. Preferential Li growth direction characterized with cryo-TEM. (a) Schematic of cryo-TEM characterization. TEM images and SAED patterns of Li metal with (b) $\langle 111 \rangle$, (c) $\langle 110 \rangle$, and (d) $\langle 211 \rangle$ growth directions. (e) Statistics of Li metal growth direction. SEM images of Li metal showing (f) triangular, (g) hexagonal, and (h) rectangular cross-sectional structures. Reproduced with permission from ref 92. Copyright 2017 The American Association for the Advancement of Science.

crystalline Li nanowires were observed to have preferential growth directions such as $\langle 111 \rangle, \langle 110 \rangle,$ and $\langle 211 \rangle$ (Figure 13b—d). The statistics show that Li metal growth was mostly preferential along $\langle 111 \rangle$ direction rather than $\langle 110 \rangle$ and $\langle 211 \rangle$ in carbonate-based electrolytes (Figure 13e). The growth along $\langle 111 \rangle$ was attributed to the minimization of surface energy by exposing the lowest surface energy (110) facet. The scanning electron microscopy (SEM) images of dendrites also exhibited different facet structures according to growth directions, such as triangular (Figure 13f), hexagonal (Figure 13g), and rectangular (Figure 13h), which exhibited (110) facets entirely for $\langle 111 \rangle$ and partially for $\langle 211 \rangle$ and $\langle 011 \rangle$ directions. This result suggests that Li metal has a favorable growth direction and exposed facets.

Luo et al. systematically explored electrochemical deposition behaviors of single-crystalline Li metals with different facets.²⁵ Interestingly, different facets of single-crystalline Li metal exhibited a similar trend of critical current density (CCD) regardless of electrolyte systems (Figure 14a). The trend of CCD followed Li adatom migration diffusion barrier of different facets, where (110) facet with the lowest migration barrier of 0.02 eV showed the highest CCD compared to (200) and (211) facets with migration barriers of 0.14 and 0.41 eV, respectively. Phase-field model simulation was further employed to predict the deposition morphology as a function of the reaction rate and self-diffusion rate (Figure 14b). Accordingly, morphologies of Li deposits significantly varied, where the (110) facet showed dense Li deposits even at high current density of 5 mA cm⁻² and areal capacity of 10 mAh cm⁻² compared to (200) and (211) orientations (Figure 14c). Unlike single-crystalline Li metal, polycrystalline Li metal showed multiple domains of different crystal facets from the electron backscatter diffraction (EBSD) inverse pole figure (IPF) map (Figure 14d,e). When Li is deposited, single-crystalline Li(110) forms uniform seeds, whereas polycrystalline Li forms nonuniform, dendritic seeds. These different morphologies of Li seeds resulted in less reversible and more isolated Li for polycrystalline, confirmed by

titration gas chromatography (TGC) analysis after 50 cycles (Figure 14f).

It is also necessary to understand whether crystallographic orientations are maintained during extended electrochemical cycling under various operation conditions. Archer et al. showed that crystallographic orientation of Li could be maintained with increasing areal capacities. 93 From two-dimensional (2D) general area X-ray diffraction (XRD) analysis, the Li(110) peak was dominant after deposition capacity of 5 mAh cm⁻². When more Li was deposited with 10 and 20 mAh cm⁻², the (110) orientation was maintained without the obvious appearance of other peaks. Li et al. reported a systematic comparison of Li(110) and (200) on crystallographic orientation evolution for prolonged cycles.⁹⁴ It was shown that Li(110) maintained the (110) peak over 300 cycles at 1 mA cm⁻² with 1 mAh cm⁻², whereas Li(200) showed gradual disappearance of the (200) peak with the appearance of other facets, such as (110), (211), and (310). Li et al. further explored the effect of high current densities of 5, 10, and 20 mA cm⁻² on crystallographic orientation of Li growth. 95 It was found that the (110) orientation disappeared with increasing current densities, indicating uncontrollable crystal growth of Li metal. To resolve this issue, a low-rate-healing strategy was proposed and employed, which showed recovery of (110) orientation as well as electrochemical properties, enabling extended long-term cycling stability of the Li metal anode.

3.1.2. Surface Effect on Li Crystal Growth. The surface chemistry of the Li metal also affects its crystal growth. Choi et al. reported a comparison of pristine Li metal and naked Li metal obtained after surface treatment with BBr₃ to remove native oxide layers. ⁹⁶ After Li deposition of 1 mAh cm⁻² at 1 mA cm⁻², pristine Li metal showed a mossy morphology with only 1.2% Li phase fraction from SEM and EBSD images (Figure 15a), whereas naked Li metal showed densely packed deposits with 64.6% Li phase fraction (Figure 15b). For pristine Li metal, the presence of a native oxide layer induces out-of-plane growth, resulting in dendritic growth (Figure 15c), while for naked Li metal, the absence of a native oxide layer induces in-plane

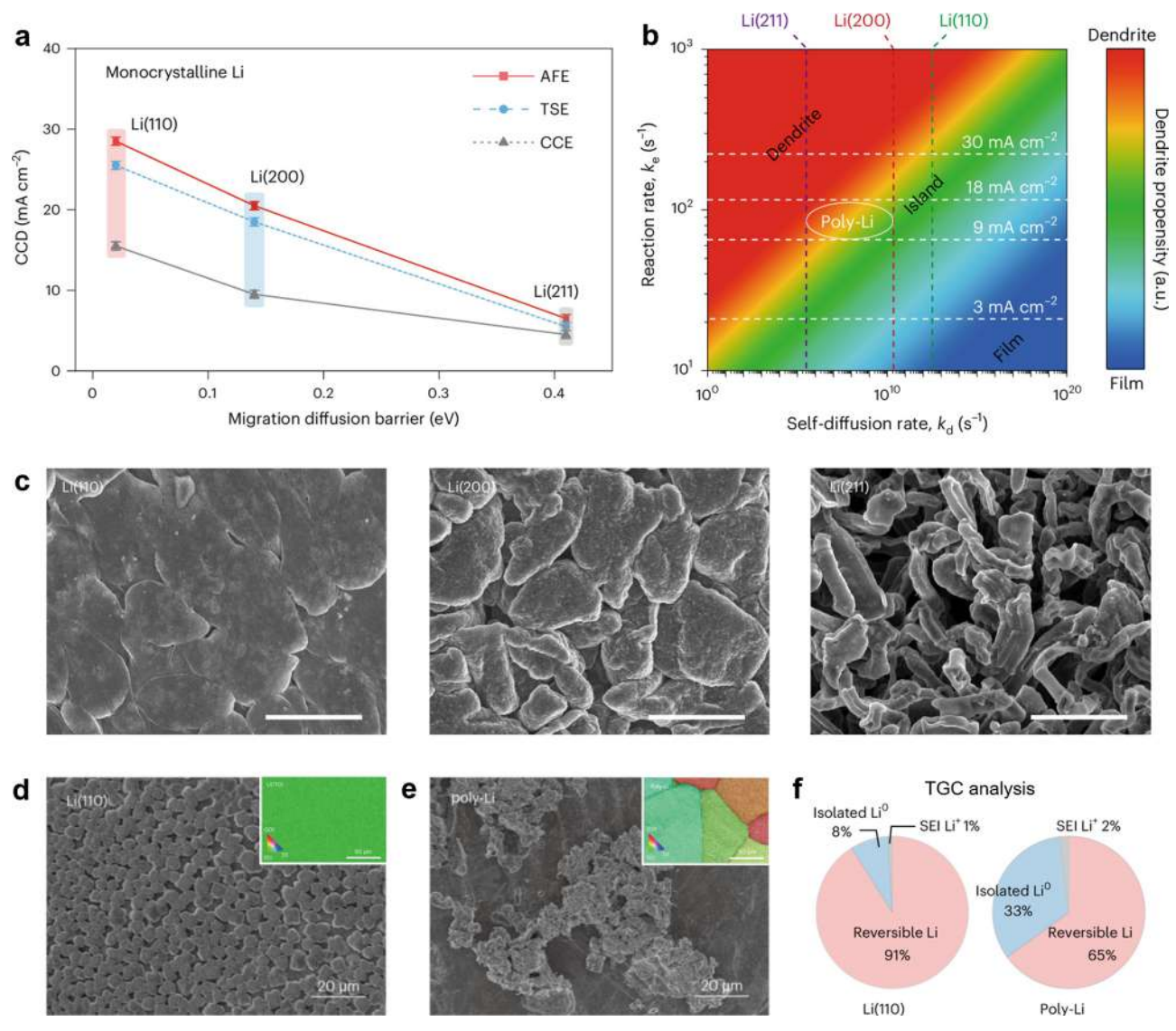


Figure 14. Electrochemical behavior and deposition morphology of single-crystalline Li metal. (a) CCD test of single-crystalline Li metal with (110), (200), and (211) facets with corresponding migration diffusion barrier in different electrolytes (AFE: all-fluorinated electrolyte, TSE: ternary salt electrolyte; CCE: commercial carbonate electrolyte). (b) A phase map of predicted deposition morphology in AFE based on reaction rate and self-diffusion rate. (c) SEM images of Li deposition morphologies of single-crystalline Li metal anodes at 5 mA cm⁻² with 10 mAh cm⁻² in AFE. SEM image of deposited Li seeds of (d) single-crystalline Li(110) and (e) polycrystalline Li. Inset shows EBSD IPF map at pristine state. (f) TGC analysis after 50 cycles in AFE. Reproduced with permission from ref 29. Copyright 2025 Springer Nature.

growth, leading to epitaxial growth (Figure 15d). Similarly, Ingenito et al. also reported a systematic comparison of Li metal prepared with conventional extrusion and thermal evaporation. The surface passivation layer of the extruded Li showed a thicker Li₂O layer than that of the evaporated Li (hundred nanometers vs tens of nanometers). This thinner native oxide layer of evaporated Li resulted in reduced charger transfer resistance as well as denser Li deposition in both ether and carbonate electrolytes. These results show that the surface chemistry of Li metal is crucial even before the electrochemical process.

The SEI layer, which is formed on the Li metal surface during the electrochemical process, is the most critical interphase affecting the Li growth kinetics. With SEI having slow Li⁺ transport, the slow-growing (110) facet cannot surpass and cover (200) due to transport limitations, eventually exposing the (200) facet (Figure 16a). On the other hand, with SEI having fast Li⁺ transport properties, the (110) facet can surpass and

cover (200), exposing the surface with the (110) facet (Figure 16b). Xiao et al. reported an SEI engineering strategy that facilitates growth of Li(110) by introducing $CF_3Si(CH_3)_3$ on the surface of Li metal. The SEI-engineered Li metal showed a thinner SEI layer (30.5 nm) consisting of highly ordered crystalline LiF and Li₂O, whereas pristine Li metal showed a thicker SEI layer (97.2 nm) consisting of an amorphous matrix with disordered crystalline Li₂O and Li₂CO₃. Due to these distinct SEI thicknesses and compositions, highly oriented growth of Li(110) was observed for the SEI-engineered Li metal and less oriented growth with prominent Li(200) was observed for the pristine Li metal (Figure 16c).

3.1.3. Li-Alloy Substrates. Surface and bulk diffusion properties of the Li metal can be modified with Li-alloy materials. A large variety of materials alloying with Li are reported to exhibit high lithiophilicity, such as gold (Au), ⁵¹ silver (Ag), ^{99–101} Zn, ^{102,103} silicon (Si), ^{104–106} and tin (Sn). ¹⁰⁷ Of note, Li–Mg has been reported to form a solid-solution phase

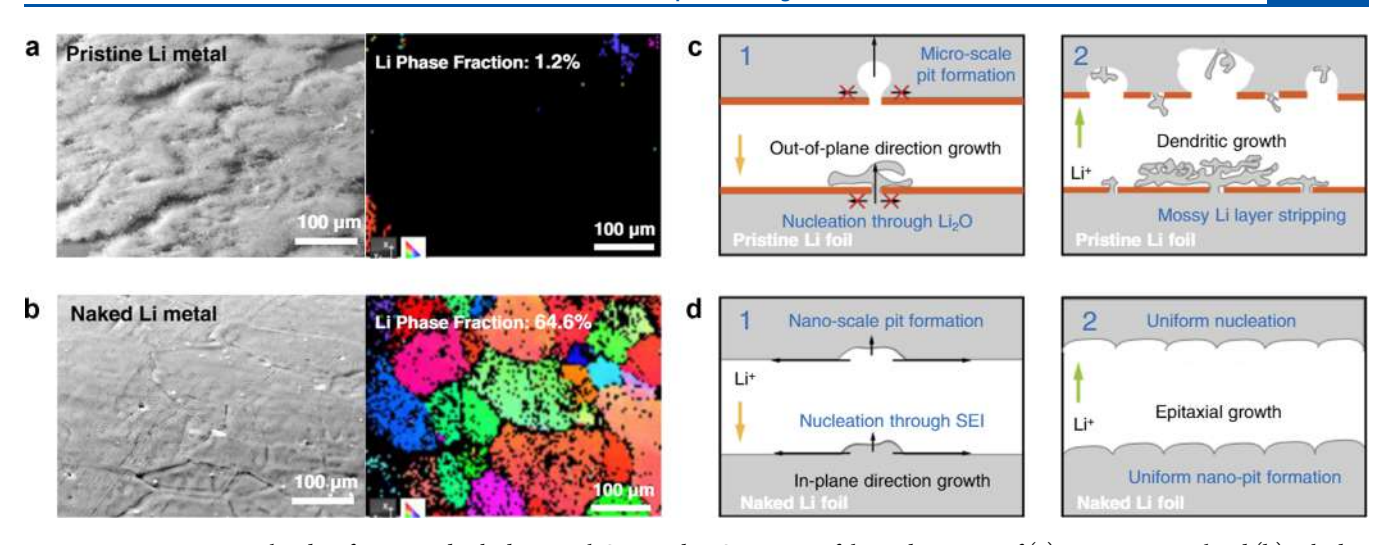


Figure 15. Pristine Li metal and surface-treated naked Li metal. SEM and EBSD images of the Li deposition of (a) pristine Li metal and (b) naked Li metal at 1 mA cm⁻² with 1 mAh cm⁻². Schematics of Li growth mechanism in (c) pristine Li metal with presence of native oxide layer and (d) naked Li metal without native oxide layer. Reproduced with permission from ref 96. Copyright 2023 Springer Nature.

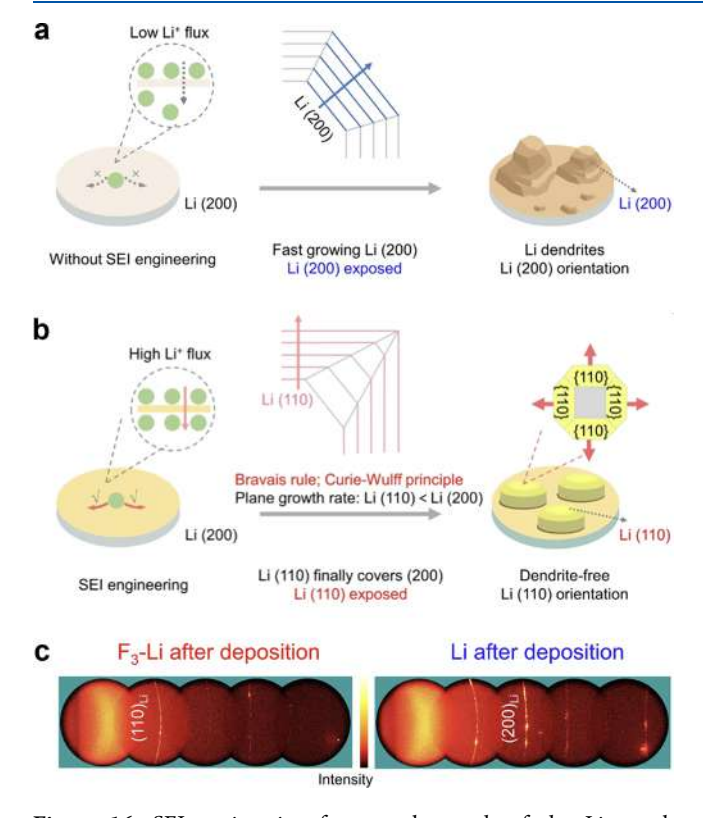


Figure 16. SEI engineering for crystal growth of the Li metal. Schematics of Li metal (a) without SEI engineering, resulting in Li(200) orientation, and (b) with SEI engineering, resulting in Li(110) orientation. (c) 2D general area XRD analysis of SEI-engineered Li metal and pristine Li metal after Li deposition at 1 mA cm⁻² with 5 mAh cm⁻². Reproduced with permission from ref 98. Copyright 2023 John Wiley and Sons.

without any phase changes during electrochemical reactions, facilitating reaction kinetics and stabilizing structures. ^{108–110} By utilizing the solid-solution phase of LiMg, Wang et al. reported single-crystalline (110)-oriented $\text{Li}_{0.9}\text{Mg}_{0.1}$. ¹¹¹ Compared to the polycrystalline counterpart, single-crystalline LiMg showed higher Li diffusion coefficient (9.40 × 10⁻⁸ vs 3.27 × 10⁻⁹ cm² s⁻¹), resulting in greater grain size of Li deposition. From *ex situ*

XRD analysis, polycrystalline LiMg showed the appearance and disappearance of other (200) and (211) peaks during stripping and plating (Figure 17a), whereas single-crystalline LiMg(110)

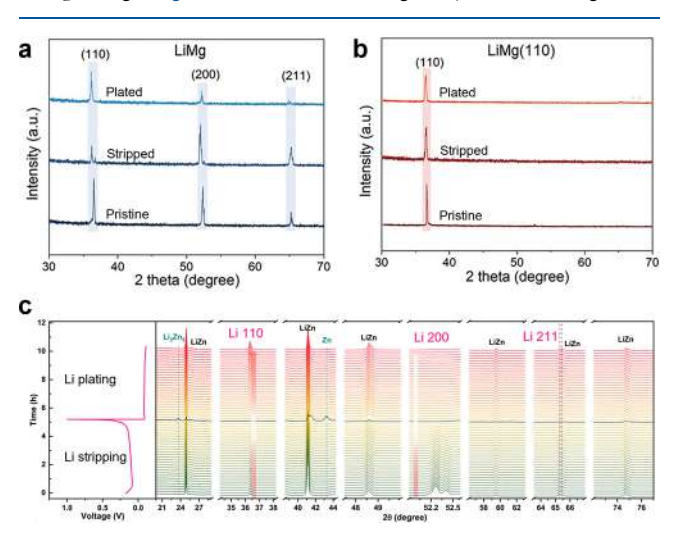


Figure 17. Li-alloy strategies for preferred crystal growth of Li metal. Evolution of the XRD patterns during electrochemical stripping and plating of (a) polycrystalline LiMg and (b) single-crystalline LiMg(110). Reproduced with permission from ref 111. Copyright 2025 John Wiley and Sons. (c) Evolution of XRD patterns of the Li/LiZn@Cu anode. Reproduced with permission from ref 112. Copyright 2024 Springer Nature.

maintained (110) peaks during stripping and plating (Figure 17b). This result indicates that careful control of crystal orientation of highly lithiophilic Li-alloys may still be necessary for faceted growth of Li metal.

Non-solid-solution-based Li-alloys were also reported to facilitate the crystal growth of Li metal. Lu et al. reported a facile fabrication of Li/LiZn and Li₂ZnCu₃ composite by introducing Zn into molten Li on Cu substrate (Li/LiZn@Cu) as the anode. From the calculation result, the LiZn(110) facet showed an ~0.03 eV lower Li diffusion barrier compared to the Li(100) facet, facilitating lateral transportation and deposition of Li. The *in situ* XRD analysis showed the disappearance of Li(200) during initial stripping process and appearance of

Li(110) during the plating process (Figure 17c). The mechanism and material selection criteria of the preferential growth of Li(110) on a Li-alloy substrate were further elaborated in other works using different Li-alloys. Liu et al. reported a Li–Li₂₂Sn₅ dual-phase alloy anode with a Li(110) and Li₂₂Sn₅(822). The low lattice mismatch (<1%) between these two facets promoted a preferential growth of Li(110) on the Li₂₂Sn₅(822) surface. Similarly, Chen et al. reported a dual-phase alloy anode with Li(110) and In₃Li₁₃(311) facets, which showed a low lattice mismatch of 2.2%. The combined effects of high lithiophilic Li-alloy materials and low lattice mismatch of non-solid-solution-based Li-alloys enabled a preferential deposition of (110)-textured Li metal during electrochemical operation, which enables dense deposition and stable cycling performance.

3.2. Li-Free Substrates for Li Crystal Growth

3.2.1. Single-Crystalline Cu Substrate: Facets. A Li-free (or anode-free) system is of the greatest interest due to its highest energy density. A Cu substrate has been widely used as a current collector to directly deposit Li metal. As the Li metal anode exhibits different crystallographic orientations, a commercial Cu substrate is also formed of different crystal orientations (Figure 18a). Ujihara et al. reported preferential

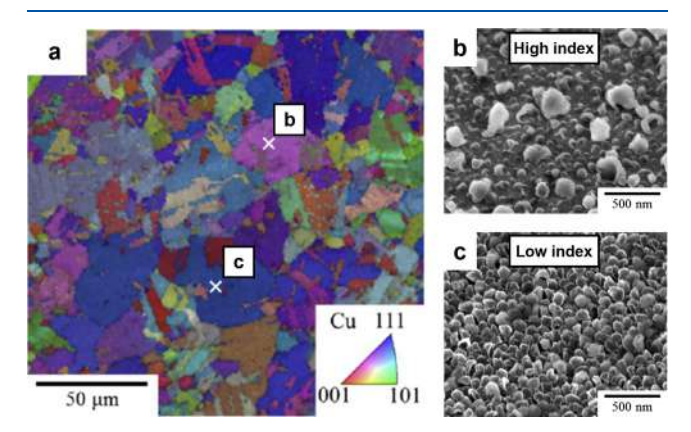


Figure 18. Preferential nucleation and growth of Li on a Cu substrate. (a) EBSD IPF map of Cu showing polycrystalline orientation. SEM images after Li deposition with 0.1 mAh cm $^{-2}$ on areas with a (b) high-index orientation and (c) low-index Cu(111) orientation. Reproduced with permission from ref 117. Copyright 2017 American Chemical Society.

nucleation and growth of Li metal on different Cu orientations. 117 Specifically, Li nucleation was observed to occur less on the high-index orientation surface (Figure 18b) compared to the low-index orientation surface of Cu(111) (Figure 18c). This nonuniform, preferential Li nucleation could lead to less dense Li deposition, requiring further understanding and engineering of Cu substrate to enable uniform deposition.

Mao et al. reported a faceted Cu substrate by electrochemical modification of a pristine Cu substrate. ¹¹⁸ The rough surface of pristine Cu was modified to a relatively smooth surface with larger polyhedral crystals with mostly (100) orientation, where pristine Cu consisted of mostly a (111) orientation. It was found that Cu(100) has a low lattice mismatch with Li(110), and the faceted Cu substrate also showed high lithiophilicity with a lower contact angle with molten Li metal. As a result, the faceted Cu substrate showed reduced nucleation overpotential and improved electrochemical performance compared with the pristine Cu substrate.

Xie et al. also showed that Cu(110) enabled favorable Li deposition compared to a commercial polycrystalline Cu substrate. The *ex situ* SEM after Li deposition at various areal capacities showed a uniform and dense deposition for Cu(110), whereas preferential island-like deposition along grain boundaries was observed in polycrystalline Cu. Accordingly, the single-crystalline Cu(110) showed much lower nucleation overpotential, higher Coulombic efficiencies, and capacity retention compared to a polycrystalline Cu substrate.

Although a faceted Cu substrate clearly showed a more favorable Li deposition compared to a nonfaceted substrate, which orientation of Cu is most favorable is still unclear. Kim et al. further reported a systematic comparison of low-index orientations of Cu substrates. 120 The voltage profile during the early stage of Li deposition showed that Cu(100) had the lowest nucleation overpotential and highest growth potential compared with (110) and (111). This indicates that both Li nucleation and growth were most favorable on Cu(100) compared to other low-index orientations.

Zheng et al. further conducted a comprehensive MD simulation of different Cu orientations. When the Cu surface is covered with one layer of Li, the potential energy surface flattens for Cu(100) and (111) whereas it fluctuates for Cu(110) (Figure 19a). The increased potential energy variance

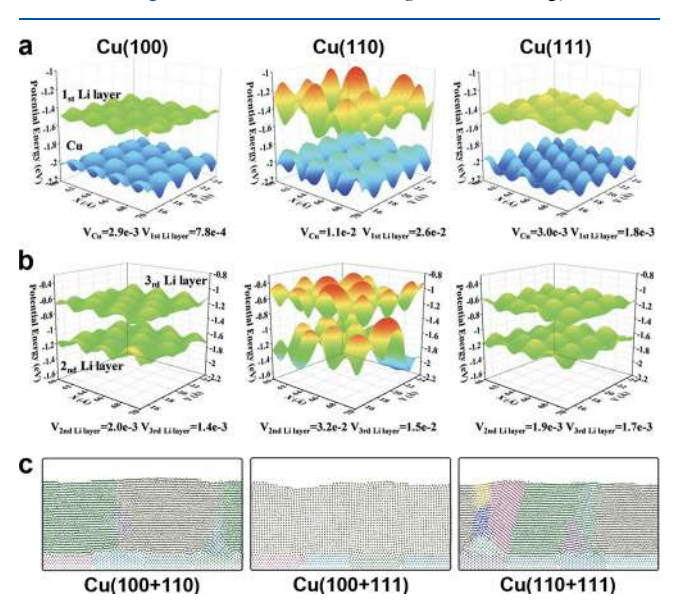


Figure 19. Molecular simulation of the Li surface on different Cu orientations. Potential energy surface diagram of (a) first Li layer and (b) second and third Li layers on Cu(100), Cu(110), and Cu(111). (c) Grain analysis of Li deposition on different binary combinations of polycrystalline Cu surface. Reproduced with permission from ref 121. Copyright 2023 John Wiley and Sons.

indicates that the movement of Li atoms is restricted, which makes it difficult to form Li(110), the most favorable surface of Li metal. This is because both Cu(100) and (111) have a low lattice mismatch with Li(110), but Cu(110) has a high lattice mismatch with Li(100). When the second and third layers of Li are further introduced, the potential energy surface remains flat for Cu(100) and (111) but uneven for Cu(110) (Figure 19b). As a result, the surface layers of Li atoms on Cu(100), (110), and (111) would follow the structural features of Li(110), (100), and (110), respectively. Furthermore, a large-scale simulation of homogeneous deposition on binary combinations of low index

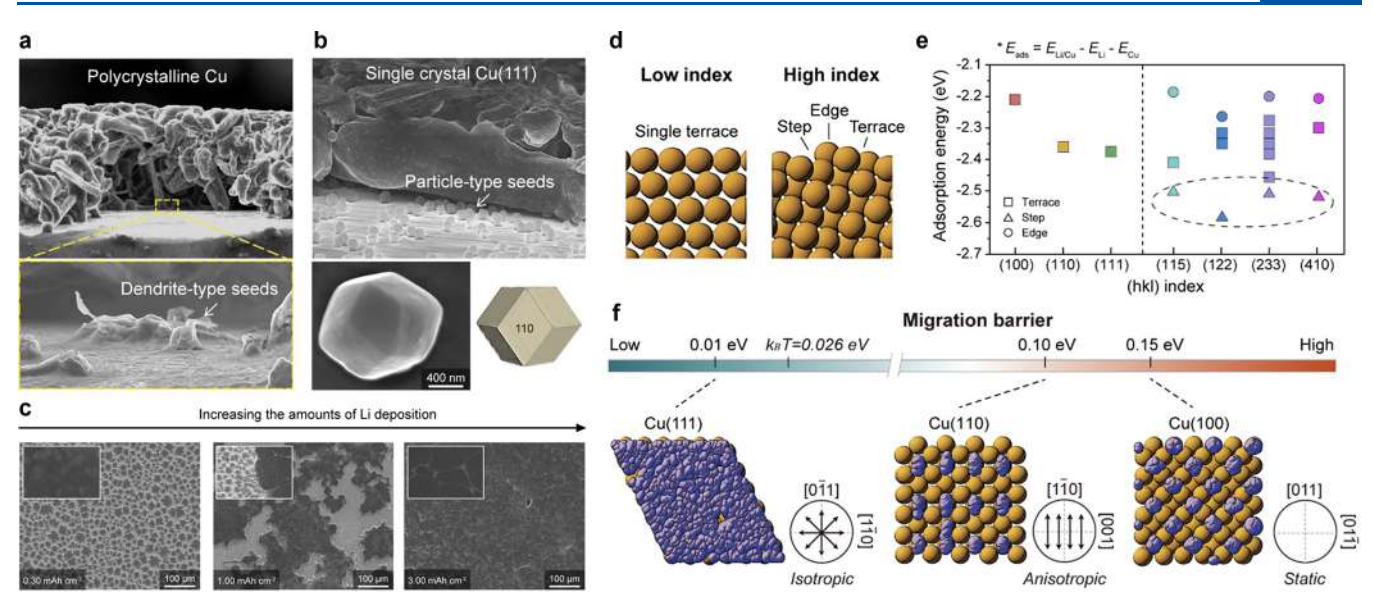


Figure 20. Single-crystalline Cu substrate for particle-type Li seeds. Side-view SEM images of Li deposits with 3.5 mAh cm⁻² on (a) polycrystalline Cu and (b) single-crystalline Cu(111). (c) SEM images of morphological evolution with increasing Li deposition. (d) Schematic showing surface features of low-index and high-index orientations of Cu. (e) Li adsorption energy on diverse low-index and high-index Cu. (f) Li migration barriers for all low-index surfaces and motion of Li adatoms computed using an ab initio molecular dynamics (AIMD) simulation. Reproduced with permission from ref 60. Copyright 2024 The Royal Society of Chemistry.

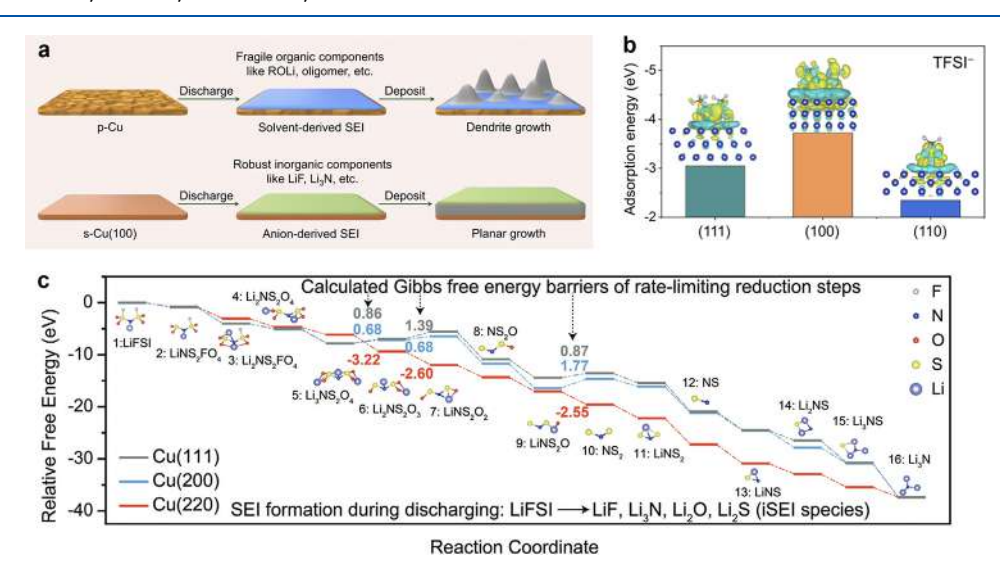


Figure 21. SEI formation on different orientations of Cu. (a) Schematics comparing SEI formation on polycrystalline Cu and single-crystalline Cu(100). (b) Adsorption energy of TFSI $^-$ on different orientations of the Cu substrate. Reproduced with permission from ref 123. Copyright 2024 John Wiley and Sons. (c) Gibbs free energy diagram of the decomposition reaction of LiFSI to LiF, Li₃N, Li₂O, and Li₂S on Cu(111), (200), and (220). Reproduced with permission from ref 124. Copyright 2025 John Wiley and Sons.

Cu facet was conducted (Figure. 19c). It was shown that deposited Li exhibited no grain boundaries or defects without Cu(110), which could be a key design consideration of the Cu substrate for growth of defect-free single-crystalline Li metal.

Although previous works have demonstrated uniform and dense Li deposition by modifying the crystallographic orientation of Cu substrates, precise control of Li crystal growth has not been realized. Lee et al. reported a successful growth of single-crystalline Li seeds on Cu(111) orientation. The nonuniform Li metal nucleation on polycrystalline Cu led to dendrite-type seeds that resulted in porous Li deposits (Figure 20a). Single-crystalline Cu(111), on the other hand, yielded particle-type Li seeds with a rhombic dodecahedron shape, the most thermodynamically stable polymorph of a body-centered

cubic (BCC) structure (Figure 20b). With increasing Li deposition, these particle-type seeds coalesced into 2D Li islands, which further expanded horizontally, eventually forming a dense, uniform Li deposit (Figure 20c). Li adsorption energy was calculated on both low-index and high-index orientations of Cu (Figure 20d,e). Cu(111) showed the lowest adsorption energy among low-index orientations, whereas the step site of all high-index orientations showed an even lower adsorption energy than Cu(111). Li migration barrier was further calculated for low-index orientations, and Cu(111) showed the near-zero migration of 0.01 eV with isotropic migration pathways (Figure 20f). These results indicate that Cu(111) not only favors Li adsorption but also facilitates migration of the Li adatom, enabling uniform Li deposition. It should be noted that despite

lower adsorption energies on high-index orientations, their migration barriers were significantly higher, resulting in nonuniform Li deposition. Also, the work showed that growth of rhombic dodecahedral Li seeds on Cu(111) was independent of different electrolyte chemistries, including dual-salt, etherbased, localized, highly concentrated, and weakly solvating electrolytes, indicating the dominant effect of substrate for Li seed growth.

3.2.2. Single-Crystalline Cu Substrate: SEI. Thermodynamically, SEI formation occurs prior to Li nucleation due to reduction of the electrolyte. Thus, it is also important to understand the electrolyte decomposition behavior on different orientations of Cu. Ujihara et al. reported SEI formation on different low-index Cu orientations. 122 After one cycle of cyclic voltammetry (CV), three low-index orientations of Cu were selected for auger electron spectroscopy (AES) analysis. It showed that the Cu signal was strong in the order Cu(111), Cu(001), and Cu(101), which could be indicative of a thinner SEI layer. X-ray photoelectron spectroscopy (XPS) was further conducted on single-crystalline Cu substrates after one cycle of CV. Li 1s spectra showed a relatively small LiF peak, and Cu $2p_{3/2}$ showed an obvious Cu metal peak for Cu(111). This result suggests that the thickness of the SEI layer could be different depending on the orientations of Cu, indicating preferential electrolyte decomposition.

Chen et al. reported properties of SEI layers on polycrystalline Cu and single-crystalline (111) and (100) faceted Cu. 123 It was found that single-crystalline Cu favored to form anion-derived SEI, resulting in planar growth of Li compared to dendrite growth for polycrystalline Cu (Figure 21a). The calculation results suggested that Cu(100) had the highest adsorption energy for bis(trifluoromethanesulfonyl)imide (TFSI) anion, indicating more formation of anion-derived SEI (Figure 21b). Time-of-flight secondary ion mass spectrometry (ToF-SIMS) and Young's modulus measurements were further conducted to confirm the distribution of inorganic (LiF₂⁻) and organic (C₂HO⁻) contents and mechanical property of SEI layers, respectively. The robust inorganic-rich SEI could maintain mechanical rigidity during Li plating and stripping compared to the soft organic-rich SEI, enhancing electrochemical reversibility and stability. Chen et al. elucidated the decomposition reaction kinetics involved in inorganic-rich SEI on different orientations of $\operatorname{Cu.}^{124}$ The Gibbs free energy calculated for decomposition reactions of lithium bis(fluorosulfonyl)imide (LiFSI) to form inorganic SEI species, such as Li₃N, Li₂O, and Li₂S, showed that both Cu(111) and (200) had endothermic reduction steps with high positive Gibbs free energy barriers, whereas Cu(220) had entirely spontaneous exothermic reaction with negative Gibbs free energy, suggesting catalyzing ability of LiFSI decomposition and inorganic SEI formation (Figure 21c). XPS depth profiling further confirmed that the SEI layer of the Cu(111)-rich substrate showed high organic contents, while the Cu(220)-rich substrate showed high organic on top layer and inorganic on bottom layer. These results show that not only Li deposition but also SEI formation could significantly vary depending on different Cu orientations, which requires further systematic studies for different electrolyte chemistries.

3.2.3. Other Substrates. While modifying the crystallographic orientation of Cu substrates effectively demonstrated improved cycling stability of Li plating and stripping, the orientations are limited to (100), (110), and (111) for low-index Cu facets. A research trend has been further extended to exploring other types of substrates to control the crystal growth

of Li metal. Wei et al. demonstrated growth of Li along (110) orientation by using a reduced graphene oxide (rGO) template (Figure 22a). 125 The length of two carbon hexagons (4.92 Å)

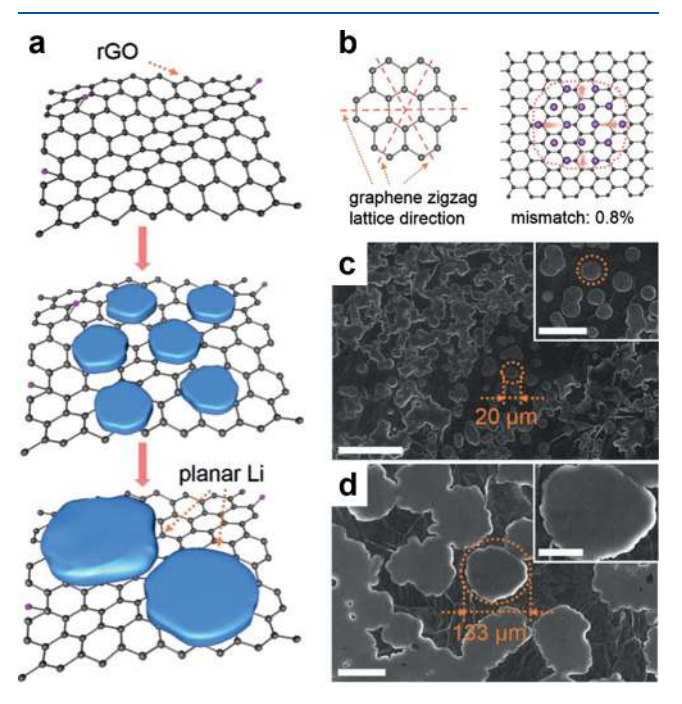


Figure 22. Growth of planar Li metal on the rGO substrate. Schematics showing (a) Li growth process on rGO and (b) lattice direction and mismatch of rGO with Li metal. SEM images of deposited Li with (c) 1 mAh cm⁻² and (d) 5 mAh cm⁻². Reproduced with permission from ref 125. Copyright 2020 John Wiley and Sons.

along the graphene zigzag direction matched well with that of two Li atoms along the (110) plane (4.96 Å), yielding a low lattice mismatch of 0.8% (Figure 22b). This low lattice mismatch between Li(110) and graphene minimized the interfacial free energy barrier, as discussed in Section 2.3.2. As a result, Li deposits showed dense, planar growth at areal capacities of 1 and 5 mAh cm $^{-2}$ (Figure 22c,d). Additionally, from XRD analysis, Li deposited on rGO substrate showed a higher relative intensity ratio of (110)/(200) compared to that of pristine Cu substrate (34.1 vs 7.63), indicating more oriented growth of Li metal.

Liu et al. demonstrated a growth of single-crystalline Li seeds on a lithiophobic FeF₃-coated substrate. 126 The FeF₃ layer converted into Fe and LiF upon electrochemical cycling, in which Fe nanodomains served as a homogeneous nucleation site and LiF promoted fast Li diffusion (Figure 23a). The growth of crystalline Li seeds was observed even at a low current density of 0.5 mA cm⁻² (Figure 23b). High-angle annular dark-field (HAADF) TEM image with energy dispersive spectroscopy (EDS) mapping of C, O, F, S, and N also confirmed a thin, conformal SEI layer on the Li crystal (Figure 23c). 3D cryo-TEM tomography further showed a nearly elongated hexagonal bipyramidal shape of a Li crystal, which had all low-energy (110) facets (Figure 23d). The resulting single-crystalline Li seeds enabled much dense Li deposition compared to typical Cu current collectors, thereby achieving improved cycling performance. Song et al. reported oriented growth of Li metal on a LaF3coated substrate. Similar to FeF₃, LaF₃ converted to La and LiF but La worked as a dopant in Li metal, which changed the preferred growth orientation from (110) to (200). It was shown

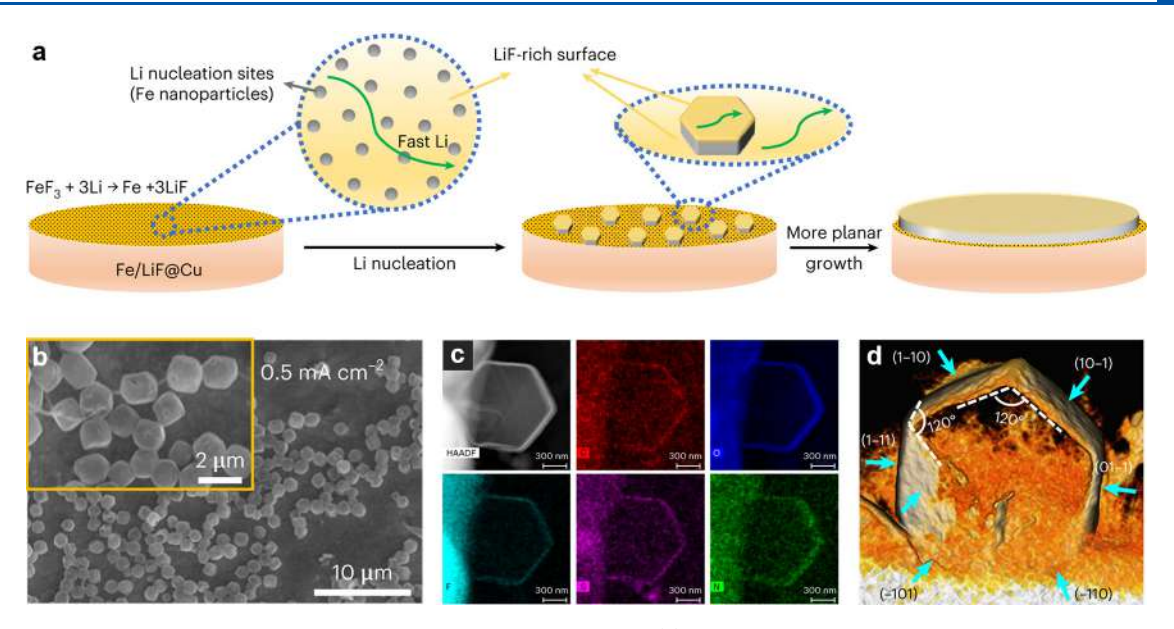


Figure 23. Growth of single-crystalline Li seeds on a lithiophobic FeF₃ substrate. (a) Schematic showing Li nucleation and growth mechanisms. (b) SEM images of Li deposited at 0.5 mA cm⁻² with 0.1 mAh cm⁻². (c) HAADF image with EDS maps and (d) 3D cryo-TEM tomography of hexagonal-shaped single-crystalline Li metal. Reproduced with permission from ref 126. Copyright 2023 Springer Nature.

from surface energy calculation that Li₉₅La had the lowest surface energy on the (200) orientation (19.0564 meV Å⁻²), whereas pristine Li had the lowest surface energy on the (110) orientation (30.9019 meV Å⁻²). The lower surface energy by La doping enabled growth of Li metal with (200) orientation, enabling a dense Li deposition and extended cycling life compared to the pristine Cu substrate.

Although many materials have been explored as nucleation sites for Li deposition, tuning the size and density of the nucleation sites is challenging. Liu et al. further demonstrated that the spatial distribution of nucleation sites could be finely tuned by different carbon materials and carbon concentrations in the polymer composite. 128 It was discovered that defects on carbon materials could act as effective nucleation sites for the crystal growth of Li metal (Figure 24a). Raman spectra showed intensity ratios of the D band to G band (I_D/I_G) , also known as defect ratios (Figure 24b). The defect ratio increased in the order of graphite, graphene, super P (SP), ketjen black (KB), and carbon nanotube (CNT), with values of 0.33, 0.88, 1.01, 1.25, and 1.29, respectively. Interestingly, the size of Li seeds decreased with increasing defect ratio, where Li deposited on SP, KB, and CNT showed a similar morphology to single-crystalline Li particles as previously reported (Figure 24c). Using KB as a model carbon material, the effects of defect ratio and carbon ratio as well as the nucleation mechanism on defect sites were also investigated. Consequently, a KB-polymer composite enabled dense Li deposition and extended cycling life compared to a SP-polymer composite or commercial Li metal in both half cells and full cells.

3.3. Effect of Operation Conditions

3.3.1. Current Density. In addition to cell design parameters, different operation conditions were investigated for the crystal growth of Li metal. Overpotential directly affects the size and density of nuclei as discussed in Section 2.3.1, and current density is the most common operation parameter affecting overpotential in typical galvanostatic cycling. Cui et al. elucidated the correlation between overpotential and nuclei size and number density. ⁶⁴ It was found that the nuclei size is linearly

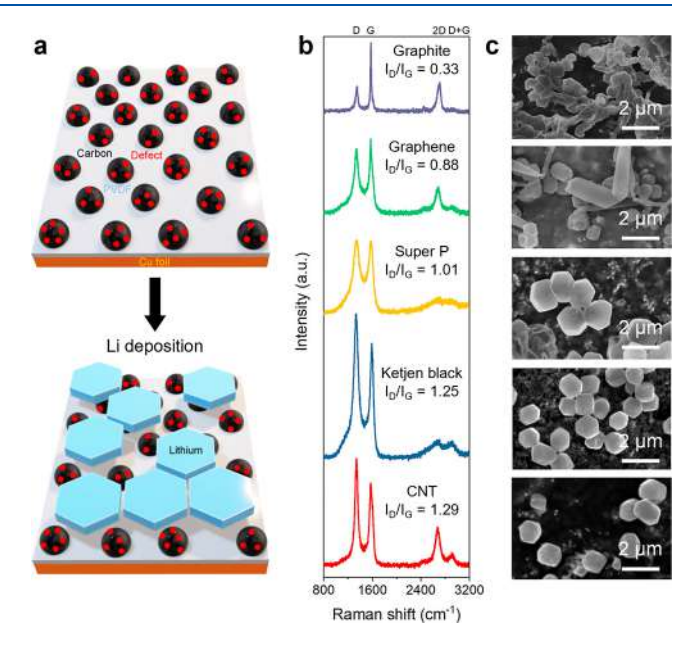


Figure 24. Growth of crystalline Li seeds on carbon defects. (a) Schematic showing Li nucleation on a carbon—polymer composite substrate. (b) Raman spectra of carbon materials with different D band to G band intensity ratios. (c) Corresponding SEM images of deposited Li seeds at 3 mA cm⁻² with 0.1 mAh cm⁻². Reproduced with permission from ref 128. Copyright 2024 American Chemical Society.

proportional to the inverse of nucleation overpotential, and the number density of nuclei is proportional to the cubic power of the nucleation overpotential. In other words, with increasing current densities, smaller and more Li seeds were formed in the early nucleation stage. Although high current density enabled uniform and sparse distribution of Li seed layers, further increasing the areal capacity resulted in deposition of porous seeds instead of dense deposits. A strategy of applying a short high current density (10 mA cm⁻² at 0.02 mAh cm⁻²) was proposed to form uniform Li seed layers before the desired

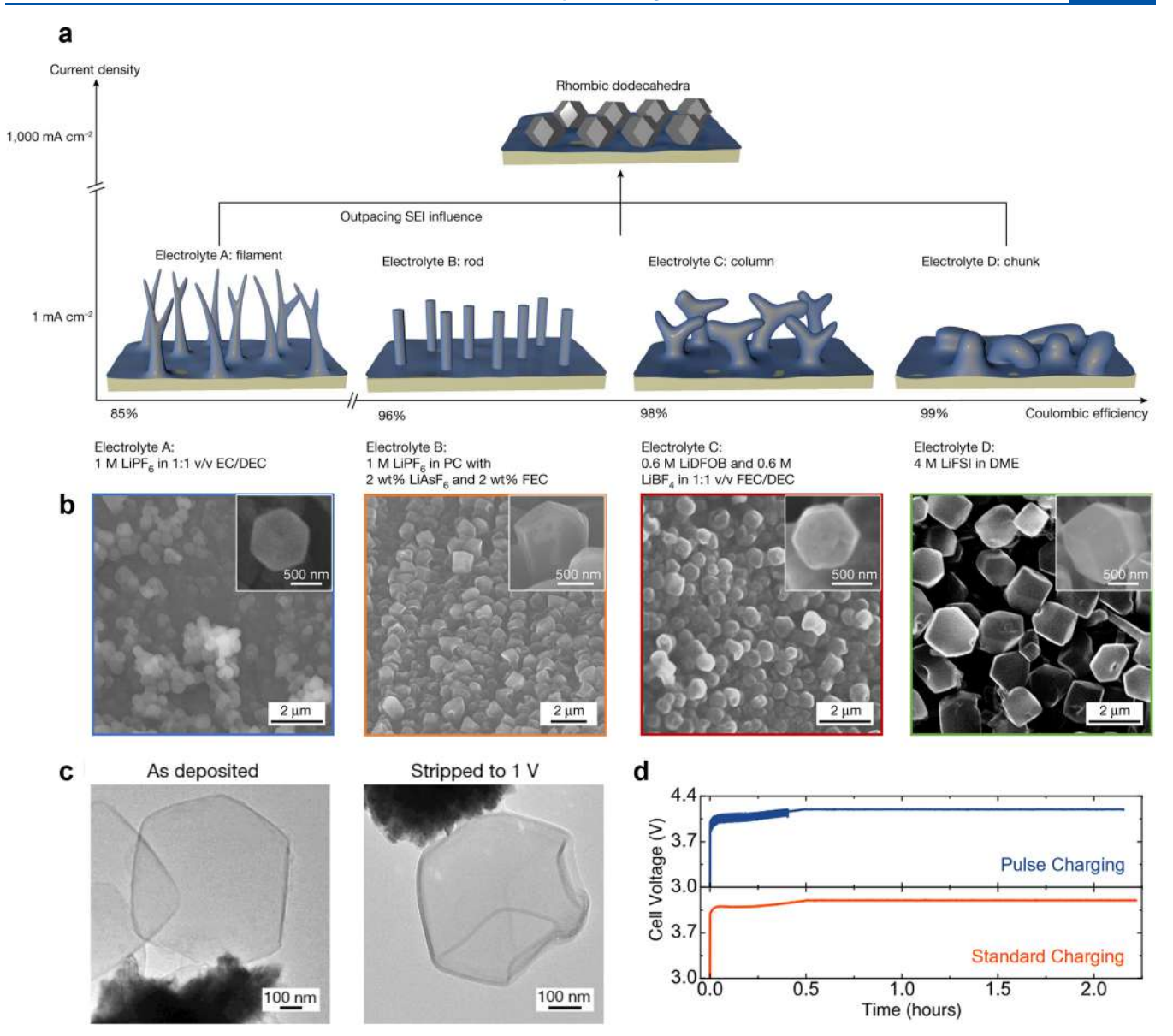


Figure 25. Current density effects on growth of single-crystalline Li metal. (a) Schematic showing electrolyte-independent behavior of single-crystalline Li metal growth under ultrahigh current density. (b) SEM images showing single-crystalline Li metal particles in different electrolyte systems. (c) Cryo-TEM images of a deposited and stripped Li particle showing poor contact with the Cu substrate. Reproduced with permission from ref 129. Copyright 2023 Springer Nature. (d) Voltage profiles of LillNCM full cell with pulse charging and standard charging protocols. Reproduced with permission from ref 130. Copyright 2022 American Chemical Society.

cycling current density, which alleviated the nucleation overpotential.

Li et al. further carried out the current density effect to grow single-crystalline Li metal under an ultrahigh current density of 1000 mA cm⁻². ¹²⁹ In the high current density regime, the common morphology dependence on electrolyte chemistry disappeared due to the outpaced formation of the SEI, resulting in the deposition of single-crystalline Li particles (Figure 25a). Li particles showed a rhombic dodecahedra shape consisting of only (110) facet exposed surfaces (Figure 25b). Despite the facile formation of single-crystalline Li particles by simply increasing the current density, these particles exhibited poor contact with the current collector and could not be fully stripped (Figure 25c). To take full advantage of single-crystalline Li seeds, a pulse-based charging protocol was demonstrated that showed improved cyclability compared to the standard charging protocol (Figure 25d). ¹³⁰

3.3.2. Temperature. Temperature is another controllable operation condition in practical battery cycling. Cui et al. reported a temperature dependence of Li nucleation. 65 The nucleation overpotential increased with lowering temperature as similarly observed with increasing current density.⁶⁴ Consequently, distinct Li particles were observed at low temperatures from -20 to 0 °C (Figure 26a-c). These particles started to merge at moderate temperatures from 10 to 30 °C (Figure 26d-f), and distinct merged islands were formed at high temperatures from 40 to 60 °C (Figure 26g-i). Despite the uniform seed formation at low temperatures, it was concluded that higher temperatures resulted in more stable cycling due to a more ordered multilayered structure of the SEI and reduced surface area that avoided unwanted side reactions of the electrolyte. Therefore, high temperatures assist the coalescence of Li metal during the growth process, minimizing surface area and enabling dense deposits. At low temperatures, on the other

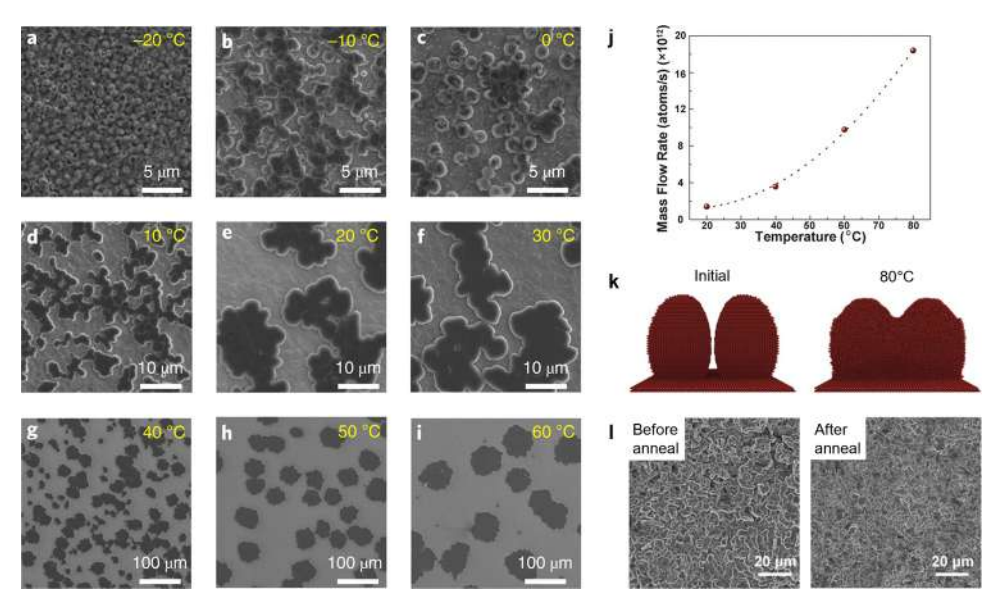


Figure 26. Temperature effects on the nucleation and growth of Li metal. SEM images of Li deposited at (a) -20 °C, (b) -10 °C, (c) 0 °C, (d) 10 °C, (e) 20 °C, (f) 30 °C, (g) 40 °C, (h) 50 °C, and (i) 60 °C at 0.25 mA cm⁻² with 0.15 mAh cm⁻². Reproduced with permission from ref 65. Copyright 2019 Springer Nature. (j) Migration mass flow rate of Li atoms as a function of temperature predicted with MD. (k) MD simulation of Li dendrite particles at the initial state and after ~ 50 ps at ~ 80 °C. (l) SEM images of Li dendrites before and after thermal annealing at ~ 70 °C for 3 days in an Ar environment. Reproduced with permission from ref 138. Copyright 2018 American Association for the Advancement of Science.

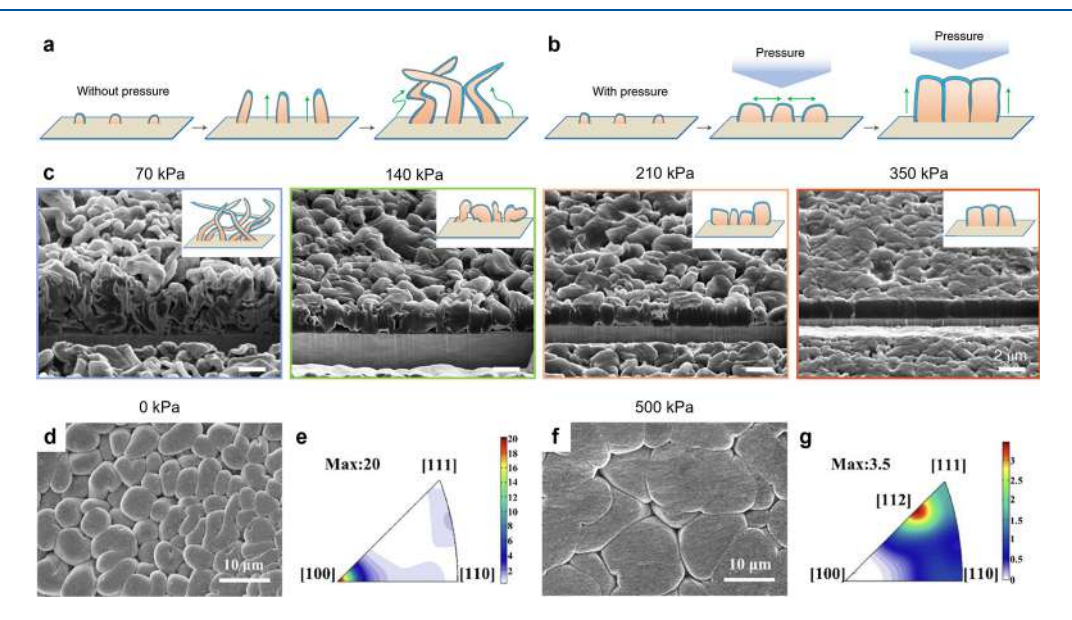


Figure 27. Pressure effects on the growth of Li metal. Schematics showing growth of Li metal (a) without and (b) with pressure. (c) Cyro-FIB-SEM images of Li deposited at 70, 140, 210, and 250 kPa at 2 mA cm⁻² with 0.333 mAh cm⁻². Reproduced with permission from ref 74. Copyright 2021 Springer Nature. (d) SEM image and (e) IPF map of Li deposited without pressure at 5 mA cm⁻² with 20 mAh cm⁻². (f) SEM image and (g) IPF map of Li deposited with a 500 kPa pressure at 5 mA cm⁻² with 20 mAh cm⁻². Reproduced with permission from ref 139. Copyright 2023 Elsevier.

hand, electrolyte engineering was found be effective for dense deposition and improved electrochemical reversibility. ^{131–137}

Koratkar et al. further showed that high temperatures could facilitate the healing of Li dendrites. The migration mass flow rate of Li atoms showed that the surface diffusion of Li is strongly temperature-dependent and dramatically increases above 40 °C (Figure 26j). This behavior is very similar to the Ostwald ripening discussed in Section 2.2.2, where the chemical potential difference serves as a driving force for surface migration. The MD simulation also showed the merging of two Li dendrite particles after annealing at ~80 °C for ~50 ps (Figure 26k). The experimental results confirmed the merging of Li dendrite

particles after thermal annealing of Li dendrites at \sim 70 °C for 3 days in an Ar environment (Figure 26l). These results show that high temperatures are more favorable during the growth process of Li deposition.

3.3.3. Pressure. Pressurization is important to maintaining electrical contact between the electrode active materials and current collectors. Meng et al. reported that stack pressure directly affects the growth morphology of Li metal.⁷⁴ Without pressure, Li grew freely in a vertical direction perpendicular to the current collector, forming whisker-shaped Li deposits (Figure 27a). With pressure, Li grew in a lateral direction along with the current collector, forming dense Li deposits

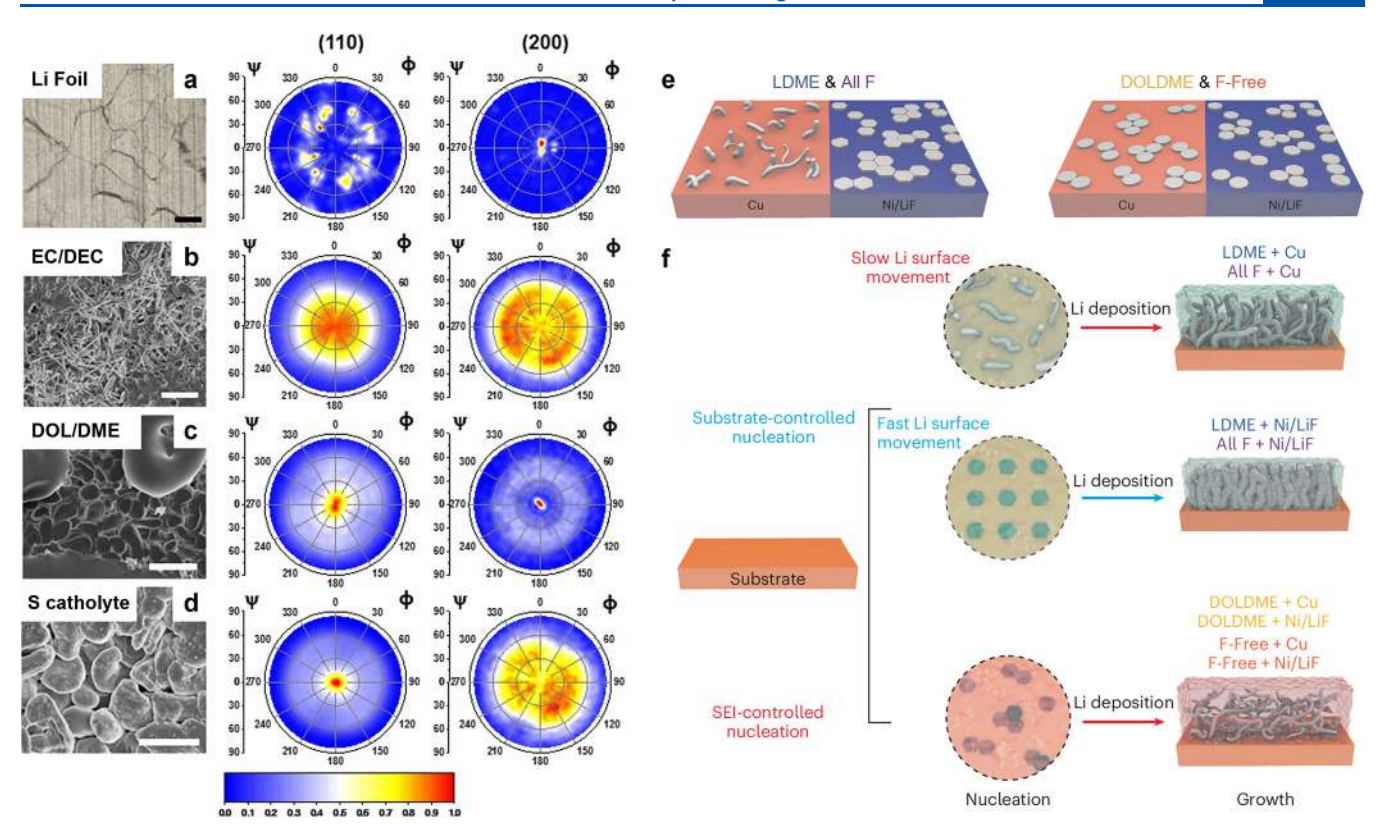


Figure 28. Liquid electrolyte effects on the crystal growth of Li metal. SEM image and pole-figures of Li(110) and (200) of (a) commercial Li foil, Li deposited in (b) EC/DEC 1 M LiPF₆, (c) DOL/DME 1 M LiTFSI with 1% LiNO₃, and (d) sulfur catholyte 5 M S₈ in DOL/DME 1 M LiTFSI with 1% LiNO₃. Reproduced with permission from ref 140. Copyright 2017 National Academy of Sciences. (e) Schematics showing distinct morphologies of Li crystal seeds with different electrolyte systems on Cu and Ni/LiF nanocomposite substrates. (f) Substrate-controlled nucleation and SEI-controlled nucleation depending on electrolyte chemistry. Reproduced with permission from ref 152. Copyright 2025 Springer Nature.

(Figure 27b). Cryogenic focused ion beam-SEM (Cryo-FIB-SEM) was utilized on Li metal deposited at uniaxial pressures of 70, 140, 210, and 350 kPa (Figure 27c). It showed that dendritic Li metal with a high surface area was formed at a low pressure of 70 kPa, whereas dense Li metal with minimal surface area was formed at a high pressure of 350 kPa.

Hu et al. further reported the effect of pressurization on the crystal orientation of Li metal. Without pressure, Li deposits with a small grain size were formed (Figure 27d), which showed a dominant (100) orientation from the IPF map (Figure 27e), a typical indication of dendrite growth. With a pressure of 500 kPa, Li deposits showed larger grain size with the evidence of merging (Figure 27f), and the IPF map also showed a disappearance of the (100) orientation and appearance of (112) and (110) orientations (Figure 27g). These results indicate that pressure affects not only morphology, but also the growth orientation of Li metal deposition.

3.4. Impact of Electrolyte Systems on Li Crystal Growth

3.4.1. Liquid Electrolyte. In a liquid system, the electrolyte is the most critical factor determining the cyclability of the Li metal anode. Cui et al. reported different crystallographic textures of Li metal depending on different electrolytes. ¹⁴⁰ Compared to commercial Li foil, Li deposited in the EC/diethyl carbonate (DEC) 1 M LiPF₆ electrolyte showed a rough surface from SEM images (Figure 28a,b). The difference was also observed in pole-figure analysis, where Li deposited in EC/DEC electrolyte showed a broad intensity distribution, indicating that the texture is not clearly pronounced. On the other hand, Li deposited in dioxlane (DOL)/dimethoxyethane (DME) (1 M

LiTFSI with 1% LiNO₃) and sulfur catholyte electrolytes (5 M S_8 in DOL/DME 1 M LiTFSI with 1% LiNO₃) showed denser, round-shaped Li deposits from SEM images (Figure 28c,d). The pole-figure maps also showed strong (110) intensity in the center, indicating a high (110) orientation of Li deposits.

It has been widely reported that the liquid electrolyte directly affects the SEI composition, and thus the microstructure and cycling stability of Li metal anode. T5,141–144 Despite different electrolyte design strategies such as salt concentrations and solvation structures to improve the performance of Li metal anode, there has been a lack of studies on the crystal growth of Li metal depending on electrolyte chemistries. Since almost all electrolytes get reduced toward Li metal, 150,151 decoupling the effects of the SEI and crystal orientation remains challenging across different electrolyte systems. Previous works on substrate and current density strategies showed negligible dependence of electrolyte systems on the growth of single-crystalline Li seeds.

Recently, Liu et al. reported the effects of different electrolyte chemistries and substrates on nucleation and growth of single-crystalline Li seeds. ¹⁵² As illustrated in Figure 28e, distinct Li nucleation morphologies were observed for electrolyte systems—a localized high-concentration electrolyte (LDME), an all-fluorinated carbonate electrolyte (All F), a dilute ether electrolyte with LiNO₃ additive (DOLDME), and a fluorine-free carbonate electrolyte (F-Free)—on Cu and Ni/LiF nano-composite substrates. To be specific, LDME and All F electrolytes showed substrate-controlled nucleation, where the nucleation process is not limited by SEI transport and charge-transfer reaction but the Li nuclei formation and interfacial

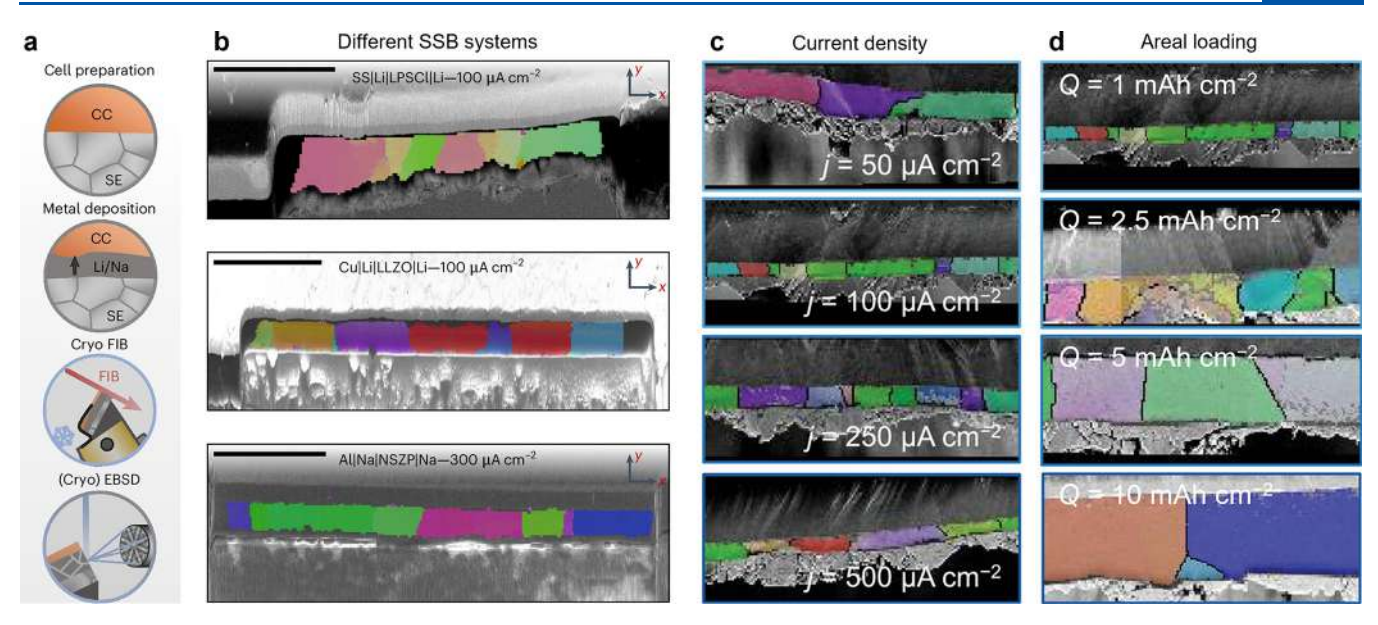


Figure 29. Growth and characterization of Li metal in SSBs. (a) Schematic showing the characterization procedure of probing the crystal orientation of Li metal in SSBs. Reproduced with permission from ref 157. Copyright 2024 Springer Nature. Cross-sectional IPF maps of (b) different SSB systems, (c) Li deposited at different current densities with 1 mAh cm⁻², and (d) Li deposited at different areal capacities at 100 μA cm⁻². Reproduced with permission from ref 158. Copyright 2024 John Wiley and Sons.

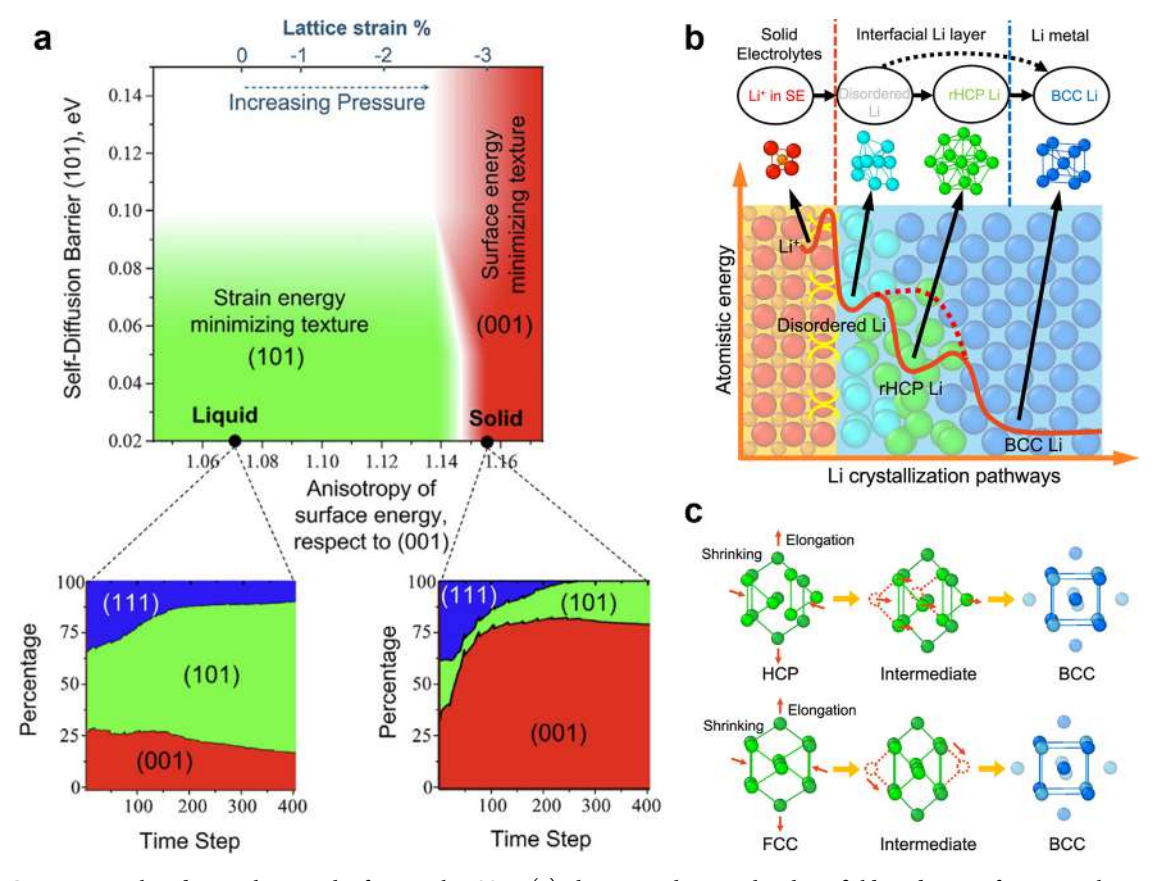


Figure 30. Computational studies on the growth of Li metal in SSBs. (a) Phase map showing the phase-field prediction of Li grain selection growth in liquid and solid systems. Reproduced with permission from ref 160. Copyright 2025 Elsevier. (b) Schematic showing multiple-step pathways of Li crystallization in SSBs. (c) Transition steps of HCP or FCC configuration to BCC configuration. Reproduced with permission from ref 161. Copyright 2023 Springer Nature.

transport of the substrate (Figure 28f). On the other hand, DOLDME and F-Free electrolyte showed SEI-controlled nucleation, in which the nucleation process is limited by the through-plane lithium transport of the SEI and charge-transfer

reaction due to organic-rich SEI. Upon continuous deposition on Ni/LiF substrate with a fast Li surface transport, LDME and All F electrolytes showed Li nucleation on the original seed layers, forming well-connected deposit structure, whereas

DOLDME and F-free electrolytes showed a new layer of Li crystal nucleation, leading to poorly connected layer-by-layer structure. This work elucidates the Li crystal nucleation modes by uncovering the effects of Li—substrate and Li—SEI interfaces on nucleation, highlighting the importance of electrolytes with favorable SEI composition for fast charge-transfer and substrates with fast Li adatom transport for stable and uniform nucleation.

3.4.2. Solid Electrolyte. Recently, solid-state batteries (SSBs) have emerged as a next-generation battery system due to their improved safety features compared to the conventional liquid system. 153–156 The Li metal SSB has also been a research focus due to its high energy density. However, due to the intrinsic nature of a buried interface unlike the liquid system, characterizing crystal orientation or even the morphology of the Li anode is challenging. Janek et al. reported a characterization procedure for imaging the crystal structure of Li metal in SSB using EBSD. 157 After a cell is assembled and cycled, FIB and EBSD are conducted under cryogenic conditions to minimize chemical reactivity and beam damage (Figure 29a). This method is applicable to various SSB systems such as a Li metal anode using argyrodite-type Li₆PS₅Cl (LPSCl) or oxidetype Li₇La₃Zr₂O₁₂ (LLZO) solid electrolytes, and even a SSB using a Na metal anode (Figure 29b). Using this method, Janek et al. further investigated the effects of current density and areal capacity in anode-free Li SSB. 158 Unlike the liquid system, in which a high current density was reported to induce small grains of Li deposition, no clear correlation was observed for the solid system (Figure 29c). Interestingly, the grain size of deposited Li metal increased with increasing areal capacity (Figure 29d). This suggests that Li growth and crystallization mechanisms could be entirely different for solid electrolytes compared to those for liquid electrolytes. Additionally, the same group recently showed that Li crystal orientations and grain sizes differed significantly in the presence of various alloy materials (Au, Ag, Bi) as an interlayer, highlighting potential strategies to control crystal growth in SSB systems.¹

Meng et al. reported a study predicting the grain selection of Li metal in a solid electrolyte compared to in a liquid electrolyte. The grain selection of Li growth was illustrated in liquid and solid systems using the phase-field prediction (Figure 30a). With lower pressure applied, the liquid system would favor a strain-energy-minimizing texture of (101) that exhibits the lowest Li diffusion barrier (0.02 eV). On the other hand, with higher pressure applied, the solid system would favor a surface-energy-minimizing texture of (001) that exhibits the lowest surface energy. This thermodynamic consistent model was further confirmed with experimental results from FIB-EBSD, which showed more (001) orientation of Li metal in the solid system. Accordingly, amorphous Si as an interfacial layer was proposed for the growth of the (101) oriented Li metal.

While the Li deposition process can be described by classical nucleation theory in a liquid electrolyte, the crystallization pathways are hardly understood in a solid electrolyte. Mo et al. further reported MD simulations on how Li metal crystallizes at the interfaces with a solid electrolyte. If was found that Li crystallization is energetically favorable in multiple-step pathways, where disordered Li is formed from Li⁺ in a solid electrolyte that undergoes an intermediate state of a random mixture of hexagonal close-packed (HCP) and face-center cubic (FCC) before formation of a BCC configuration (Figure 30b). To be specific, HCP-Li or FCC-Li shrinks and elongates to move atoms to form BCC-Li (Figure 30c). This multiple-step pathway follows Ostwald's step rule, which suggests that the

higher energy intermediate phase forms first before the thermodynamically stable phase. Mo et al. also reported comprehensive computational works on the atomistic understanding of the interfacial layer of solid-electrolyte and Li metal. ¹⁶², ¹⁶³

In summary, after intense research efforts to stabilize and control the deposition of a Li metal anode, recent studies have reached a level of controlling the crystallographic orientation of the Li deposit. Novel strategies on substrate texture and chemistry, operating conditions, and electrolyte systems have shown effective control of growth of Li crystals, advancing toward a stable and high-energy density application of Li metal anodes.

4. ZN METAL ANODE

Li batteries face challenges in long-duration energy storage due to safety concerns, high costs, and limited resources. Meanwhile, commercial aqueous rechargeable batteries (e.g., lead-acid) fail to meet the necessary scale and cost requirements for extended storage. To address these issues, the development of rechargeable aqueous batteries has drawn much attention. Zn metal, with high theoretical gravimetric and volumetric capacities (820 mAh g $^{-1}$ and 5855 mAh cm $^{-3}$, respectively) is an ideal anode due to its affordability, environmental friend-liness, relative safety, and rich abundance. 164,165

Even though the Zn metal anode can undergo reversible electroplating/stripping reactions in acidic aqueous electrolytes, several scientific gaps still hinder the practical application of Zn-based aqueous batteries. To be specific, three main challenges for metallic Zn anodes are (1) dendritic formation due to unregulated Zn deposition behavior; (2) corrosion arising in acidic electrolyte systems; and (3) the undesired hydrogen evolution reaction (HER). In this section, we summarize the recent works mitigating the above issues using crystallographic engineering, with a focus on elucidating how those strategies control the nucleation and growth of Zn during the electrodeposition process. ^{166,167}

4.1. Epitaxial Zn Growth on Textured Interlayer

The epitaxial electrodeposition process, where a thin-film electrodeposit forms a coherent or semicoherent lattice interface with the substrate, is widely used in semiconductors. The singlecrystalline new phase (epilayer) exhibits a correlated orientation in relation to the substrate and low residual stresses. The strongest orientation correlations are achieved through directed nucleation and growth of the epilayer on a substrate that imposes minimal lattice strain. In 2019, Archer's pioneering work first realized Zn epitaxial growth on aligned graphene coatings over a stainless-steel substrate. 168 A semicoherent interface was formed considering that the lattice mismatch between graphene and Zn(002) is about 7% and thus enabled an energetically favorable Zn epitaxial deposition (Figure 31). Inspired by this work, substrates with a low lattice misfit with Zn are widely explored. Other 2D carbon materials, for example, Ndoped graphene oxide (GO), ¹⁶⁹ zeolitic imidazolate framework (ZIF-8) modified GO, ¹⁷⁰ and N/O codoped carbon, ¹⁷¹ are all suggested to facilitate an oriented Zn(002) deposition.

Transition metal carbides/nitrides (MXenes) are an alternative. Zhi et al. proposed the synthesis of a composite anode using flexible MXene flakes and Zn powders. Their research suggests that the lattice mismatch between ${\rm Ti_3C_2T_x}$ and ${\rm Zn(002)}$ is 10%. The semicoherent interface enabled a uniform Zn deposition while establishing a consecutive electronic

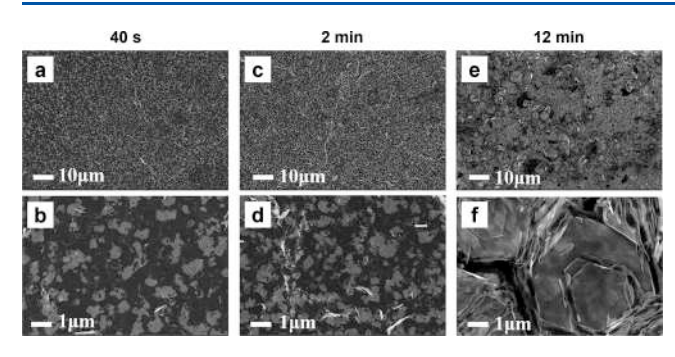


Figure 31. Epitaxial Zn growth on the textured interlayer. SEM images of Zn deposited on graphene-coated stainless steel with deposition times of (a,b) 40 s, (c,d) 2 min, and (e,f) 12 min. Reproduced with permission from ref 168. Copyright 2019 The American Association for the Advancement of Science.

transport channel to avoid electrical contact loss of Zn powders. Liu et al. reported Sn-modified ${\rm Ti_3C_2Cl_2}$ MXene. ¹⁷³ Besides the coherent MXene/Zn interface, Sn with high Zn-affinity also supplied low nucleation overpotential, excellent Zn affinity, and high conductivity, while -Cl terminations showed strong interaction with Zn atoms, resulting in a lower surface energy on the Zn(002) planes.

Beyond these, Guo et al. utilized 2D fluorinated covalent organic frameworks (FCOF), considering that F atoms in the FCOF film demonstrate the strongest interaction with the (002) crystal planes of Zn. 174 Luo et al. proposed the fabrication of a single-layer 1T-vanadium diselenide (1T-VSe2) film on graphene. 175 The film was subsequently employed as a zincophilic template for Zn epitaxial electrodeposition, as the in-plane lattice constant of VSe2 (2.6 Å) is very close to that of Zn(002) of 2.67 Å. Alshareef et al. proposed MoS2 as the substrate to study Zn metal deposition behavior due to their similar lattice structures. 176 They confirmed that the edge of MoS2 exhibited a Zn-deposition-inducing effect much stronger than that of the basal plane. In contrast, when deposited on MoS2 free of edges, the Zn film grew epitaxially with a high degree of orientation in both the in-plane and out-of-plane.

However, when employing 2D materials, the number of layers also has a significant influence on the electrochemistry and crystallographic orientation of electrodeposited Zn.¹⁷⁷ The presence of different layer numbers of graphene was found to alter electrochemical signatures during electrodeposition (Figure 32a-c). Density functional theory (DFT) calculations revealed electronic interactions between the substrate and deposit through 1- and 2-layer graphene, but inhibited charge transfer capability through 3-layer graphene. Similarly, Sun et al. found that multilayer graphene film could not render the desirable Zn(002) epitaxial texture, whereas the breakage during the transfer process unexpectedly created a unique pinhole deposition mode that facilitated the formation of smooth deposition layers over monolayer graphene (Figure 32d).¹⁷⁸

However, for single-layer 2D materials, it can be challenging to withstand the volume change during the repeated Zn plating-stripping process, especially under high areal capacity or extended cycling conditions. Additionally, voids could be generated during the Zn stripping process, which might induce strains and inhomogeneity at the interface. Therefore, significant efforts have been made toward interlayer designs involving inorganic/organic materials.

For the Zn-containing alloy interlayer design, Yang et al. introduced a 3D Cu-In alloy heterogeneous interface on Zn by

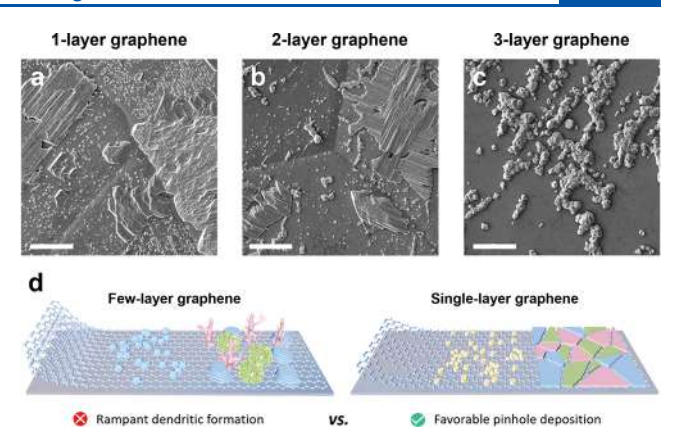


Figure 32. Distinct Zn deposition morphology on 2D materials with different numbers of layers. SEM images of Zn electrodeposited on (a) 1-layer graphene, (b) 2-layer graphene, (c) 3-layer graphene. Reproduced with permission from ref 177. Copyright 2024 American Chemical Society. (d) Schematic of different Zn deposition modes on employing few-layer and single-layer graphene film. Reproduced with permission from ref 178. Copyright 2024 John Wiley and Sons.

a chemical substitution method. The as-fabricated Cu–In interlayer possessed an anti-HER capability of In and the Zn-affinity of Cu, resulting in a preferred Zn(002) deposition with mitigated side reactions. Huang et al. proposed the fabrication of an interfacial lattice locking layer by electrocodepositing Zn and Cu, forming a CuZn $_{\rm S}$ alloy layer onto the Zn electrodes, with a low lattice mismatch of 3.6% with Zn(002) crystal plane. The alloy interlayer selectively locked the lattice orientation of Zn deposits, enabling the epitaxial growth of Zn deposits layer by layer. Sun et al. performed surface selenation on Zn foil via chemical vapor deposition (CVD). A Zn–Se alloy layer was in situ formed, creating a semicoherent interface ($\approx 13\%$) with Zn and guiding the Zn deposition along the (002) plane. Similarly, alloys like ZnTe 182 and AgZn $_3^{183}$ were also suggested to facilitate dense Zn growth due to their favored binding energy with the Zn(002) plane.

Besides alloys, metal nitrides, ¹⁸⁴, ¹⁸⁵ polymers, ^{186–188} nanofluids, ¹⁸⁹ and Prussian blue analogues ¹⁹⁰ were also explored to serve as interlayers for Zn(002) growth. To serve as an interlayer, the material should exhibit not only a matched lattice structure but also physicochemical properties like electrical conductivity, ionic conductivity, and corrosion resistance, which are crucial in stabilizing the Zn anode during the repeated electroplating/stripping process.

4.2. Zn Growth on Single-Crystalline Substrates

4.2.1. Single-Crystalline Zn Substrate. Since Zn deposition on Zn forms a fully coherent interface with zero lattice mismatch, nucleation on a single-crystalline Zn substrate requires minimal energy to overcome the barrier. Building upon this, Liang et al. demonstrated that exposing the preferred (002) crystal plane on the Zn anode surface enhances both stability and reversibility. The lateral growth of Zn helps suppress side reactions, because the (002) plane strongly retains Zn atoms and possesses a high free energy barrier for hydrogen evolution. Moreover, a regulated structure was achieved due to the homogeneous interfacial charge distribution and preferred adsorption in the parallel direction, making it an ideal surface for long-term cycling stability.

Robertson et al. further addressed the dendrite issue using single-crystalline Zn(002). Through SEM analysis, they revealed that Zn deposited on polycrystalline Zn formed

randomly oriented flaky structures that extended outward from the electrode surface (Figure 33a,b). These irregular morphol-

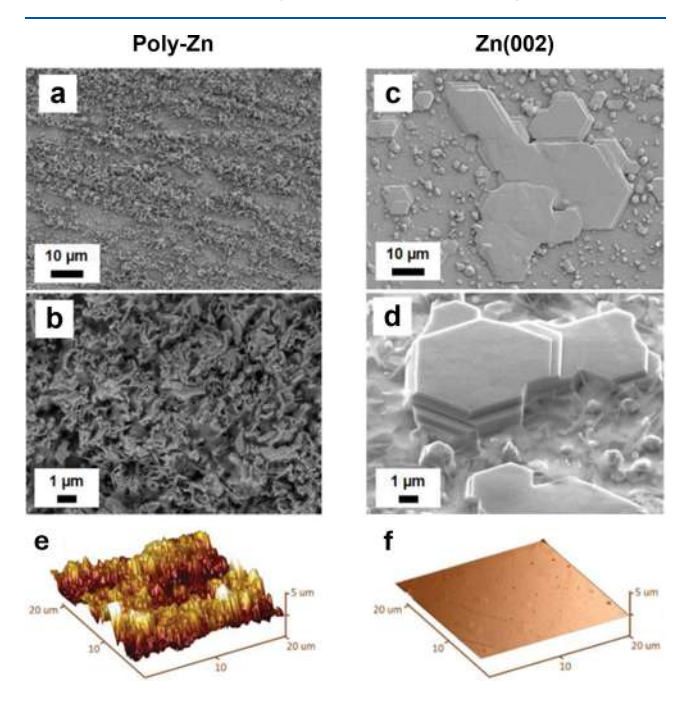


Figure 33. Comparison of polycrystalline and single-crystalline Zn(002). SEM images of Zn electroplated on (a,b) polycrystalline Zn and (c,d) single-crystalline Zn(002). AFM surface profiles of zinc plated on (e) polycrystalline Zn and (f) single-crystalline Zn. Reproduced with permission from ref 192. Copyright 2022 John Wiley and Sons.

ogies contributed to severe roughening and inhomogeneity of the electrode, which in turn promoted dendritic growth during subsequent cycling. In stark contrast, Zn plated on single-crystalline Zn electrodes formed smooth, flat hexagonal islands, all exhibiting the same rotational alignment (Figure 33c,d). This difference in morphology, confirmed by atomic force microscopy (AFM) analysis (Figure 33e,f), suggests that single-

crystalline Zn offers a more controlled and uniform deposition process, which is essential for maintaining electrode integrity over extended charge—discharge cycles.

More recently, Jiang et al. demonstrated that Zn deposition on single-crystalline Zn follows a step-edge guided homoepitaxy pattern, enabling layer-by-layer Zn plating and stripping with minimal side reactions regardless of local anisotropy. 193 Their study revealed that polycrystalline Zn tended to deposit as hexagonal platelets only when the system exceeded mass transport limitations (>100 mA cm⁻²). However, even at these ultrahigh currents, voids and dendrites persisted, leading to incomplete stripping during cycling. In contrast, Zn deposition on single-crystalline Zn exhibited a distinct morphological transition, consistently forming ordered hexagonal Zn platelets across a wide current density range from 0.1 mA cm⁻² to 100 mA cm⁻². This transition was driven by the increased adsorption energy of Zn adatoms at step edges compared to that of terraces, which made edge nucleation more energetically favorable. Consequently, subsequent crystal growth followed a highly organized pattern, allowing adjacent domains to coalesce seamlessly and form uniform Zn layers.

However, some research suggests that Zn(002) may not be the optimal choice for Zn deposition, particularly at high areal capacities. Zhang et al. found that while Zn(002) performed well at low areal capacities, its cycling stability deteriorated at higher deposition levels due to the accumulation of lattice mismatch and an increasingly uneven electric field distribution. ¹⁹⁴ These factors ultimately led to cycle failure. In contrast, their study demonstrated that the Zn(101) anode enabled continuous and stable electroepitaxy, ensuring reliable cycling performance, even under high deposition capacities (Figure 34).

It is important to clarify that the so-called "single-crystalline Zn" is not strictly single crystals. In most studies, the as-formed single-crystalline Zn exhibits single-crystalline characteristics at the particle scale; however, grain boundaries remain essential structural units connecting individual grains. These grain boundaries have a significant influence on Zn deposition behavior, as intercrystalline regions are generally more reactive than intracrystalline regions. The increased reactivity of

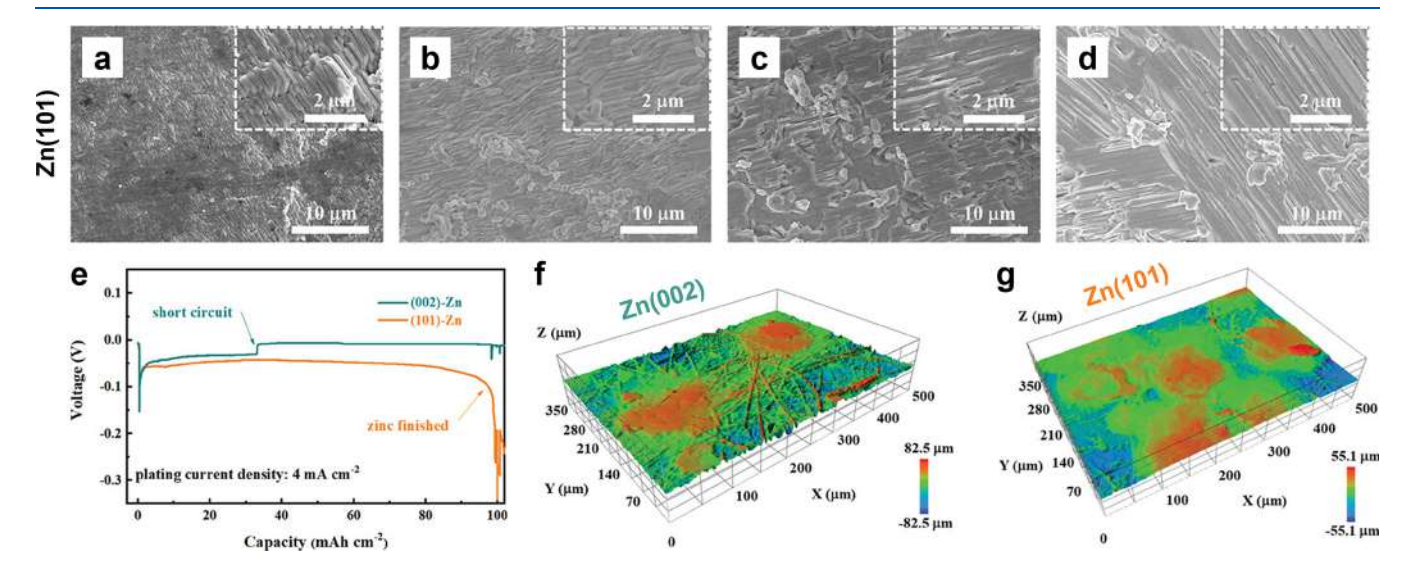


Figure 34. Zn(101) single-crystalline anode as an alternative to Zn(002). (a–d) SEM images of progressive Zn deposition on Zn(101) anode. (e) Voltage—capacity profile of Zn electrodeposition on Zn(002) and Zn(101). White light interferometer 3D height images of postcycled (f) Zn(002) and (g) Zn(101). Reproduced with permission from ref 194. Copyright 2024 John Wiley and Sons.

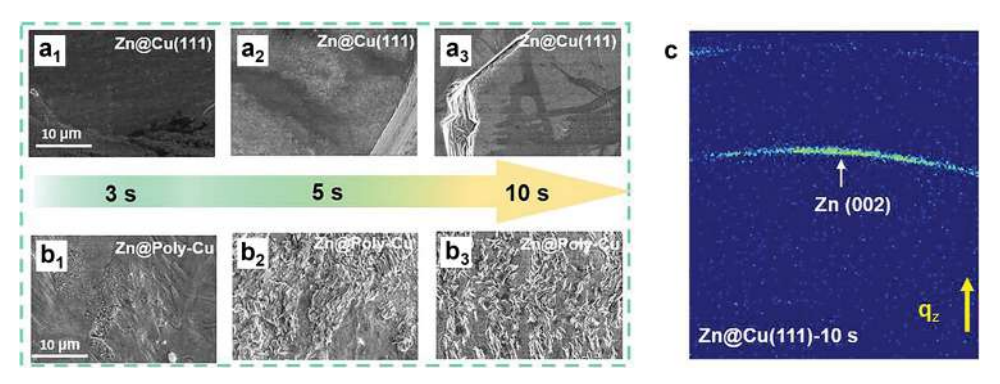


Figure 35. Comparison of polycrystalline Cu and single-crystalline Cu. SEM images of Zn electrodeposited on (a) single-crystalline Cu and (b) polycrystalline Cu. (c) Grazing incidence small-angle X-ray scattering (GIWAXS) pattern of Zn on Cu(111) after 10 s of deposition. Reproduced with permission from ref 197. Copyright 2023 John Wiley and Sons.

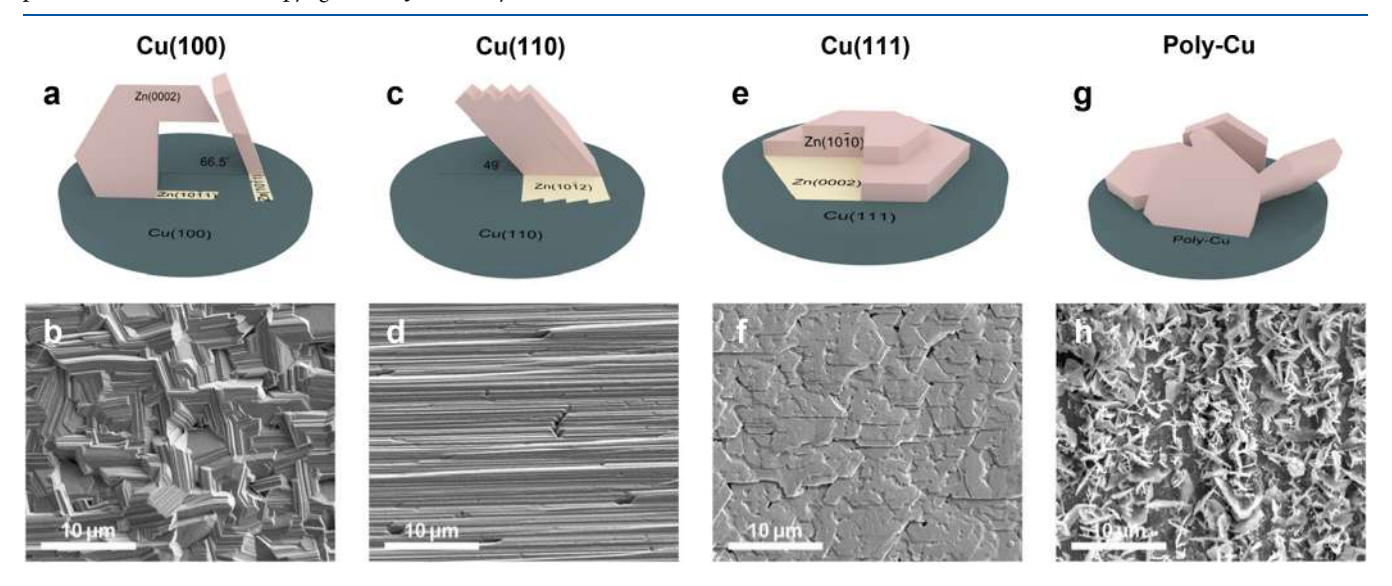


Figure 36. Distinct Zn deposition morphology on single-crystalline Cu substrates with different facets. Schematics and SEM images of electrodeposited Zn onto (a,b) Cu(100), (c,d) Cu(110), (e,f) Cu(111), and (g,h) polycrystalline Cu at 10 mA cm $^{-2}$ with 1 mAh cm $^{-2}$. Reproduced with permission from ref 30. Copyright 2025 American Chemical Society.

intercrystalline regions can lead to undesirable preferential Zn deposition and side reactions, ultimately compromising electrode performance. To address this issue, Zhao et al. proposed a grain boundary engineering strategy to modify the intercrystalline regions in (002)-textured Zn by introducing In metal as a grain boundary filler. ¹⁹⁵ The infusion of In metal into Zn grains effectively suppressed intergranular Zn issues, greatly enhancing the stability of the Zn electrodes during battery operation. Similarly, Zhou et al. tailored the grain boundaries of polycrystalline Zn using a Zn—Ti alloy, which resulted in a significantly improved full cell performance. ¹⁹⁶

4.2.2. Single-Crystalline Cu Substrate. Due to its strong affinity for Zn, Cu has been extensively studied as a substrate for Zn deposition. Among various forms of Cu, single-crystalline Cu has demonstrated superior performance over polycrystalline Cu due to its higher homogeneity and better lattice compatibility. These qualities facilitate more uniform Zn deposition, reducing the likelihood of irregular growth, mitigating side reactions, and enhancing the overall electrochemical stability.

Sun et al. investigated the Zn deposition behavior on single-crystalline Cu(111) substrates prepared with a scalable fabrication method. ¹⁹⁷ Their findings revealed that Zn deposition exhibited a strong preference for the (002) orientation in which uniform hexagonal Zn plates were formed

rapidly on Cu(111). In contrast, Zn deposition on polycrystal-line Cu tended to nucleate along grain boundaries and accumulate on surface ridges, leading to an uneven morphology and increased susceptibility to dendrite formation (Figure 35). The study suggested that Cu(111) exhibited a negligible nucleation energy barrier for Zn(002) deposition due to the low interfacial free energy associated with the coherent interface between Zn(002) and Cu(111). Liang et al. explored the potential of leveraging Cu(111) facets in nanostructured substrates, specifically Cu nanowires, to guide Zn deposition. The minimum lattice mismatch between Cu(111) and Zn(002) reinforced the advantages of using highly ordered single-crystalline substrates for achieving controlled and reversible Zn plating and stripping.

However, the debate over the optimal Cu facet for Zn deposition remains unresolved, as different studies present varying perspectives on the most favorable crystallographic orientation of the Cu substrate. Wang et al. demonstrated that single-crystalline Cu(220) effectively facilitated Zn(002) deposition, suggesting that (220)-oriented Cu provides a viable alternative for achieving stable Zn plating. Meanwhile, Zeng et al. proposed that underpotential Zn deposition occurred preferentially on Cu(100), where the as-formed metallic Zn

monolayers served as nucleation sites for subsequent Zn growth. 200

Most recently, Cui et al. conducted a comprehensive study on all three distinct single-crystalline Cu facets to systematically evaluate their influence on Zn plating behavior (Figure 36). While all single-crystalline Cu substrates demonstrated superior performance compared with polycrystalline Cu, the morphology and orientation of the deposited Zn varied depending on the crystallographic orientation of the Cu substrate. On Cu(100), hexagonal Zn flakes aligned perpendicularly, but their slanted orientation resulted in a slightly uneven surface. In contrast, Zn deposition on Cu(110) and Cu(111) produced flatter surfaces with more uniform orientation—Zn aligned parallel to Cu(111), whereas it was uniformly slanted on Cu(110). A detailed analysis of the crystallinity relationship between electrodeposited Zn and Cu revealed that Cu(111) offered the most favorable conditions for Zn diffusion and epitaxial growth.

4.3. Electrolyte Engineering

As discussed earlier, according to Young's eq (eq 7), the expression of the contact angle is given as

$$\cos \theta = \frac{\gamma_{se} - \gamma_{sn}}{\gamma_{ne}} \tag{7a}$$

For Zn-oriented deposition on textured substrates, the interfacial energy between the substrate and the metal nucleus is altered. When forming a coherent or semicoherent interface, γ_{sn} decreases, leading to a reduction in the contact angle and, consequently, a lower nucleation energy barrier. Similarly, the contact angle can be further minimized by reducing the interfacial energy between the electrolyte and the metal nucleus, which can be effectively achieved through electrolyte engineering. Electrolyte engineering further influences the Zn²+ solvation structure and electrical double layers, thereby suppressing unwanted dendrite growth and side reactions.

4.3.1. Electrolyte-Facilitated Zn(002) Growth. Zhou et al. demonstrated that Zn deposition morphology is strongly influenced by the electrolyte salt, particularly the anion.³² As shown in Figure 37, Zn metal deposited from ZnCl₂ and Zn(CH₃COO)₂ solutions exhibited irregular crystalline ori-

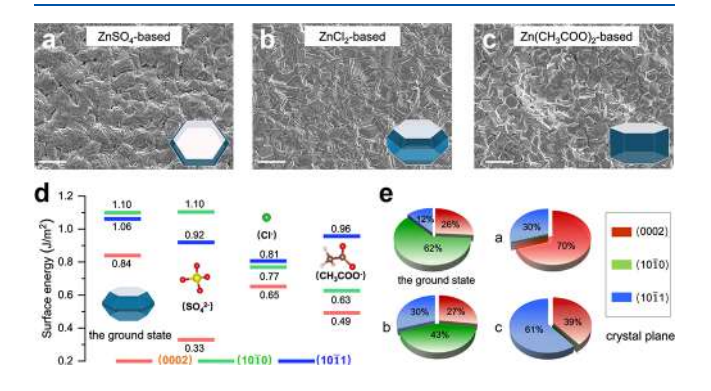
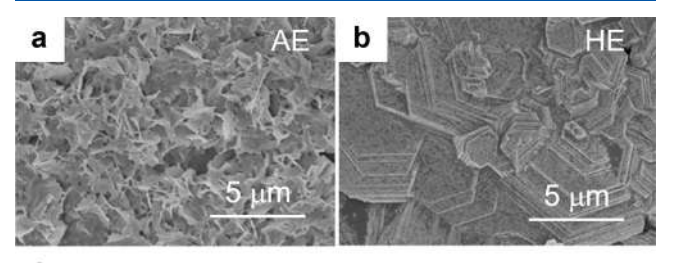


Figure 37. Effect of the electrolyte anions on Zn growth. SEM images of the electrodeposited Zn in (a) $ZnSO_4$, (b) $ZnCl_2$, and (c) $Zn(CH_3COO)_2$ systems, respectively (scale bar is $20~\mu m$). The inset images correspond to the equilibrium shape of Zn crystals in different systems, reconstructed using the Wulff construction. (d) Surface energies of Cl^- , SO_4^{2-} , and CH_3COOH^- on each main crystal plane of Zn. (e) The ratios of each crystal plane in different electrolyte systems after Zn electrodeposition. Reproduced with permission from ref 32. Copyright 2024 Springer Nature.

entations. In contrast, a single (0002)-textured Zn metal was obtained from a ZnSO₄ electrolyte. This was attributed to the selective adsorption of anions, which reduced the surface energies across all crystal planes. Notably, the surface energy of the Zn(0002) plane in the ZnSO₄ system decreased significantly, indicating a preferential exposure of this plane in the presence of SO₄²⁻ anions. According to the Gibbs–Wulff theory of crystal growth, surfaces with lower surface energy tend to grow laterally at a faster rate, making them the predominantly exposed crystal planes. The equilibrium morphologies of Zn deposits, reconstructed using Wulff construction, exhibited distinct crystal structures across the three electrolyte systems.

Xu et al. identified LaCl₃ as a crystal facet-terminating agent for Zn crystals. ²⁰⁴ Specifically, Cl⁻ anions selectively adsorbed onto the (002) facet, while La³⁺ ions, due to their lower reduction potential, accumulated near these adsorption sites. This electrostatic interaction slows the growth kinetics of the Zn(002) plane. Similarly, Zhang et al. developed an iodide ion (I⁻)-assisted electrodeposition strategy, enabling scalable fabrication of highly (002)-textured Zn.

Guo et al. investigated the impact of polar solvents such as dimethylacetamide (DMAC) and trimethyl phosphate (TMP) in hybrid electrolyte (HE) (Figure 38). 206 These solvents



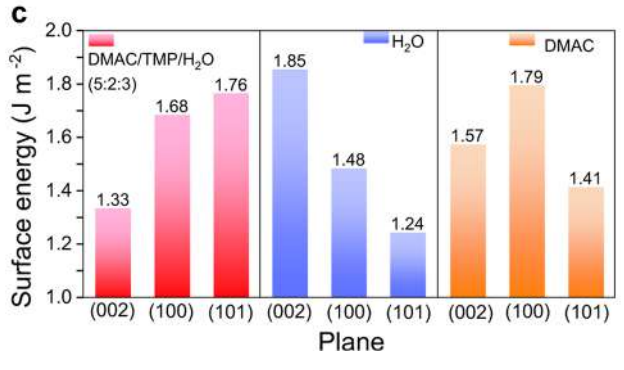


Figure 38. Effect of the electrolyte solvent composition on Zn growth. Surface morphology for deposited Zn in (a) aqueous electrolyte and (b) hybrid electrolyte. (c) Surface energy value for main planes of Zn in different liquid environments. Reproduced with permission from ref 206. Copyright 2023 Springer Nature.

interact strongly with H_2O through dipole—dipole interactions, increasing the electron density around water protons. This effect reduces the thermodynamic favorability of H_2O dissociation and strengthens the O–H bonds. In a conventional aqueous electrolyte (1 M $Zn(OTf)_2$, AE), Zn deposition resulted in a porous layer. In contrast, deposition in HE produced a compact stepped surface with a hexagonal crystalline structure. DFT calculations revealed that the (002) plane has the lowest surface energy in the DMAC/TMP/ H_2O mixture, leading to preferential Zn(002) growth. Pan et al. 207 demonstrated that selective adsorption of highly polar propylene glycol (PG) molecules at the Zn/electrolyte interface generated a uniform interfacial

electric field with enhanced potential intensity, while Huang et al. 208 employed hexamethylphosphoramide as a cosolvent in an aqueous electrolyte to restructure the $\rm Zn^{2+}$ solvation shell. Both modification strategies promoted dense and uniform Zn electroplating patterns.

Beyond modification of salts and solvents, electrolyte additives have been explored to facilitate epitaxial Zn deposition. Cui et al.²⁰⁹ discovered that introducing a trace amount of a nonionic surfactant led to the *in situ* formation of a liquid crystal interphase (Figure 39).²⁰¹ This interphase aligned both Zn and

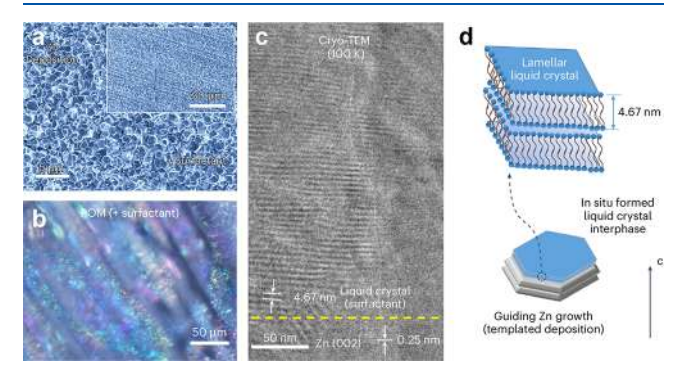


Figure 39. Influence of electrolyte additives on Zn growth. (a) SEM images of deposited Zn using a surfactant electrolyte. (b) Polarized optical microscope image of Zn surface prepared in a surfactant electrolyte. (c) Cryo-TEM image of the interface between Zn(002) and liquid crystal. (d) Schematic illustration of Zn(002) growth via templated deposition at the liquid crystal interphase. Reproduced with permission from ref 209. Copyright 2024 Springer Nature.

MnO $_2$ depositions along the c-axis, significantly improving the electrochemical cycling stability. Soft matter characterizations revealed a dynamic transition from a bilayer-aligned surfactant structure before deposition to a gradient liquid crystal interphase afterward. Likewise, various additives, including cationic/anionic surfactants $^{210-212}$ and sodium salts, $^{213-215}$ have been shown to promote growth of Zn(002) orientation. Additional studies $^{216-220}$ further validate the significance of electrolyte engineering in optimizing Zn deposition.

4.3.2. Electrolyte-Facilitated Zn(101)/(100) Growth. As discussed above, the Zn(002) crystal plane has been considered to have a better chemical corrosion resistance and inhibitory effect on dendrite growth relative to the loosely packed Zn(100) and Zn(101) facets. In addition, dendrite-free Zn deposition is more readily realized on Zn(002) because its parallel alignment with the substrate manifests a small contact angle, while the large contact angle of vertical and tilted Zn deposition on Zn(100) and Zn(101) is considered thermodynamically less stable. Due to the prominence of this prior perception, most endeavors have been devoted to developing practical texturing strategies to induce selective exposure of the Zn(002) crystal planes for enhanced electroplating/stripping stability.

However, a number of studies also demonstrated excellent Coulombic efficiency (CE) and cycling lifespan by realizing highly textured Zn(101) or Zn(100) deposition. Hu et al. used theophylline, a low-cost additive for the $ZnSO_4$ electrolyte, to regulate the growth rate of different crystal planes, thus realizing clear crystal orientation preferences on the pristine Zn foil. Specifically, the theophylline-derived cations preferentially adsorbed on the Zn(002) plane rather than the other facets due to its higher adsorption energy, which further accelerated the growth rate of the Zn(002) facet by the stronger binding

affinity with Zn^{2+} ions. This strategy effectively promoted the transformation of pristine Zn into Zn(101) plane with homogeneous surface crystal orientation. Similarly, Liu et al. demonstrated a preferential exposure of unconventional Zn(101) facet by adopting a small amount of malate molecules as an electrolyte additive. The malate molecules preferentially adsorbed on the Zn(002) and Zn(100) facets, achieving the preferred Zn(101) plane orientation exposure. Additional electrolyte additives, such as 3-(N-morpholino)-2-hydroxypropanesulfonic acid-dimethyl sulfoxide Zn(101) and dextrin, were reported to engineer and optimize Zn deposition by inducing a Zn(101) deposition.

To achieve Zn(100) deposition, Liu et al. introduced disodium lauryl phosphate surfactant into the ZnSO₄ electrolyte as a depositing agent to realize vertically oriented Zn plating and achieve a dendrite-free feature with rapid Zn electro-plating/ stripping, high capacity, and long cycle life. 225 Phosphoric acid groups in surfactants selectively adsorbed on the Zn(002) crystal surface, thus shielding the (002) plane to promote vertical Zn plating toward the Zn(100) crystal plane. Benefiting from such oriented Zn plating, a dense and stable (100)-textured Zn layer was formed due to the rapid growth of Zn atoms along the (100) plane and the slow in-plane deposition on the (002) plane. Wang et al. proposed the use of a zwitterionic amino acid ion, aspartic acid, to achieve the in situ fabrication of a highly ordered Zn(100) anode.²²⁶ The orderly arranged structure on the surface of the anode induced uniform and dense deposition of Zn2+ in the vertical direction and eliminated the growth of dendrites, leading to good reversibility and stability of the battery.

4.4. Effect of Operation Conditions

In addition to substrate modifications and electrolyte engineering, extensive research has been dedicated to understanding the relationship between the operation conditions (e.g., current density, loading, pressure, and temperature) and Zn deposition behaviors. Many studies have provided thermodynamic and kinetic insights into the Zn nucleation and growth of aqueous battery systems.

Among these factors, the current density is the most widely studied, as it directly influences the overpotential, which serves as the driving force for Zn deposition. It is well-established that Zn tends to deposit on the (002) crystal plane when cells operate at high current densities. Zhang et al. proposed that at a relatively low current density (20 mA cm⁻²), Zn deposition occurred with a balanced growth rate on the (002) and (100) planes, leading to an overall (101)-textured surface, given the hexagonal closepacked structure of Zn.²²⁷ However, at a higher electrodeposition current (80 mA cm⁻²), the increased energy supply raised the Zn plating overpotential. In this case, the growth rate disparity between the (100) and (002) planes became significantly larger, with the (100) plane growing much faster due to its more favored adsorption. Consequently, high-current electrodeposition resulted in an oriented Zn(002) structure.

Further research has explored a broader range of current densities to determine the dominant Zn deposition behaviors. Sun et al., through a combination of *in situ* optical imaging and theoretical modeling, identified that Zn deposition modes varied based on the interplay between crystallographic thermodynamics, kinetics, and Zn²⁺ ion diffusion. These factors dictated the formation of different morphologies: stacked hexagonal plates, horizontally dense granules, or vertically oriented metal pillars. Pu et al. introduced a unified parameter,

relative current density (RCD = i/i_L), to classify deposition behaviors. Here, i_L represents the limiting current density, which was experimentally determined via linear sweep voltammetry (LSV). As illustrated in Figure 40, three regimes

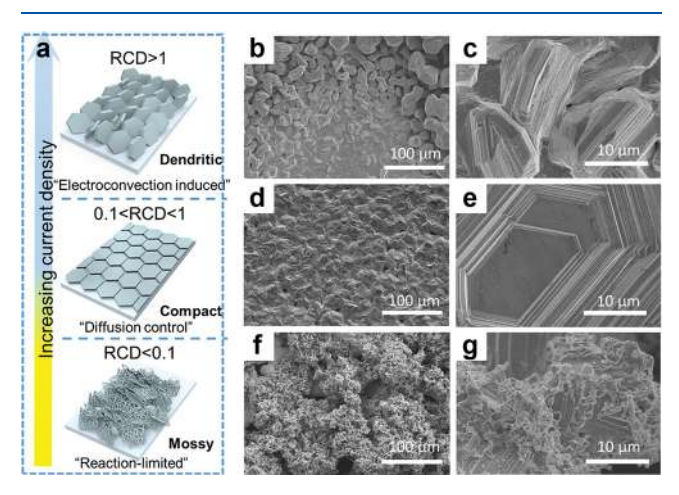


Figure 40. (a) Schematic illustrating the dependence of morphology on the relative current density (RCD). The SEM images of the Zn electrodeposits at different current density regimes: (b,c) RCD > 1, (d,e) 1 > RCD > 0.1, and (f,g) RCD < 0.1. Reproduced with permission from ref 229. Copyright 2023 John Wiley and Sons.

were identified: vertical dendritic structures for RCD > 1, compact and strongly (002)-textured structures for 0.1 < RCD < 1, and mossy structures for RCD < 0.1. Similar results were reported by Archer's group.²³⁰

Despite the dense and highly textured Zn deposition achieved at high current densities, such conditions are generally considered to be unfavorable for long-term stability. Zhou et al. found that the combination of localized high current density and rapid Zn²⁺ depletion led to severe separator permeation, eventually causing short circuits when separators were used.²³¹ This effect counteracted the benefits of oriented Zn deposition observed in separator-free setups under the same high current densities. Furthermore, operating full cells at such high currents remains impractical, primarily due to the lack of cathode

materials with sufficient rate performance to match these conditions. 232,233

Beyond current density, Chen et al. discovered that the deposition amount of Zn also affected its growth pattern.²³⁴ As the deposition capacity increased from 10 mAh cm⁻² to 25 mAh cm⁻², Zn deposition became more disordered, transitioning from (002)-preferred growth to a (101) crystal plane orientation. Additionally, Robertson et al. demonstrated that applying external pressure during electroplating enhanced the durability and cycling stability of Zn anodes, especially at a low current density range from 1 mA cm⁻² to 10 mA cm^{-2,235} The deposited Zn exhibited a mossy-like morphology but underwent a transition to a denser morphology with fewer voids under external pressure (Figure 41). The pressure-induced morphological changes created a more mechanically stable microstructure, which helped prevent metal detachment during stripping, thereby reducing degradation from dead Zn formation and corrosion losses.

In summary, crystallographic engineering of the Zn anode has emerged as one of the most effective strategies to overcome key challenges, including poor electrodeposition/stripping behavior and side reactions such as electrochemical HER and corrosion-induced HER. Over the past decade, numerous efforts and impressive advances have not only improved the performance of Zn-based chemistries but also established the fundamental basis for crystallographic engineering. Looking ahead, research is expected to move beyond laboratory-scale concept verification toward demonstrating the effectiveness of single-crystalline metal anodes and substrates in pouch or cylindrical cells with nominal capacities under practical conditions such as low negative-to-positive (N/P) capacity ratios and lean-electrolyte designs.

5. OTHER METAL ANODES

A high volumetric energy density is more desirable for mobile devices (such as vehicles, assistive robots, and drones) than for stationary energy storage systems. The more portable the device (such as personal electronics), the less space available for its battery; therefore, the volumetric energy density plays a crucial role. Besides Li and Zn, metal batteries such as Na, Al, and Mg have gradually become emerging research areas. In this section,

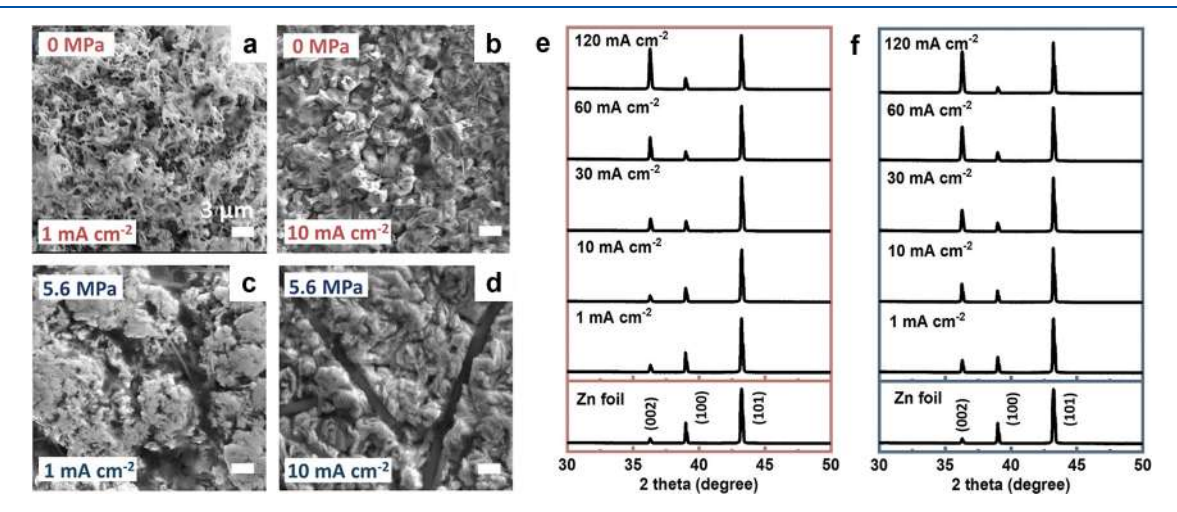


Figure 41. Impact of applied pressure on Zn electrodeposition. SEM images of Zn deposited on Zn foil (a,b) with and (c,d) without external pressure at different plating current densities. XRD of Zn electrodeposition of varying current densities (e) without and (f) with an applied pressure of 5.6 MPa. Reproduced with permission from ref 235. Copyright 2024 John Wiley and Sons.

we discuss strategies involving crystallographic optimization of the metal deposits or substrates for Na, Al, and Mg metal anodes.

5.1. Na Metal Anode

Na metal batteries present a promising, sustainable, and cost-effective alternative to LMBs, primarily due to their high natural abundance and theoretical gravimetric and volumetric capacities (1165 mAh g⁻¹ and 2026 mAh cm⁻³, respectively). Similar to Li, Na possesses a BCC structure and faces challenges related to dendrite formation, prompting extensive research efforts to control its deposition morphology. Unlike Li batteries, which typically use Cu as the anode current collector, Al is a more suitable choice for both the positive and negative electrodes in Na batteries. This is due to its affordability, lightweight, and resistance to alloying reactions with Na. 238

However, when Na is deposited on a conventional polycrystalline Al foil, it tends to accumulate randomly, leading to dendritic growth and ultimately degrading battery performance. To address this issue, Pint et al. applied carbon films onto Al foil using a simple aqueous slurry casting process. ²³⁹ Acting as a nucleation layer, the carbon material facilitated uniform sodium deposition, forming hexagonal island-like structures. Over time, these sodium islands grew and coalesced, while maintaining distinct grain boundaries (Figure 42a-c).

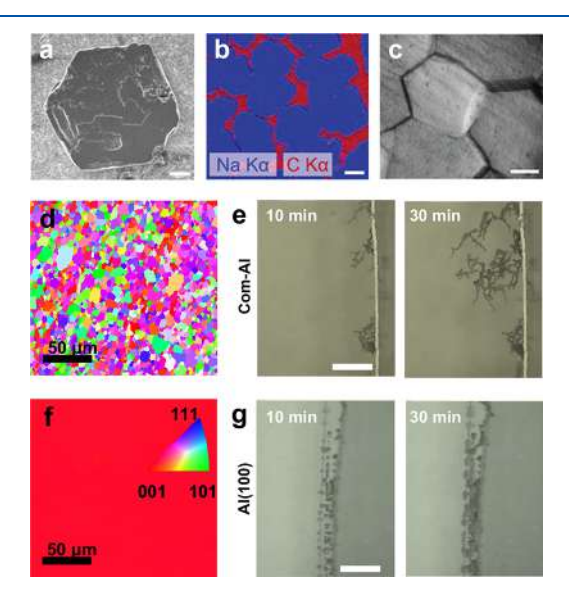


Figure 42. Single-crystalline materials for Na metal anodes. (a) SEM image and (b) EDS element mapping of sodium metal islands. (c) Micrograph of plated sodium metal film. Reproduced with permission from ref 239. Copyright 2017 American Chemical Society. IPF and *in situ* optical micrographs of Na deposition on (d,e) commercial Al and (f,g) single-crystalline Al(100). Reproduced with permission from ref 241. Copyright 2025 Springer Nature.

Beyond surface treatment of the Al foil, the use of single-crystalline Al substrates has also been explored. Matsumoto et al. developed a fluorinated Al substrate with a strong (100) crystal plane orientation, which enhanced sodium nucleation and growth while promoting the formation of a stable SEI rich in inorganic components. Similarly, Yu et al. demonstrated that single-crystalline Al(100) induced uniform Na deposition and improved Na transport kinetics, which was attributed to the reduced grain boundaries of crystallographic-oriented substrates. As a result, highly reversible Na electrochemical stripping/plating behavior was achieved, leading to an anode-

free full cell with superior rate performance and cycling stability (Figure 42d-g).

5.2. Al Metal Anode

Al metal batteries are regarded as viable alternatives to LIBs owing to the low cost, intrinsic nonflammability, and crustal abundance of Al. More importantly, owing to its three-electron redox property, Al manifests high theoretical gravimetric and volumetric specific capacities (2980 mAh g⁻¹ and 8040 mAh cm⁻³, respectively). Therefore, rechargeable Al-based batteries could enable substantial advances in energy storage technology.

Similar to other metal batteries, the plating and stripping of Al are influenced by the atomic structure of the anode surface. Liu et al. demonstrated the correlation between the preferred crystal plane growth mechanism with high lattice matching and the electrochemical performance of Al anodes by modulating the preferred orientation of the Al crystal plane. In this work, Al(111), Al(200), Al(220), and Al(311) were systematically studied (Figure 43a). The *in situ* optical observation results

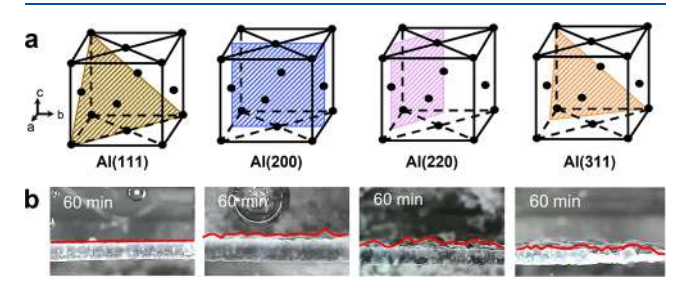


Figure 43. Single-crystalline materials for Al metal anodes. (a) Surface atomic arrangements of Al(111), Al(200), Al(220), and Al(311). (b) *In situ* optical observation of the plating process in different aluminum anodes. Reproduced with permission from ref 245. Copyright 2024 Springer Nature.

showed a uniform and dense deposition morphology for the Al(111) electrode and uneven deposition morphology for Al(200), Al(220), and Al(311) electrodes after 60 min of deposition (Figure 43b). This distinct deposition morphology was attributed to the strongest adsorption of Al on (111) crystal plane, which facilitated an isomorphic crystal plane growth mode.

Al, with an FCC crystal structure, shares many similarities with other FCC metals. For example, Au and Al are in the same space group of $Fm\overline{3}m$, and the lattice mismatch between Au and Al is only 0.7%, indicating that Au is a potential substrate to epitaxially regulate the growth of Al. Archer et al. designed Au nanosheets with a strong crystal orientation associated with (111) crystal plane. The typical morphology of Al deposited on stainless steel was seen to be an ensemble of randomly distributed large particle clusters that formed a heterogeneous landscape on the substrate. In contrast, Al electrodeposits on Au sheets formed uniform and dense nuclei with an average particle size of approximately 200 nm. Similarly, Chen et al. constructed a lattice-matching layer on Ti substrate by magnetron sputtering of Au, leading to a uniform and dense Al reservoir and greatly improving cycle life and CE of the Au@Ti electrode. 247

5.3. Mg Metal Anode

Mg is an alkaline earth metal that has nearly double the volumetric capacity (3832 mAh cm^{-3}) of Li with a very negative reduction potential of -2.37 V vs standard hydrogen electrode. Similar to Al, Mg exhibits low flammability, thus air exposure is

much less of a safety and processing issue. Additionally, Mg is abundant in the earth's crust, resulting in wider availability and much lower cost. 243

Previous studies have demonstrated that Mg deposition-dissolution processes are highly reversible and Mg metal anodes do not appear to be plagued by dendrite formation to the same degree as Li. As early as 2010, Matsui investigated the electrodeposition process of Mg, where two distinct growth modes were identified. The Mg deposit obtained at low current density showed the (001) preferred orientation formed by minimizing surface energy during a slow deposition process. In contrast, the Mg deposit obtained at high current density showed (100) preferred orientation formed by maximizing the crystal growth speed for a high deposition rate. In addition, it was found that the overpotential of Mg deposition had a significantly high dependency on the activity of electrochemically active species (Figure 44). Accordingly, it was proposed

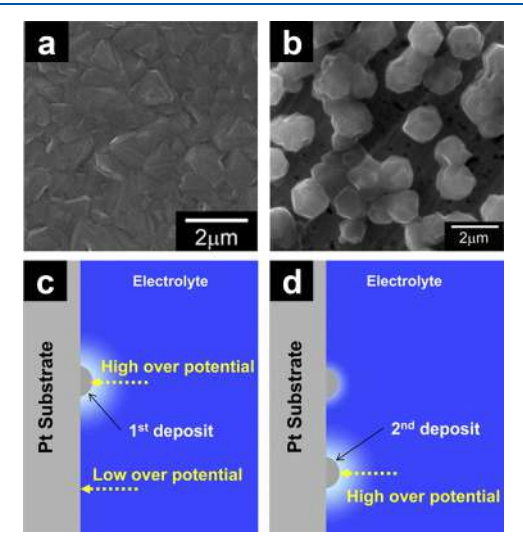


Figure 44. Observance of Mg single-crystalline seeds. SEM images of electrodeposited Mg at (a) $2.0~\text{mA}~\text{cm}^{-2}$ and (b) $0.5~\text{mA}~\text{cm}^{-2}$. Schematic showing the Mg deposition process of (c) first deposition and (d) following deposition (color of the electrolyte represents the concentration). Reproduced with permission from ref 248. Copyright 2011 Elsevier.

that the overpotential of the Mg deposition process suppressed a locally focused current, which initiated the growth of the deposits with dendritic morphology.

More recently, inspired by the epitaxial deposition of Zn, ¹⁶⁸ research has been conducted on controlling the crystallography of Mg electrodeposits to improve the electrodeposition/stripping efficiency. Cui et al. realized epitaxial electrocrystallization of Mg on nickel hydroxide@carbon cloth owing to a low lattice mismatch of 2.8% between Mg and the substrate. ²⁴⁹ In addition, the nickel hydroxide nanosheet presented an evenly distributed, hillock-like electrostatic potential field over its exposed facets, where bivalent Mg species could be captured and confined in the local electron-enriched sites near the anions, inducing uniform Mg nucleation at the atomic level. Similarly, Seh et al. employed a MXene film with a low lattice mismatch of 4% to guide the horizontal electrodeposition of Mg. ²⁵⁰

Electrolyte engineering is also crucial in improving the electrochemical performance of the Mg-based batteries. As alkaline earth metals, Mg tends to form analogous passivation

films that impede reversible plating/stripping due to the sluggish diffusion kinetics of cations. Therefore, with careful modification of the electrolyte system, surface passivation and uniform Mg deposition could be achieved simultaneously. Nazar et al. designed a dynamically clean interface on deposited Mg by introducing a stably coordinated anion and solvent, unlocking rapid nucleation/growth along the edges of Mg(0001) with minimal electrolyte decomposition (Figure 45). ²⁵¹ As a result,

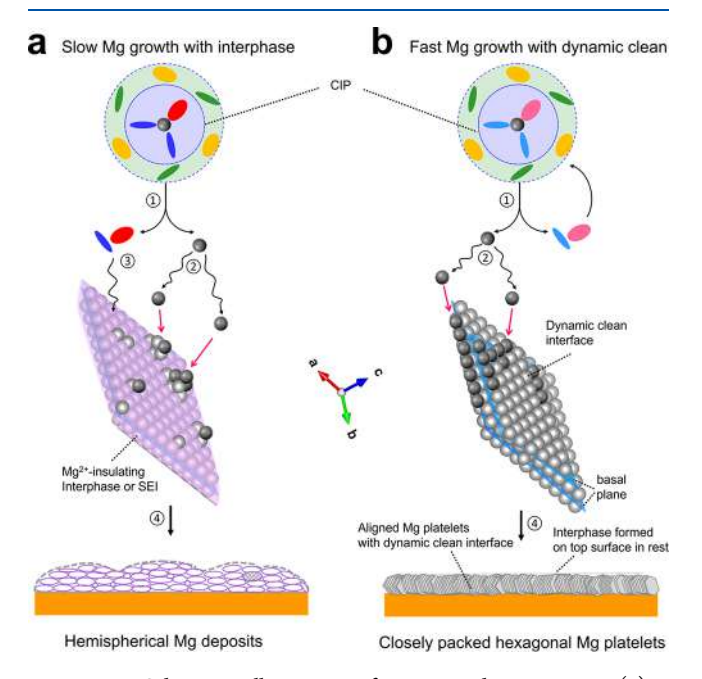


Figure 45. Schematic illustration of Mg growth pattern on (a) a sluggish interphase and (b) a dynamic clean interface at high deposition rates. Reproduced with permission from ref 251. Copyright 2025 Elsevier.

densely aligned, thin hexagonal Mg platelets were observed under practical conditions. This led to a close-to-unity CE of Mg electrodeposition/stripping under demanding conditions over long-term cycling in both half cells and full cells. Seh et al. introduced a covalent molecule of 1-chloropropane in magnesium trifluoromethanesulfonate-based electrolytes. A robust Cl-rich SEI was formed *in situ* on the Mg electrode surface, effectively minimizing sustained electrolyte decomposition and facilitating electrochemical reaction kinetics. In addition, the surface energy of the Mg(002) crystal plane was reduced from the interactions between 1-chloropropane and Mg electrode, promoting the growth of horizontally arranged platelets with enhanced (002) orientations during the electrodeposition process.

Overall, crystallographic engineering is emerging as a promising strategy to regulate metal electrodeposition beyond the Li and Zn systems. However, due to the distinct physicochemical properties of each metal—such as lattice characteristics and electrodeposition kinetics—insights from existing strategies cannot be directly transferred. Therefore, greater research attention is required to address the unique challenges of alternative systems such as Na, Al, and Mg, along with emerging candidates, including Sn and iron (Fe). In particular, systematic investigations into their crystallographygoverned nucleation behavior, interfacial chemistry, and electrolyte compatibility will be crucial for devising tailored approaches that unlock their practical potential.

6. SINGLE-CRYSTALLINE HOST MATERIALS

Unlike those in metal batteries, where a metal electrodeposition process occurs at the anode side during charging, the host anode materials of ion batteries undergo either ion insertion or alloying reactions, which present different crystallographic constraints. Ion insertion depends on well-defined diffusion pathways within the host lattice, while alloying involves substantial lattice rearrangements and large volume changes. In both cases, crystallographic orientation governs ion transport kinetics, phase transition mechanisms, and anisotropic mechanical responses, making crystallographic engineering essential for improving the rate capability, structural stability, and long-term cycling performance. In this section, we discuss crystal-plane-related physicochemical properties, challenges, and design strategies of silicon, graphite, and transition metal oxides, which are the commonly used anode materials for LIBs.

6.1. Si

6.1.1. Single-Crystalline Si. Si has been intensively explored due to its exceptionally high theoretical capacity (3579 mAh $\rm g^{-1}$), roughly ten times higher than that of the graphite anode. It is well-known that Si undergoes large volume expansion (300–400%) during lithiation, which induces cracks and contact losses, leading to rapid capacity decay and cell failure. Therefore, understanding chemo-mechanical properties of Si from a crystallographic level is crucial to enable a stable and high-performance Si anode.

Cui et al. reported a systematic study on anisotropic lithiation and volume expansion of single-crystalline Si nanowires with $\langle 100 \rangle$, $\langle 110 \rangle$, and $\langle 111 \rangle$ axial directions. After lithiation, $\langle 100 \rangle$, $\langle 110 \rangle$, and $\langle 111 \rangle$ Si nanowires showed expansion into cross, ellipse, and hexagonal shapes, respectively (Figure 46a,b).

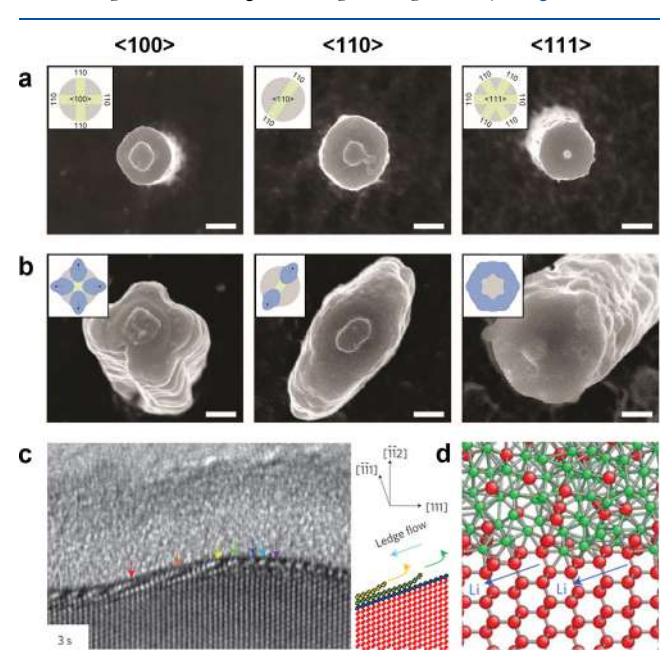


Figure 46. Anisotropic Li insertion and volume expansion of single-crystalline Si. (a) Pristine and (b) after lithiation SEM images of Si nanowires with $\langle 100 \rangle$, $\langle 110 \rangle$, and $\langle 111 \rangle$ axial directions. Reproduced with permission from ref 253. Copyright 2011 American Chemical Society. (c) TEM image of amorphous—crystalline interface showing the ledge mechanism of lithiation. (d) Relaxed atomic structures during lithiation process. Reproduced with permission from ref 256. Copyright 2012 Springer Nature.

It was found that the volume expansion is highly relevant to the (110) planes of Si nanowires, where Li is inserted preferentially on the (110) planes, leading to unique expansion shapes for nanowires with different axial directions. The preferential lithiation on the (110) plane was explained by its large interstitial space of (110), which allows for ion diffusion channels. Yan et al. showed from MD simulations that the atomic channels of Si(110) favor more lithiation than the (100) plane, enabling faster phase boundary movement. ²⁵⁴ Zhang et al. also employed finite element nonlinear diffusion model to confirm the unique expansion shape of single-crystalline Si nanowires. ²⁵⁵

Huang et al. elucidated the electrochemical lithiation dynamic of Si nanowires by *in situ* TEM with atomic-scale resolution. ²⁵⁶ Upon lithiation, a sharply defined interface (\sim 1 nm thick) separating the crystalline silicon (c-Si) core from amorphous lithium—silicon (a-Li_xSi) was observed. Although (110) and (112) planes were dominantly exposed on the nanowire surface, the lithiation kinetics were determined by the lateral migration of atomic-scale ledges along the (111) planes rather than perpendicular to (110) or (112) planes (Figure 46c,d). Specifically, the lateral motion speed of these ledges on (111) facets was measured at about 2.5 atomic planes per second, 3.5 times faster than that of (112). These differences reflect orientation-dependent interfacial mobilities, explaining the anisotropic volume expansion of single-crystalline Si during lithiation.

By utilizing the anisotropic nature of volume expansion, Nuzzo et al. demonstrated different electrochemical behaviors of 3D patterned single-crystalline Si microstructures. Specifically, the rate capability of Si microstructures increased with a larger spacing distance, and capacity utilization increased with thinner platelets. It was found that controlling the area available for volume expansion during lithiation is the key to achieving a good rate capability and capacity utilization of such single-crystalline Si microstructures.

6.1.2. Crystal Plane-Dependent Structure Degradation. The large volume change during lithiation-delithiation induces structure degradation such as cracks and pulverization. As volume expansion is highly crystal orientation-dependent, understanding such anisotropic structure degradation is necessary. Cui et al. showed that single-crystalline Si nanowires exhibited distinct fracture behaviors after lithiation. While Si nanowires with different axial directions showed the distinct expansion shapes from their previous work, they showed distinct fracture shapes under a fast lithiation rate. It was shown that orientations with less volume expansion are susceptible to fractures. As a result, $\langle 100 \rangle$ showed fractures on every angular orientation of 90°, $\langle 110 \rangle$ on 180°, and $\langle 111 \rangle$ on 60° (Figure 47a).

However, in a practical condition, each Si particle is likely to be surrounded in a confined, closed space surrounded by other Si particles. Cui et al. further investigated volume expansion of $\langle 110 \rangle$ Si nanopillar in a systematically designed unclamped and clamped systems. It was shown that Si nanopillar expanded to the $\langle 100 \rangle$ direction under a compressed scenario, despite its favorable expansion toward the $\langle 110 \rangle$ direction (Figure 47b). The compression applied on Si also resulted in different fracture dynamics, in which the unclamped case showed favored fracture sites on the $\langle 100 \rangle$ direction whereas the clamped case showed along a diagonal between the $\langle 110 \rangle$ and $\langle 100 \rangle$ directions (Figure 47c).

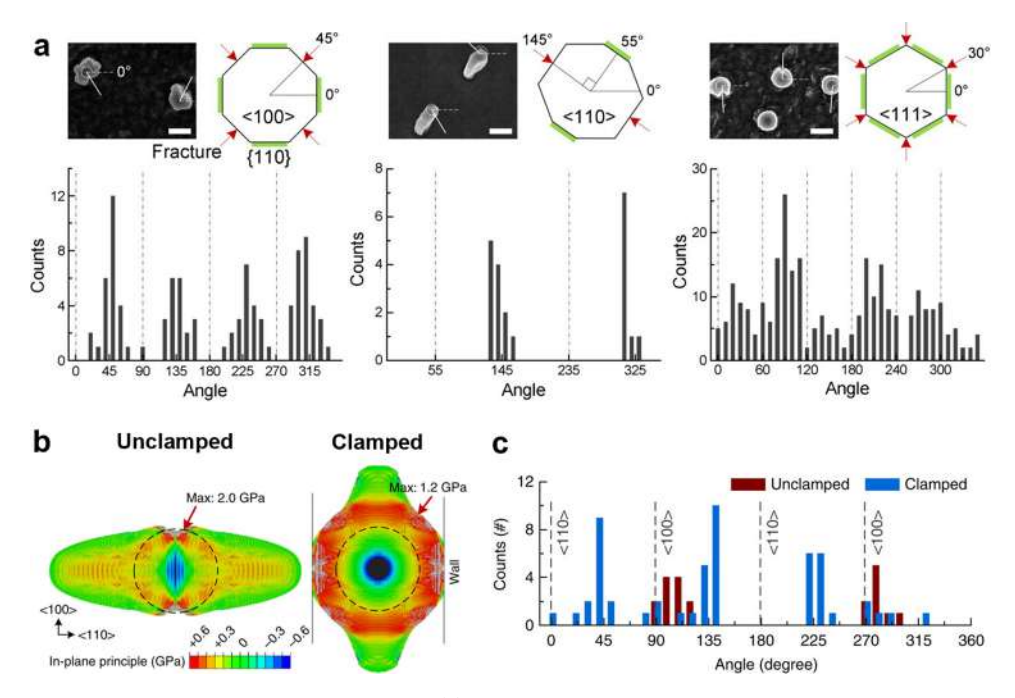


Figure 47. Anisotropic fracture dynamics of single-crystalline Si. (a) SEM images and fracture distribution of Si nanowires with $\langle 100 \rangle$, $\langle 110 \rangle$, and $\langle 111 \rangle$ axial directions. Reproduced with permission from ref 258. Copyright 2012 National Academy of Sciences. (b) FEM of in-plane principal stress of unclamped and clamped $\langle 110 \rangle$ Si nanopillars. (c) Fracture distribution of unclamped and clamped Si nanopillars. Reproduced with permission from ref 259. Copyright 2015 Springer Nature.

Häusler et al. reported structure degradation dynamics of Si using scanning transmission electron microscopy (STEM). ²⁶⁰ It was observed that after several cycles, a number of dislocations were formed at the c-Si interface (Figure 48a). These dislocations were predominantly slipping along (111) planes, comprising screw and edge type dislocations (Figure 48b). The elastic strain maps of multiaxial (ε_{xx} and ε_{yy}) and rotation (Θ) strains were quantified by employing four-dimensional STEM (4D-STEM). Strong stain variations were observed at the interface of the c-Si domain, and high strains were observed near dislocation domains (Figure 48c). MD simulation results further substantiated that the internal stresses were the driving force for shear band formation.

Komvopoulos et al. further investigated the fracture mechanism of patterned Si microstructures. 261 It was found that anisotropic volume change resulted in crack initiation perpendicular to the electrode surface, leading to propagation and deflection parallel to the electrode surface (Figure 48d). From the finite element method (FEM), the low fracture energy of the amorphous Si (a-Si)/c-Si interface was found to be responsible for the crack deflection, which led to delamination and contact loss of Si after prolonged cycling. Electrolyte additives such as vinylene carbonate (VC) or fluoroethylene carbonate (FEC) were shown to be effective on mechanical degradation of Si microstructures, in which poly-VC aggregates filled the cracks and promoted crack-free bridging and ROCO₂Li salt filled the surface cracks and decelerated the crack growth.

6.1.3. Limitations and Prospects. Despite the innovative design strategies of Si nanostructures, ^{13,262–264} understanding of failure mechanism has been limited. Wang et al. elucidated capacity fading mechanism of single-crystalline Si nanowires by cryo-STEM-HAADF and EDS mapping. ²⁶⁵ The morphology and SEI distribution of Si and SEI components were probed at different cycling numbers (Figure 49a). It was shown that with

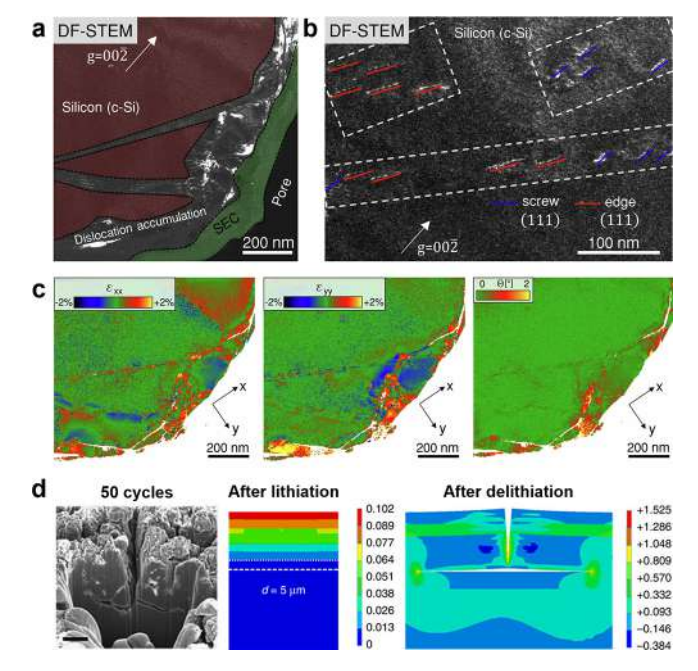


Figure 48. Structure degradation of crystalline Si. (a) Dark-field STEM image after 3 cycles showing regions of c-Si and dislocation. (b) Magnified image showing screw and edge dislocations along (111) orientation. (c) 4D-STEM elastic strain maps with $ε_{xxy}$ $ε_{yyy}$ and Θ. Reproduced with permission from ref 260. Copyright 2024 Springer Nature. (d) Cross-sectional SEM image of single-crystalline Si wafer after 50 cycles and corresponding FEM after lithiation and delithiation. Reproduced with permission from ref 261. Copyright 2016 Springer Nature.

increasing cycle number, not only did Si nanowire become more porous, but also SEI penetrated from outer shell to core of the nanowire. 3D tomography was further utilized to confirm the

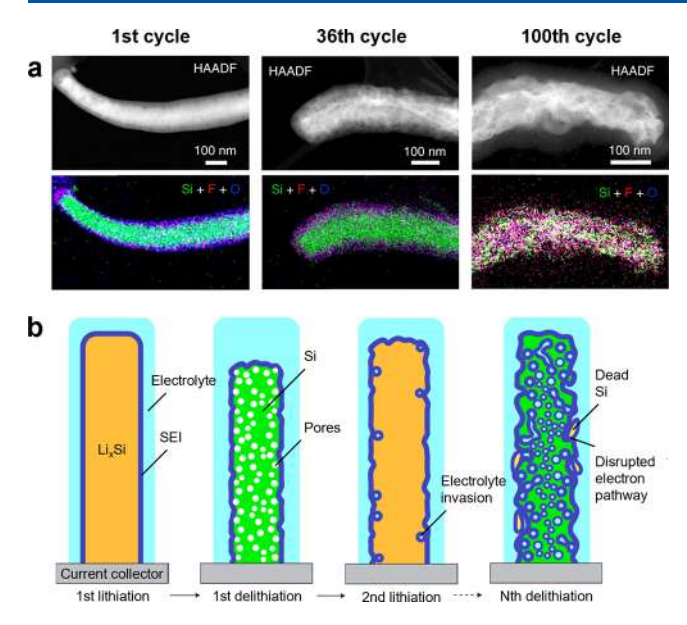


Figure 49. Vacancy generation and SEI formation of a single-crystalline Si nanowire. (a) Cryo-STEM-HAADF image and corresponding EDS mapping of Si nanowire after the 1st, 36th, and 100th cycles. (b) Schematic showing failure mechanism of Si nanowire during extended cycling. Reproduced with permission from ref 265. Copyright 2021 Springer Nature.

complete formation of thr SEI inside the nanowire. Accordingly, the capacity fading mechanism of nanosized Si was proposed in a liquid electrolyte system (Figure 49b). The first lithiation leads to volume expansion of Li_xSi with the formation of the SEI on the outer surface, and delithiation leads to shrinkage of Si where pores are nucleated. During the second lithiation, if liquid electrolyte has penetrated the pores, the SEI will form on the surface of each pore. This vacancy generation and SEI formation process is repeated during repeated cycling, resulting in excess SEI formation into the Si core as well as dead Si with contact loss.

The state-of-the-art single-crystalline Si nanostructures still cannot avoid interface and interphase challenges. Although they can be mitigated by novel strategies including encapsulation, ^{266–268} carbon composite, ^{269,270} advanced binder, ^{271,272} and electrode design ^{273–275} to keep electron and ionic contacts during prolonged cycling, the nature of SEI formation will persist as long as liquid electrolyte is in contact with Si. Electrolyte engineering strategies were found to be effective by tuning the SEI composition from fragile organic-rich to robust inorganic-rich, enabling stable cycling even with large-sized micron Si particles. ^{276–278} However, in general, enabling Si anode in practical LIBs still requires many hurdles such as swelling, cutoff voltage, calendar life, safety, and cost issues.²⁷⁹ More recent works have demonstrated stable cycling performance of the Si anode in a system where interphase can precisely be controlled. The solid electrolyte, unlike liquid electrolyte, does not flow and penetrate pores of Si; thus, the interphase formation is maintained to the initial contact between the SSE and the Si anode. Meng et al. demonstrated excellent cycle life using 99.9% Si without SSE in the electrode, which naturally confines the SEI formation into 2D interface. Based on this design concept, different strategies such as Li-Si,²⁸¹ hard carbon Li-Si,²⁸² and Ag@binder Si²⁸³ demonstrated improved cycling performance and stability of the Si-based anode in SSBs. However, the core limitation of Si anode in SSB for practical

application is low stack pressure performance, which requires a wide range of strategies including fundamental understanding, 284 electrode design 285 as well as module component engineering. 286

6.2. Graphite

6.2.1. Crystal Structure of Graphite. Graphite has dominated the anode market in LIBs over the past decades due to its low cost and exceptional stability. Its crystal structure consists of a highly ordered, layered arrangement, where two-dimensional carbon layers, known as graphene, form a honeycomb lattice. Within these layers, carbon atoms establish strong covalent bonds through sp² hybridization, while van der Waals forces hold the graphene sheets together, maintaining the overall structure. ^{287,288} The stacking of graphene layers in graphite typically follows either a hexagonal (ABA) sequence or a rhombohedral (ABC) sequence, with the former being thermodynamically more stable.

On a macroscopic scale, graphite particles exhibit two distinct surface morphologies: basal planes (parallel to the graphene layers) and edge planes (perpendicular to the layers). Due to its two-dimensional layered structure, graphite displays significant anisotropy, resulting in distinct physicochemical properties for these two planes (Figure 50a). The basal plane,

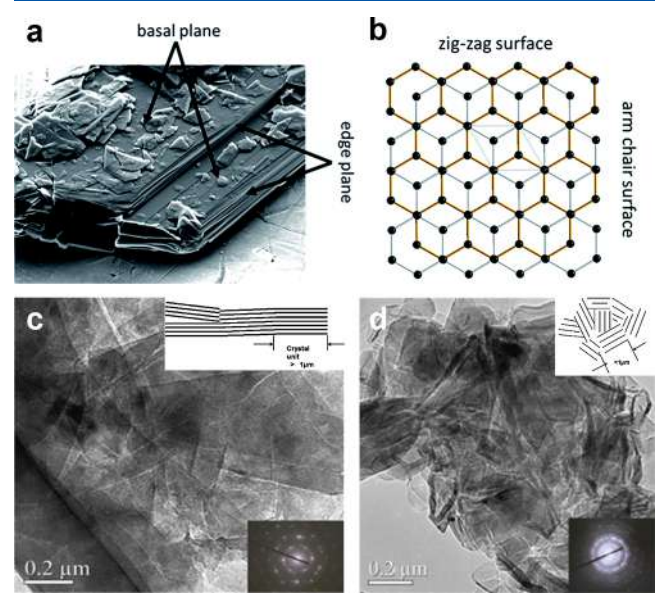


Figure 50. Crystallographic structure of graphite. (a) SEM image of a graphite particle and (b) schematic illustration of the layered graphite structure. Reproduced with permission from ref 290. Copyright 2020 Royal Society of Chemistry. TEM image and electron diffraction pattern of (c) flake graphite and (d) microcrystalline graphite. Reproduced with permission from ref 299. Copyright 2008 Elsevier.

dominated by strong covalent bonding, is largely chemically and electrochemically inert. In contrast, the weaker van der Waals interactions between layers enable guest species such as Li ions to intercalate between them. Edge planes can be further classified into zigzag (100) and armchair (110) orientations (Figure 50b).²⁹¹ The armchair edges, where adjacent carbon atoms share triple covalent bonds, offer greater chemical stability and are more favorable for Li intercalation than zigzag edges. This leads to improved Li transport kinetics and reduced parasitic reactions at armchair sites.^{292–295}

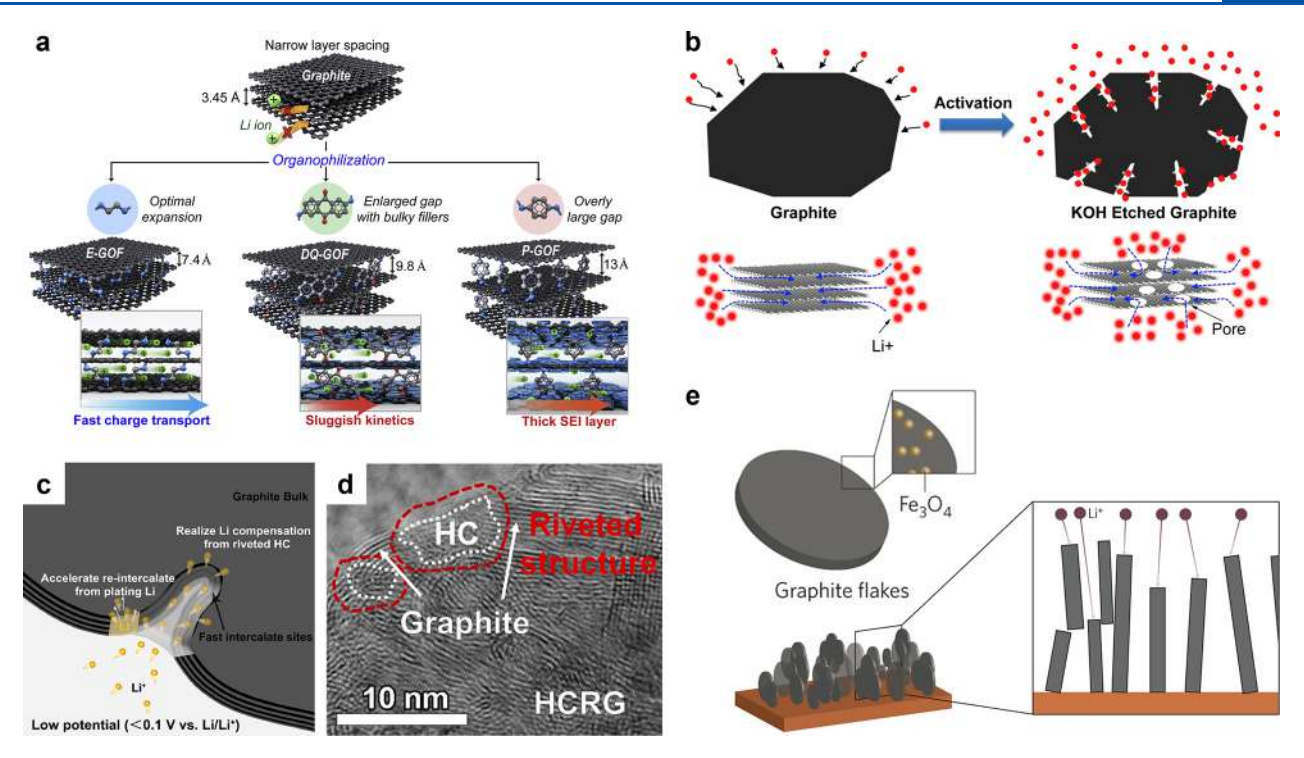


Figure 51. Design strategies for fast-charging flake graphite. (a) Schematic representation of the Li⁺ diffusion behavior of layered structure upon different interlayer spacing. Reproduced with permission from ref 300. Copyright 2022 Elsevier. (b) Schematic of the KOH etching process for creating a porous structure of graphite. Reproduced with permission from ref 305. Copyright 2015 Elsevier. (c) Design principle of hard carbon-riveted graphite (HCRG) anode and (d) corresponding TEM image. Reproduced with permission from ref 313. Copyright 2022 Elsevier. (e) Schematic of functional graphite flakes coated with superparamagnetic nanoparticles and the alignments of graphite particles under a rotating magnetic field during the electrode drying step. Reproduced with permission from ref 316. Copyright 2016 Springer Nature.

6.2.2. Single-Crystalline and Polycrystalline Graphite.

Single-crystalline graphite (or flake graphite) consists of highly ordered, anisotropic crystalline layers (Figure 50c), where Li intercalation follows a staged insertion process. The insertion of Li progressively increases the interlayer distance from 0.335 to 0.37 nm as it transitions through intermediate staging phases before reaching the fully lithiated LiC₆ state. ²⁹⁶ The in-plane diffusion within a single crystal is relatively fast, and the dominant basal planes manifest both smaller surface area and defect density, which can lead to suppressed SEI formation and Li loss, resulting in higher initial Coulombic efficiency (ICE) compared to polycrystalline graphite.²⁸⁹ However, the reduced number of edge planes of single-crystalline graphite makes the Li intercalation/deintercalation process the rate-limiting step. 297,298 In addition, its much larger particle size leads to elongated diffusion pathways, resulting in poor Li⁺ diffusion kinetics under fast charging conditions. These inferior kinetic properties of single-crystalline graphite result in higher electrochemical polarization, which can lead to severe Li deposition and dendrite growth when the reduction potential approaches or even falls below that of the Li metal.

In contrast, polycrystalline graphite (or microcrystalline graphite) consists of randomly oriented nanocrystalline domains (Figure 50d), creating an isotropic intercalation environment that facilitates faster Li diffusion and enhances electrochemical kinetics. This disordered structure mitigates Li⁺ concentration gradients, preventing localized ion accumulation and reducing the likelihood of lithium metal deposition. Moreover, randomly oriented microcrystalline structures distribute mechanical stress more uniformly, and the smaller disordered crystallites provide more isotropic expansion, minimizing the

risk of interparticle detachment and maintaining stable electrode integrity. By comparison, due to the accumulation of internal stress as Li ion intercalation, a highly anisotropic expansion (\sim 10%) of single-crystalline graphite along the *c*-axis was observed, resulting in delamination, microcracking, and eventual structural collapse. However, as a trade-off, the higher content of defects and impurities also results in lower ICE and reversible capacity of polycrystalline graphite compared with the single-crystalline counterpart.

6.2.3. Toward Fast-Charging Single-Crystalline Graphite. As previously discussed, the primary limitation of flake graphite in LIBs is its sluggish Li⁺ transport kinetics. To improve the rate capability of these highly anisotropic particles, extensive research has focused on structural engineering, surface

modification, and morphology control. In terms of materials engineering, the goal is to create more reactive sites for Li⁺ adsorption on flake graphite particles. One effective approach is expanding the interlayer distance to provide additional space for Li+ diffusion, thereby reducing diffusion resistance and significantly improving fast-charging capability (Figure 51a). 300,301 However, simply increasing the interlayer spacing does not always yield better performance, particularly when the spacing exceeds 0.42 nm, where Li intercalation no longer occurs spontaneously.302 Other modification strategies, such as introducing functional groups and structural defects, have been explored to further enhance both the rate capability and specific capacity of graphite.³⁰³ Another effective approach is the introduction of micropores on the surface of flake graphite particles (Figure 51b). By constructing ion channels within bulk graphite through methods such as etching 304,305 or thermal/mechanochemical reac-

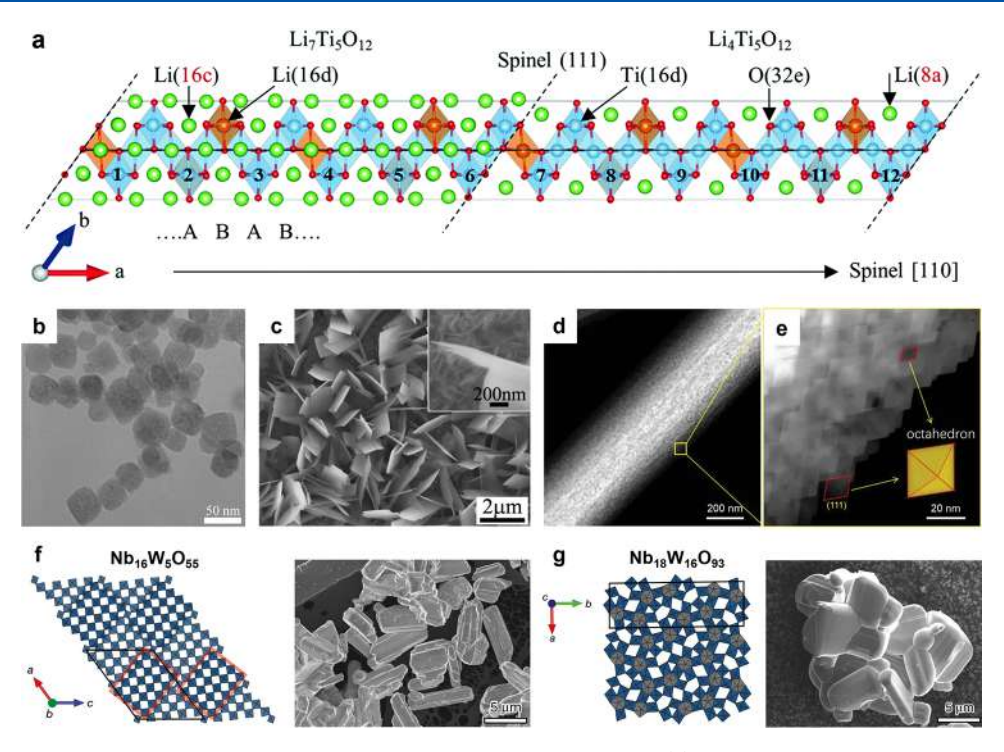


Figure 52. Crystallographic structure and design strategies of representative host materials. (a) Structure of the optimized stoichiometric two-phase $\text{Li}_7\text{Ti}_5\text{O}_{12}/\text{Li}_4\text{Ti}_5\text{O}_{12}$ model. Reproduced with permission from ref 328. Copyright 2016 Royal Society of Chemistry. (b) TEM image of single-crystalline LTO nanoparticles. Reproduced with permission from ref 337. Copyright 2012 Elsevier. (c) SEM image of LTO nanosheet arrays. Reproduced with permission from ref 338. Copyright 2014 Royal Society of Chemistry. (d,e) TEM images of mesoporous single-crystalline LTO microrods. Reproduced with permission from ref 340. Copyright 2022 John Wiley and Sons. Crystal structures and particle morphologies of (f) $\text{Nb}_{16}\text{W}_5\text{O}_{55}$ and (g) $\text{Nb}_{18}\text{W}_{16}\text{O}_{93}$. Reproduced with permission from ref 343. Copyright 2018 Springer Nature.

tions, ^{306,307} Li diffusion pathways are significantly shortened, thereby improving Li⁺ transport kinetics.

Surface modification has been widely recognized as an effective strategy for enhancing the rate capability and suppressing Li deposition. A variety of coating materials, including carbon, metal oxides, polymers, and inorganic compounds, have been explored. For instance, carbon coating via CVD/thermal vapor deposition (TVD) processes alters the surface properties of the graphite electrode, mitigating anisotropic intercalation, facilitating uniform potential distribution, and even tuning lithiophilicity (Figure 51c,d). Additionally, carbon coating effectively reduces the surface area of flake graphite, leading to a thinner and more homogeneous SEI layer. A high-quality SEI layer further prevents excessive side reactions between graphite and the electrolyte, improving the cycling stability.

The rate capability of flake graphite can also be improved by optimizing the particle size and shape. Milling or spheroidization effectively reduces the anisotropy of flake graphite, enhancing the internal ion diffusion. The resulting spherical particles not only improve Li⁺ transport but also increase tap density, leading to higher packing density and volumetric capacity within the battery. Turthermore, controlling the orientational distribution of anisotropic graphite flakes during electrode fabrication has been shown to enhance the Li⁺ transport kinetics. Billaud et al. demonstrated that applying an external magnetic field could modify graphite flakes into a biaxial orientation, aligning their basal planes perpendicular to the current collector (Figure 51e). This alignment significantly improves ion diffusion across the electrode due to the formation of a low-tortuosity structure. Additionally, the alignment angle has been correlated

with the specific capacity of graphite, indicating that the precise orientation control can further optimize battery performance.³¹⁷

6.3. Transition Metal Oxides

Various transition metal oxides (TMOs) have been extensively investigated as electrode materials for LIBs. Based on their reaction mechanisms, TMOs can be broadly classified into two categories: insertion- and conversion-type materials. For conversion-type TMOs (e.g., TM = cobalt (Co), nickel (Ni), Fe, Cu, rutile (Ru), manganese (Mn)), the anodes undergo conversion reactions during the charging process, which offers high theoretical specific capacities due to the complete reduction of metal ions to their elemental form.³¹⁸ Although the use of single-crystalline TMOs has been reported to enhance rate performance, the conversion process involves significant volume changes.^{11,319–323} During cycling, TMO is reduced to elemental metal, which results in drastic volume variations, leading to structural degradation and consequently poor cycling stability.³²⁴

By contrast, insertion-type TMOs (e.g., TM = titanium (Ti), niobium (Nb), vanadium(V)) undergo a highly reversible intercalation/deintercalation reaction during the charge/discharge process. Instead of reduction to elemental metal, lithiated phases of TMO can be formed. Consequently, the theoretical specific capacity is naturally lower than that of conversion-type TMOs, but they offer the advantage of structural stability, significantly improving cycle stability. ^{32.5}

For Ti, besides ${\rm TiO_2}$, the spinel-structured ${\rm Li_4Ti_5O_{12}}$ (LTO) has gained significant attention as an anode material due to its excellent structural stability. During charge–discharge process, LTO undergoes a phase transformation between spinel ${\rm Li_4Ti_5O_{12}}$ and rock salt ${\rm Li_7Ti_5O_{12}}$, with distinct phase

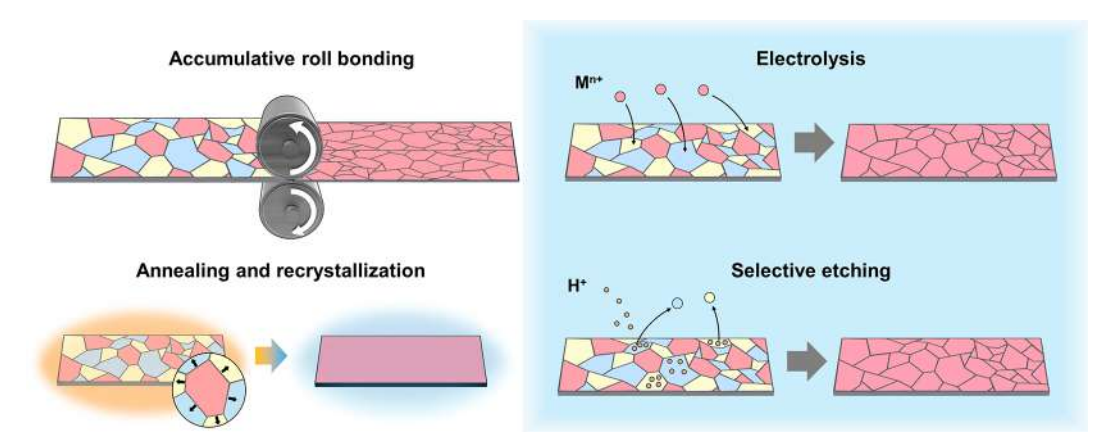


Figure 53. Schematic of representative fabrication methods for crystal plane-oriented metallic foils. The different colors represent different crystal planes.

boundaries observed along the (111) plane (Figure 52a).³²⁶ Since the lattice mismatch between these two phases is less than 1%, minimal stress is generated during Li insertion, resulting in the zero-strain characteristic of LTO.^{327,328} This unique property ensures minimal volume change during cycling, contributing to the long-term durability of LIBs.³²⁹

Despite its structural advantages, LTO suffers from low electrical conductivity ($\sim 10^{-13}~{\rm S}~{\rm cm}^{-1}$) and a limited Li⁺ diffusion coefficient ($10^{-9}~{\rm to}~10^{-13}~{\rm cm}^2~{\rm s}^{-1}$), which restrict its performance in high-rate applications. To overcome these limitations, various strategies have been explored, including structural engineering, ^{331,332} element doping, ^{333,334} and surface coating. Among these approaches, reducing LTO particle size to the nanoscale has proven to be particularly effective. By employing single-crystalline nanostructured LTO, the Li⁺ diffusion pathway is significantly shortened, improving ion transport kinetics and enhancing the rate performance of the material (Figure 52b,c). ^{337,338}

However, in nanostructured LTO, Li⁺ ions must diffuse across multiple grain boundaries, which can lead to ion trapping and a lower overall Li⁺ diffusion coefficient.³³⁹ In contrast, bulk single-crystalline LTO, with its reduced grain boundaries, offers more efficient Li⁺ transport due to an uninterrupted diffusion pathway. Jiao et al. synthesized mesoporous single-crystalline LTO microrods with an interconnected mesoporous network, which enhances electrolyte penetration and improves Li⁺ accessibility to active sites (Figure 52d,e).³⁴⁰ The high porosity further reduces tortuosity, ensuring efficient electrolyte percolation and an overall improved electrochemical performance. Additionally, its higher tap density addresses the practical limitations associated with nanostructured LTO materials.

Niobium pentoxide (Nb₂O₅) has attracted significant attention as a promising electrode material due to its ultrafast lithium storage kinetics. Among its various crystalline phases, orthorhombic Nb₂O₅ (T-Nb₂O₅) and monoclinic Nb₂O₅ (H-Nb₂O₅) are two widely studied structures. A well-recognized trade-off exists between these two phases: Nb₂O₅ offers superior structural stability, while H-Nb₂O₅ delivers a higher specific capacity of approximately 250 mAh g⁻¹ and exhibits a flat charge/discharge plateau around 1.65 V (vs Li⁺/Li). However, the enhanced capacity of H-Nb₂O₅ stems from a two-phase transition process, which adversely deteriorates its cycling stability. To address this issue, Li et al. introduced an amorphous nitrogen-doped carbon shell over micron-sized single-crystal H-Nb₂O₅, effectively mitigating anisotropic

electron and ion transport. This strategy prevents asynchronous phase transitions and enhances the electrochemical performance of the material. Similarly, Xiong et al. demonstrated that single-crystalline H-Nb₂O₅ oriented along the (001) direction can better accommodate volume changes while shortening the Li⁺ diffusion pathways, leading to improved rate capability and cycle stability. 342

As mentioned above, a persistent challenge in electrode material design is the trade-off between particle size and rate performance. Micron-sized particles offer high tap density and are advantageous for volumetric energy density, but they usually suffer from poor rate performance due to elongated Li⁺ diffusion pathway. This dilemma, however, may be addressed using Wadsley-Roth oxides (WROs). Griffith et al. reported that two niobium tungsten oxides, Nb₁₆W₅O₅₅ and Nb₁₈W₁₆O₉₃, are capable of intercalating large amounts of Li⁺ at high rates, even when the particle size is on the micrometer scale (Figure 52f,g).³⁴³ The outstanding volumetric capacities and rate performance could be attributed to multielectron redox reactions, buffered volume expansion, topologically frustrated niobium/tungsten polyhedral frameworks, and rapid solid-state lithium transport. Guo et al. further identified (010)-preferred Li⁺ transport in Nb₁₆W₅O₅₅ crystals as a critical bottleneck for achieving fast charging. 344 By creating a Li-rich layer to facilitate the rapid transfer of Li⁺ ions to the (010)-faceted entrance and alleviate the spatial and temporal anisotropy of Li⁺ insertion/ extraction, the material manifests enhanced rate performance due to local inhomogeneities during fast charging and discharging cycles. Li et al. further advanced the field by synthesizing a series of micron-sized single-crystalline WROs. Their study revealed that the fast Li⁺ diffusion in these materials is closely related to unique phonon anomalies, which enhance the pre-exponential factor in the Arrhenius-type diffusivity. Additionally, the presence of Nb was shown to be essential for creating the WRO framework and achieving high-rate performance.34

Vanadium oxides, particularly V₂O₅, possess a layered structure that facilitates the reversible Li⁺ insertion and extraction. Their lithiated derivatives are therefore considered promising anode materials for LIBs.³²⁵ Liu et al. proposed the use of disordered rock salt Li₃V₂O₅ as a fast-charging anode that can reversibly cycle two Li⁺ at an average voltage of about 0.6 V versus a Li/Li⁺ reference electrode.³⁴⁶ Given the favorable electrochemical characteristics and promising potential of disordered rock salt materials, further insights from a crystallo-

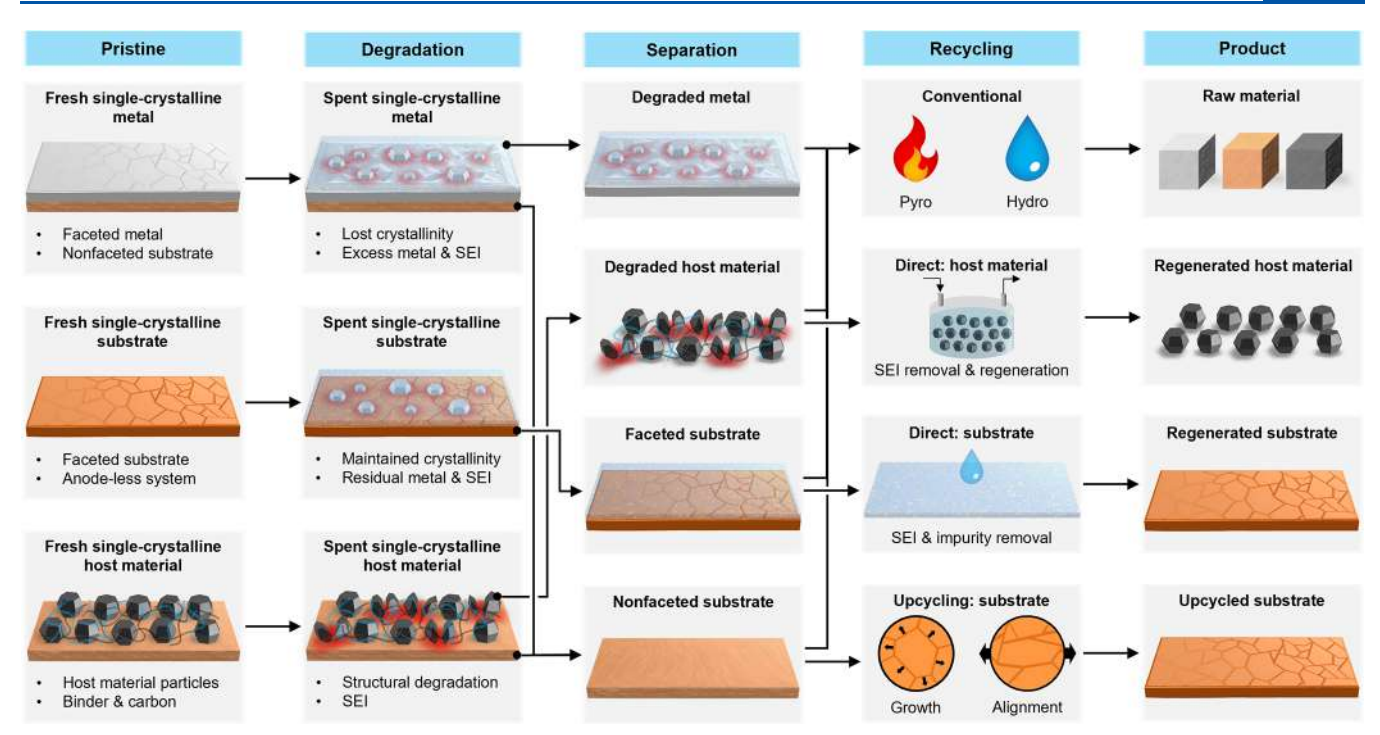


Figure 54. Schematic of possible recycling approaches of a single-crystalline metal, substrate, and host material.

graphic perspective are essential, as even "disordered" systems display local symmetry preferences, short-range ordering, and facet-dependent properties.

In conclusion, the role of single-crystalline properties can differ markedly in ion batteries, where the host materials undergo Li alloying or insertion reactions. Beyond improving structural stability, single crystals reduce the number of grain boundaries, thereby facilitating ion transport and enhancing the intercalation kinetics and rate performance. However, it remains essential to strike a balance, as bulk single-crystalline host materials may introduce longer Li⁺ diffusion pathways that could limit overall performance. Moreover, it would be worthwhile to revisit materials that already have a well-established understanding from a crystallographic perspective, as this could reveal new opportunities for optimizing ion transport and structural design for other future applications.

7. FABRICATION AND RECYCLING

7.1. Fabrication of Single-Crystalline Anodes

The above discussion mainly focuses on the strategies for crystallographic alignment of metallic electrodeposits. However, it is also important to note that some substrates themselves are single-crystalline metals, requiring specialized fabrication methods for their synthesis before they are used in electrodeposition. In this section, we focus on summarizing the recent advances in the fabrication of single-crystalline metal anodes or substrates (Figure 53). It should be noted that the fabrication of single-crystalline host materials is not included here, as these methods are already quite mature. For example, techniques adopted from the semiconductor industry—such as bottom-up and top-down synthesis of single-crystalline Si nanowires—are well established and readily scalable. 347,348 Similarly, for singlecrystalline TMOs, precisely controlled calcination processes can recrystallize polycrystalline structures and effectively eliminate grain boundaries, yielding bulk single-crystalline particles. 342,343,345

7.1.1. Accumulative Roll Bonding. Accumulative roll bonding (ARB) is one of the most widely used metallurgical methods to induce severe plastic deformation in metals, enabling the formation of fine-grained materials. ³⁴⁹ In a typical ARB process, a mechanical roller press is used to roll and fold an ingot repeatedly, generating deformation and dislocations within its microstructure. Studies have successfully demonstrated that repeated rolling can trigger grain boundary sliding in crystals, which facilitates the manufacturing of high-strength bulk materials. ³⁵⁰

ARB is particularly suitable for metals with high ductility, as they are more prone to deformation and creep compared to those with high modulus.³⁵¹ Consequently, numerous studies have explored its use in synthesizing crystallographic-textured Li.^{94,95} Shen et al.³⁵² reported the fabrication of Li(110) and Li(200) textures via a roll-to-roll process, demonstrating that the crystal facet of rolled Li can be tailored by adjusting the number of rolling cycles. Specifically, a Li(110)-oriented metallic foil was obtained after six cycles of ARB, whereas a Li(200) metallic foil was achieved after 20 cycles.

ARB has also been applied in the fabrication of crystal plane-oriented Zn and Na. 353 Liang et al. 191 combined ARB with annealing at the deformation temperature to produce (002)-textured Zn with enhanced electrochemical performance. Zhang et al. 354 modified commercial Zn through ARB to expose more Zn(002) planes and further rolled the textured Zn with a stainless-steel mesh to construct a highly reversible, 3D rearranged (002)-textured Zn anode, enabled by a curvature-enhanced adsorbate coverage mechanism.

7.1.2. Annealing. Annealing is an alternative approach for achieving crystal plane-oriented metallic foils. Unlike mechanical processes that induce plastic deformation, annealing is a coarsening technique that eliminates grain boundaries and increases grain size. By carefully tuning the annealing parameters, colossal grain growth can be achieved, leading to

the formation of single-crystalline substrates with specific crystallographic orientations.³⁵⁶

As a result, many studies have reported the synthesis of single-crystalline Li and Zn using an annealing-recrystallization process. ^{29,194,195,357,358} Additionally, as previously mentioned, single-crystalline Cu substrates have been extensively investigated as current collectors for anode-free Li and aqueous Znion batteries. The fabrication of single-crystalline Cu with different facets, including (100), (110), and (111), can be precisely controlled by adjusting the annealing temperature, heating duration, and cooling rate. ^{30,60,120,197,359,360} In addition, the annealing treatment of commercial Al foil is also employed for the fabrication of single-crystalline Al (100) substrates, which favors uniform Na metal deposition behaviors. ^{240,241}

7.1.3. Electrolysis and Selective Etching. For nonairsensitive metals, electrolysis and selective etching are effective methods for achieving crystal plane orientation. Differences in surface energy between crystallographic facets lead to preferential deposition or etching, enabling the fabrication of crystal plane-oriented metallic substrates.

Huang et al.³⁶¹ successfully demonstrated the fabrication of large-scale Zn anodes with a 99% Zn(002) relative texture coefficient using commercial polycrystalline Zn substrates in a ZnSO₄/H₂SO₄/KMnO₄ electroplating solution. Interestingly, the byproduct generated during the process was subsequently utilized as a cathode, benefiting from MnO₄⁻ evolution during electrodeposition. Chen et al.¹²⁴ also introduced the preferential deposition of Cu(220) in a saturated LiFSI environment. The electrolysis process is cost-effective and holds promise for the continuous, decimeter-scale fabrication of single-crystalline Cu substrates further supported by other studies. ^{118,199} For selective etching, phosphoric acid has been reported as an effective etchant for producing Zn(002)-oriented ^{362,363} and Zn(100)-oriented ³⁶⁴ metallic substrates.

7.2. Recycling of Single-Crystalline Anodes

Along with the extensive development of novel battery chemistries using single-crystalline anode materials, achieving a sustainable and closed-loop life cycle for new battery systems is crucial. Recently, recycling spent batteries has become increasingly important for environment and resource substainability. Given that single-crystalline anode materials require supplementary fabrication steps, as discussed previously, enabling an even more closed-loop life cycle is imperative from an environmental viewpoint. This section aims to provide our perspective on possible recycling scenarios using three different types of single-crystalline anode materials (metal, substrate, and host material) from their degradation to separation, recycling, and final products (Figure 54).

7.2.1. Degradation. The battery materials undergo different types and modes of degradation after extended cycling. Thus, it is crucial to understand the common degradation types for each anode material. Single-crystalline metal has a faceted metal surface and a nonfaceted substrate as a current collector. After cycling, the surface metal may lose its crystallinity due to uncontrolled growth of crystals or even dendrites, leading to excess dead metal and SEI layers. Similarly, a single-crystalline substrate has a faceted substrate where metals are electrodeposited directly onto the substrate surface. Because the substrate itself is electrochemically inert, the crystallinity of the substrate surface should be preserved after long-term cycling in the presence of residual metal and SEI on the surface. Unlike the other two, single-crystalline host material is typically composed

of active material, binder, and carbon to form a composite electrode on a nonfaceted current collector substrate. The main source of degradation is structural degradation of materials, which impedes metal ion insertion and promotes SEI formation on the surface.

7.2.2. Separation. The degraded electrodes can be separated into different components. Spent metal can be separated into degraded metal and nonfaceted substrate, spent substrate into faceted substrate, and spent host material into degraded host material and nonfacet substrate. The separation process may require physical or chemical methods to separate the metal or composite electrode from the substrate. It should be noted that spent batteries are typically shredded altogether in the battery recycling industry. Here, we hypothesize a complete separation of the anode from other battery components, such as the cathode and separator, for the full advantage of later recycling processes. Nevertheless, advanced disassembly and separation processes of spent batteries are needed for higher yields and lower impurities. 372

7.2.3. Recycling. The conventional recycling approaches are pyrometallurgy and hydrometallurgy. Pyrometallurgy ^{373,374} uses high heat (>1000 °C), and hydrometallurgy ^{375–377} uses a leaching agent (<200 °C) to extract raw materials. The main advantage of these methods is their broad applicability, where the separated materials can be recycled into raw materials regardless of their chemistries. ^{378,379} However, since the raw materials eventually need to be refabricated, the total energy consumption and economic returns are not as appealing as those of other methods.

Direct recycling has attracted a lot of attention in cathode recycling due to its energy, economic, and environmental efficiency. $^{380-384}$ For single-crystalline host materials, similar direct recycling methods can be applied to remove SEI and regenerate the structural degradation of the anode materials as widely investigated in graphite recycling. 385-390 It should be noted that additional annealing or calcination processes may be needed to regrow the single crystals from the degraded crystal structures. The direct recycling approach could be even more attractive for single-crystalline substrates. Unlike the metal anode or host material, the crystallinity of the substrate is maintained, as it is an electrochemically inert component. By removal of the SEI and impurities on the surface with chemical treatment, the single-crystalline substrate should be reusable. In addition, the simplicity of the recycling procedure of singlecrystalline substrates compensates for the complex disassembly and separation processes (i.e., without shredding) needed to maintain their physical integrity.

An upcycling approach has been proposed for cathode materials to simultaneously regenerate and increase energy density of active materials. We propose that nonfaceted substrate previously used as a current collector for metal or host materials can be upcycled into faceted substrate by growing or aligning desired crystal grains using the fabrication methods discussed in Section 7.1. This approach can even be applied to spent LIBs that widely use Cu as current collectors, paving the way for sustainable fabrication and recycling of next-generation anode-free batteries.

To sum up, fabrication and recycling of battery materials are indispensable yet largely overlooked aspects in practical implementation of developed materials into battery devices. As more design strategies for anode materials will rely on their crystallographic engineering, the same research and develop-

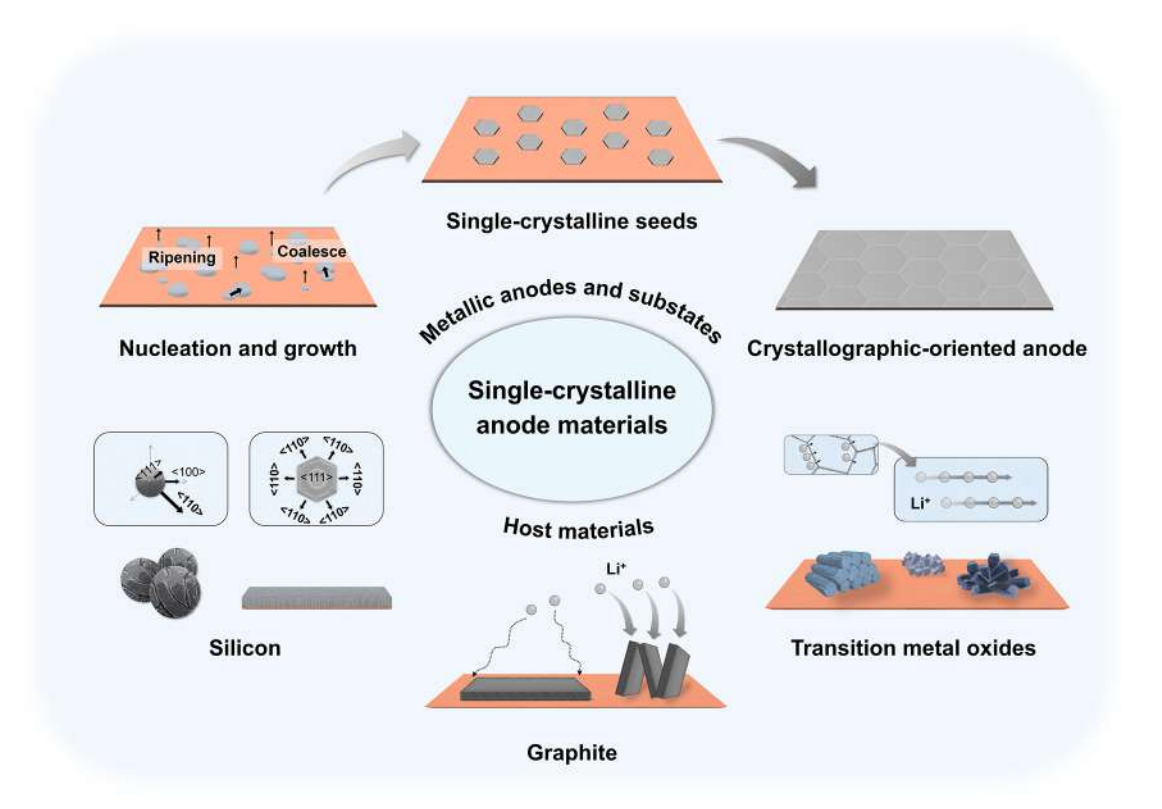


Figure 55. Summary of the use of single-crystal materials as anodes for battery applications.

ment efforts are needed for their scalable and sustainable fabrication and recycling.

8. CONCLUSION AND OUTLOOK

In this review, an understanding of and insights into single-crystalline anode materials is presented. The research progress in the utilization of single-crystalline materials such as metallic anodes, substrates, and host materials has been thoroughly summarized for both metal batteries and ion batteries (Figure 55).

To understand the electrochemical crystallization process, crystal nucleation, incubation, and growth theories are summarized in detail, with the focus on deciphering the descriptors that exhibit a significant influence on the electrodeposition process. To be specific, the lattice mismatch between substrates and metal nuclei, overpotential, temperature, and pressure are identified as critical determinants, and their impact on the nucleation and growth of metal electrodeposits is elucidated. The recent achievements involving the utilization of these strategies in advanced metal batteries (Li, Zn, Na, Al, and Mg) have been reviewed comprehensively. The as-formed crystal plane-oriented single-crystalline metals manifest uniform and highly reversible electroplating/stripping behaviors, while mitigating the side reactions at the interface.

For host materials, the effect of adopting single-crystalline structures can differ substantially from their role in controlling crystal growth in metal batteries. Using three representative yet distinct host systems (Si, graphite, and TMOs), their fundamentals, failure mechanisms, and material design strategies are revisited from a crystallographic perspective.

Additionally, representative fabrication methods for singlecrystalline metals and substrates are summarized. For a sustainable and closed-loop life cycle of next-generation batteries, possible recycling approaches for single-crystalline metals, substrates, and host materials are discussed and proposed.

Finally, we present our perspective on potential research directions that warrant further exploration of single-crystalline anode materials.

- 1 More advanced strategies are needed to enable large-scale, bulk single-crystalline metal electrodeposits with minimal defects. In the application of single-crystalline metallic anodes and substrates for metal batteries, obtaining a relative ratio of the desired facet close to unity remains a challenge. XRD patterns often reveal multiple peaks, indicating imperfect alignment and limited effectiveness of current strategies. Moreover, while the concept of a single crystal is typically considered at the particle level, grain boundaries and defects persist in metallic electrodeposits, influencing nucleation and growth both thermodynamically and kinetically. Therefore, achieving large-scale, bulk single-crystalline electrodeposits with minimal grain boundaries could significantly enhance battery performance. Potential strategies include substrate engineering with functional materials, SEI engineering for preferred facet growth, and optimization/ exploration of operation conditions.
- 2 A deeper understanding of single-crystalline materials is essential, as many questions remain unresolved. For instance, while various Cu facets have been reported to facilitate Li/Zn deposition, ongoing debate persists regarding which facet is optimal and how each affects the metal deposition process. Furthermore, the influence of different facets on SEI formation should be comprehensively elucidated with different types of substrates and electrolyte chemistries, as SEI plays the

most crucial role in crystal growth of metals. Addressing these uncertainties also requires advanced characterization techniques and simulation tools to provide deeper insights.

- 3 Practical-level battery performance needs to be demonstrated using single-crystalline anode materials. Most state-of-the-art battery performance metrics have been achieved under mild, laboratory conditions, such as high N/P ratios (or low depth of discharge), flooded electrolytes, low areal capacity and current density, and small-sized cell format. To assess the practical viability of single-crystalline anodes, it is crucial to validate their performance under practical conditions and explore their scalability from coin cells to Ah-level pouch cells.
- 4 More effective fabrication methods need to be developed for the practical employment of single-crystalline anode materials. The fabrication methods discussed in Section 7.1. remain economical and scalable, yet each method has its own drawbacks. To be specific, although the ARB process can be done simply by repeated rolling and folding to align the crystal planes, performing tens of repetitions can be time-consuming. The process also continuously introduces grain boundaries, which may hinder transport kinetics and corrosion resistance of the metal. Annealing requires precise control of the process parameters to achieve selective grain growth. Parameters such as heating temperature, duration, and cooling rate all influence the extent of grain growth and the final microstructure of the metal. For electrolysis and selective etching, the cost of electrolytes and reactive agents must be considered when evaluating the overall cost-effectiveness. While deposition and etching processes can be integrated with the state-of-the-art metallic foil preparation techniques, they often require several hours to achieve the desired crystal plane orientation, potentially reducing manufacturing throughput. Overall, to enable real-world implementation of single-crystalline metals and substrates, the development of more effective fabrication methods is essential.
- 5 A recycling strategy should be considered when designing cells with single-crystalline anode materials. Considering the higher manufacturing cost of single-crystalline materials, as well as expensive materials cost for Li and Cu, a practical recycling strategy should be conceived from separation to regeneration and final product. Apart from conventional pyrometallurgy and hydrometallurgy, a more closed-loop approach such as direct recycling or upcycling techniques should be developed and demonstrated for not only economic efficiency, but also environmental and resource efficiency.

AUTHOR INFORMATION

Corresponding Authors

Qingyang Yin — Aiiso Yufeng Li Family Department of Chemical and Nano Engineering, University of California, San Diego, La Jolla, California 92093, United States; orcid.org/0009-0005-8882-1456; Email: q9yin@

orcia.org/0009-0005-8882-1456; Email: q9yin ucsd.edu

Zheng Chen — Aiiso Yufeng Li Family Department of Chemical and Nano Engineering, University of California, San Diego, La Jolla, California 92093, United States; Sustainable Power and Energy Center, University of California, San Diego, La Jolla, California 92093, United States; Program of Materials Science and Engineering, University of California, San Diego, California 92093, United States; oorcid.org/0000-0002-9186-4298; Email: zhc199@ucsd.edu

Authors

Dong Ju Lee — Aiiso Yufeng Li Family Department of Chemical and Nano Engineering, University of California, San Diego, La Jolla, California 92093, United States; orcid.org/0000-0002-8583-4957

Dapeng Xu − Aiiso Yufeng Li Family Department of Chemical and Nano Engineering, University of California, San Diego, La Jolla, California 92093, United States; ocid.org/0009-0007-1544-7824

Complete contact information is available at: https://pubs.acs.org/10.1021/acs.chemrev.5c00306

Author Contributions

CRediT: **Dong Ju Lee** conceptualization, writing — original draft, writing — review and editing; **Qingyang Yin** conceptualization, writing — original draft, writing — review and editing; **Dapeng Xu** writing — original draft, writing — review and editing; **Zheng Chen** conceptualization, funding acquisition, writing — review and editing

Notes

The authors declare no competing financial interest.

Biographies

Zheng Chen is a Professor at University of California in Aiiso Yufeng Li Family Department of Chemical and Nano Engineering. He received his B.S. from Tianjin University (2007) and Ph.D. from University of California, Los Angeles (2012). Then he served as a postdoctoral researcher at Stanford University before joining University of California San Diego in 2016. His research focuses on designing new materials and green processes for sustainable energy storage and conversion. He received the ECS Toyota Young Investigator Award (2024), the ECS Battery Division Early Career Award (2023), the NASA Early Career Faculty Award (2018), the LG Chem Global Battery Innovation Contest (BIC) Award (2018), and the ACS PRF New Investigator Award (2018).

Dong Ju Lee is a doctoral student at University of California, San Diego in Aiiso Yufeng Li Family Department of Chemical and Nanoengineering. He received his B.S. and M.S. from University of California, San Diego (2021 and 2022). His research primarily focuses on developing anode materials and fabrication designs for lithium all-solid-state-batteries.

Qingyang Yin is a postdoctoral researcher at University of California, San Diego in Aiiso Yufeng Li Family Department of Chemical and Nanoengineering. He received his B.S. from Tongji University (2019) and Ph.D. from University of California, Los Angeles (2024). His research primarily focuses on developing anode materials for Li metal batteries and aqueous Zn-ion batteries.

Dapeng Xu is a doctoral student at University of California, San Diego in Aiiso Yufeng Li Family Department of Chemical and Nanoengineering. He received his B.S. from Tianjin University (2016) and M.S. from Worcester Polytechnic Institute (2018). His research primarily focuses on developing material and cell designs for sodium all-solid-state batteries.

ACKNOWLEDGMENTS

This work was supported by LG Energy Solution—U.C. San Diego Frontier Research Laboratory (FRL) via the Open Innovation program and the National Science Foundation through the Future Manufacturing (FM) grant no. 2134764. This work is also related to the Aqueous Battery Consortium, an energy innovation hub under the US Department of Energy, Office of Basic Energy Sciences, Division of Materials Science and Engineering.

ABBREVIATIONS

Two-dimensional Three-dimensional Three-dimensional AE Aqueous electrolyte AES Auger electron spectroscopy AFE All-fluorinated electrolyte AFM Atomic force microscopy AIMD Molecular dynamics a-Li_xSi Amorphous lithium—silicon All F All-fluorinated carbonate electrolyte ARB Accumulative roll bonding a-Si Amorphous Si BCC Body-centered cubic BF Bright field CCD Critical current density CCE Commercial carbonate electrolyte CE Coulombic efficiency CNT Carbon nanotube cryo-TEM Cryogenic-transmission electron microscopy c-Si Crystalline Si CV Cyclic voltammetry CVD Chemical vapor deposition DEC Diethyl carbonate DFT Density functional theory DMAC Dimethylacetamide DMC Dimethylacetamide DMC Dimethyl carbonate DME Dimethoxyethane DOL Dioxlane DOLDME Electron backscatter diffraction EC Ethylene carbonate EDS Energy dispersive spectroscopy	1T-VSe ₂	1T-vanadium diselenide
AD Four-dimensional AE Aqueous electrolyte AES Auger electron spectroscopy AFE All-fluorinated electrolyte AFM Atomic force microscopy AIMD Molecular dynamics a-Li_xSi Amorphous lithium—silicon All F All-fluorinated carbonate electrolyte ARB Accumulative roll bonding a-Si Amorphous Si BCC Body-centered cubic BF Bright field CCD Critical current density CCE Commercial carbonate electrolyte CE Coulombic efficiency CNT Carbon nanotube cryo-TEM Cryogenic-transmission electron microscopy c-Si Crystalline Si CV Cyclic voltammetry CVD Chemical vapor deposition DEC Diethyl carbonate DFT Density functional theory DMAC Dimethylacetamide DMC Dimethyl carbonate DME Dimethoxyethane DOL Dioxlane DOLDME Dilute ether electrolyte with LiNO ₃ additive EBSD Electron backscatter diffraction EC Ethylene carbonate	2D	Two-dimensional
AES Auger electron spectroscopy AFE All-fluorinated electrolyte AFM Atomic force microscopy AIMD Molecular dynamics a-Li_xSi Amorphous lithium—silicon All F All-fluorinated carbonate electrolyte ARB Accumulative roll bonding a-Si Amorphous Si BCC Body-centered cubic BF Bright field CCD Critical current density CCE Commercial carbonate electrolyte CE Coulombic efficiency CNT Carbon nanotube cryo-TEM Cryogenic-transmission electron microscopy c-Si Crystalline Si CV Cyclic voltammetry CVD Chemical vapor deposition DEC Diethyl carbonate DFT Density functional theory DMAC Dimethylacetamide DMC Dimethyl carbonate DME Dimethoxyethane DOL Dioxlane DOLDME Electron backscatter diffraction EC Ethylene carbonate	3D	Three-dimensional
AES Auger electron spectroscopy AFE All-fluorinated electrolyte AFM Atomic force microscopy AIMD Molecular dynamics a-Li_xSi Amorphous lithium—silicon All F All-fluorinated carbonate electrolyte ARB Accumulative roll bonding a-Si Amorphous Si BCC Body-centered cubic BF Bright field CCD Critical current density CCE Commercial carbonate electrolyte CE Coulombic efficiency CNT Carbon nanotube cryo-TEM Cryogenic-transmission electron microscopy c-Si Crystalline Si CV Cyclic voltammetry CVD Chemical vapor deposition DEC Diethyl carbonate DFT Density functional theory DMAC Dimethylacetamide DMC Dimethyl carbonate DME Dimethoxyethane DOL Dioxlane DOLDME Electron backscatter diffraction EC Ethylene carbonate	4D	Four-dimensional
AES Auger electron spectroscopy AFE All-fluorinated electrolyte AFM Atomic force microscopy AIMD Molecular dynamics a-Li_xSi Amorphous lithium—silicon All F All-fluorinated carbonate electrolyte ARB Accumulative roll bonding a-Si Amorphous Si BCC Body-centered cubic BF Bright field CCD Critical current density CCE Commercial carbonate electrolyte CE Coulombic efficiency CNT Carbon nanotube cryo-TEM Cryogenic-transmission electron microscopy c-Si Crystalline Si CV Cyclic voltammetry CVD Chemical vapor deposition DEC Diethyl carbonate DFT Density functional theory DMAC Dimethylacetamide DMC Dimethyl carbonate DME Dimethoxyethane DOL Dioxlane DOLDME Electron backscatter diffraction EC Ethylene carbonate	AE	Aqueous electrolyte
AFE All-fluorinated electrolyte AFM Atomic force microscopy AIMD Molecular dynamics a-Li _x Si Amorphous lithium—silicon All F All-fluorinated carbonate electrolyte ARB Accumulative roll bonding a-Si Amorphous Si BCC Body-centered cubic BF Bright field CCD Critical current density CCE Commercial carbonate electrolyte CE Coulombic efficiency CNT Carbon nanotube cryo-TEM Cryogenic-transmission electron microscopy c-Si Crystalline Si CV Cyclic voltammetry CVD Chemical vapor deposition DEC Diethyl carbonate DFT Density functional theory DMAC Dimethylacetamide DMC Dimethyl carbonate DME Dimethoxyethane DOL Dioxlane DOLDME Electron backscatter diffraction EC Ethylene carbonate	AES	
AIMD Molecular dynamics a-Li _x Si Amorphous lithium—silicon All F All-fluorinated carbonate electrolyte ARB Accumulative roll bonding a-Si Amorphous Si BCC Body-centered cubic BF Bright field CCD Critical current density CCE Commercial carbonate electrolyte CE Coulombic efficiency CNT Carbon nanotube cryo-TEM Cryogenic-transmission electron microscopy c-Si Crystalline Si CV Cyclic voltammetry CVD Chemical vapor deposition DEC Diethyl carbonate DFT Density functional theory DMAC Dimethylacetamide DMC Dimethyl carbonate DME Dimethoxyethane DOL Dioxlane DOLDME Dilute ether electrolyte with LiNO ₃ additive EBSD Electron backscatter diffraction EC Ethylene carbonate	AFE	
a-Li _x Si Amorphous lithium—silicon All F All-fluorinated carbonate electrolyte ARB Accumulative roll bonding a-Si Amorphous Si BCC Body-centered cubic BF Bright field CCD Critical current density CCE Commercial carbonate electrolyte CE Coulombic efficiency CNT Carbon nanotube cryo-TEM Cryogenic-transmission electron microscopy c-Si Crystalline Si CV Cyclic voltammetry CVD Chemical vapor deposition DEC Diethyl carbonate DFT Density functional theory DMAC Dimethylacetamide DMC Dimethylacetamide DMC Dimethyl carbonate DME Dimethoxyethane DOL Dioxlane DOLDME Electron backscatter diffraction EC Ethylene carbonate	AFM	Atomic force microscopy
All F All-fluorinated carbonate electrolyte ARB Accumulative roll bonding a-Si Amorphous Si BCC Body-centered cubic BF Bright field CCD Critical current density CCE Commercial carbonate electrolyte CE Coulombic efficiency CNT Carbon nanotube cryo-TEM Cryogenic-transmission electron microscopy c-Si Crystalline Si CV Cyclic voltammetry CVD Chemical vapor deposition DEC Diethyl carbonate DFT Density functional theory DMAC Dimethylacetamide DMC Dimethyl carbonate DME Dimethoxyethane DOL Dioxlane DOLDME EBSD Electron backscatter diffraction EC Ethylene carbonate	AIMD	Molecular dynamics
All F All-fluorinated carbonate electrolyte ARB Accumulative roll bonding a-Si Amorphous Si BCC Body-centered cubic BF Bright field CCD Critical current density CCE Commercial carbonate electrolyte CE Coulombic efficiency CNT Carbon nanotube cryo-TEM Cryogenic-transmission electron microscopy c-Si Crystalline Si CV Cyclic voltammetry CVD Chemical vapor deposition DEC Diethyl carbonate DFT Density functional theory DMAC Dimethylacetamide DMC Dimethyl carbonate DME Dimethoxyethane DOL Dioxlane DOLDME EBSD Electron backscatter diffraction EC Ethylene carbonate	a-Li _x Si	Amorphous lithium-silicon
a-Si Amorphous Si BCC Body-centered cubic BF Bright field CCD Critical current density CCE Commercial carbonate electrolyte CE Coulombic efficiency CNT Carbon nanotube cryo-TEM Cryogenic-transmission electron microscopy c-Si Crystalline Si CV Cyclic voltammetry CVD Chemical vapor deposition DEC Diethyl carbonate DFT Density functional theory DMAC Dimethylacetamide DMC Dimethyl carbonate DME Dimethoxyethane DOL Dioxlane DOLDME Dilute ether electrolyte with LiNO3 additive EBSD Electron backscatter diffraction EC Ethylene carbonate	All F	
BCC Bright field CCD Critical current density CCE Commercial carbonate electrolyte CE Coulombic efficiency CNT Carbon nanotube cryo-TEM Cryogenic-transmission electron microscopy c-Si Crystalline Si CV Cyclic voltammetry CVD Chemical vapor deposition DEC Diethyl carbonate DFT Density functional theory DMAC Dimethylacetamide DMC Dimethyl carbonate DME Dimethoxyethane DOL Dioxlane DOLDME EBSD Electron backscatter diffraction EC Ethylene carbonate	ARB	Accumulative roll bonding
BF Bright field CCD Critical current density CCE Commercial carbonate electrolyte CE Coulombic efficiency CNT Carbon nanotube cryo-TEM Cryogenic-transmission electron microscopy c-Si Crystalline Si CV Cyclic voltammetry CVD Chemical vapor deposition DEC Diethyl carbonate DFT Density functional theory DMAC Dimethylacetamide DMC Dimethyl carbonate DME Dimethoxyethane DOL Dioxlane DOLDME Dilute ether electrolyte with LiNO3 additive EBSD Electron backscatter diffraction EC Ethylene carbonate	a-Si	Amorphous Si
CCD Critical current density CCE Commercial carbonate electrolyte CE Coulombic efficiency CNT Carbon nanotube cryo-TEM Cryogenic-transmission electron microscopy c-Si Crystalline Si CV Cyclic voltammetry CVD Chemical vapor deposition DEC Diethyl carbonate DFT Density functional theory DMAC Dimethylacetamide DMC Dimethyl carbonate DME Dimethoxyethane DOL Dioxlane DOLDME Dilute ether electrolyte with LiNO3 additive EBSD Electron backscatter diffraction EC Ethylene carbonate	BCC	Body-centered cubic
CCE Commercial carbonate electrolyte CE Coulombic efficiency CNT Carbon nanotube cryo-TEM Cryogenic-transmission electron microscopy c-Si Crystalline Si CV Cyclic voltammetry CVD Chemical vapor deposition DEC Diethyl carbonate DFT Density functional theory DMAC Dimethylacetamide DMC Dimethyl carbonate DME Dimethoxyethane DOL Dioxlane DOLDME Dilute ether electrolyte with LiNO3 additive EBSD Electron backscatter diffraction EC Ethylene carbonate	BF	Bright field
CCE Commercial carbonate electrolyte CE Coulombic efficiency CNT Carbon nanotube cryo-TEM Cryogenic-transmission electron microscopy c-Si Crystalline Si CV Cyclic voltammetry CVD Chemical vapor deposition DEC Diethyl carbonate DFT Density functional theory DMAC Dimethylacetamide DMC Dimethyl carbonate DME Dimethoxyethane DOL Dioxlane DOLDME Dilute ether electrolyte with LiNO3 additive EBSD Electron backscatter diffraction EC Ethylene carbonate	CCD	Critical current density
CNT Carbon nanotube cryo-TEM Cryogenic-transmission electron microscopy c-Si Crystalline Si CV Cyclic voltammetry CVD Chemical vapor deposition DEC Diethyl carbonate DFT Density functional theory DMAC Dimethylacetamide DMC Dimethyl carbonate DME Dimethoxyethane DOL Dioxlane DOLDME Dilute ether electrolyte with LiNO3 additive EBSD Electron backscatter diffraction EC Ethylene carbonate	CCE	
cryo-TEM Cryogenic-transmission electron microscopy c-Si Crystalline Si CV Cyclic voltammetry CVD Chemical vapor deposition DEC Diethyl carbonate DFT Density functional theory DMAC Dimethylacetamide DMC Dimethyl carbonate DME Dimethoxyethane DOL Dioxlane DOLDME Dilute ether electrolyte with LiNO3 additive EBSD Electron backscatter diffraction EC Ethylene carbonate	CE	Coulombic efficiency
c-Si Crystalline Si CV Cyclic voltammetry CVD Chemical vapor deposition DEC Diethyl carbonate DFT Density functional theory DMAC Dimethylacetamide DMC Dimethyl carbonate DME Dimethoxyethane DOL Dioxlane DOLDME Dilute ether electrolyte with LiNO ₃ additive EBSD Electron backscatter diffraction EC Ethylene carbonate	CNT	Carbon nanotube
CV Cyclic voltammetry CVD Chemical vapor deposition DEC Diethyl carbonate DFT Density functional theory DMAC Dimethylacetamide DMC Dimethyl carbonate DME Dimethoxyethane DOL Dioxlane DOLDME Dilute ether electrolyte with LiNO ₃ additive EBSD Electron backscatter diffraction EC Ethylene carbonate	cryo-TEM	Cryogenic-transmission electron microscopy
CVD Chemical vapor deposition DEC Diethyl carbonate DFT Density functional theory DMAC Dimethylacetamide DMC Dimethyl carbonate DME Dimethoxyethane DOL Dioxlane DOLDME Dilute ether electrolyte with LiNO ₃ additive EBSD Electron backscatter diffraction EC Ethylene carbonate	c-Si	Crystalline Si
DEC Diethyl carbonate DFT Density functional theory DMAC Dimethylacetamide DMC Dimethyl carbonate DME Dimethoxyethane DOL Dioxlane DOLDME Dilute ether electrolyte with LiNO ₃ additive EBSD Electron backscatter diffraction EC Ethylene carbonate	CV	Cyclic voltammetry
DFT Density functional theory DMAC Dimethylacetamide DMC Dimethyl carbonate DME Dimethoxyethane DOL Dioxlane DOLDME Dilute ether electrolyte with LiNO ₃ additive EBSD Electron backscatter diffraction EC Ethylene carbonate	CVD	Chemical vapor deposition
DMAC Dimethylacetamide DMC Dimethyl carbonate DME Dimethoxyethane DOL Dioxlane DOLDME Dilute ether electrolyte with LiNO ₃ additive EBSD Electron backscatter diffraction EC Ethylene carbonate	DEC	Diethyl carbonate
DMC Dimethyl carbonate DME Dimethoxyethane DOL Dioxlane DOLDME Dilute ether electrolyte with LiNO ₃ additive EBSD Electron backscatter diffraction EC Ethylene carbonate	DFT	Density functional theory
DME Dimethoxyethane DOL Dioxlane DOLDME Dilute ether electrolyte with LiNO ₃ additive EBSD Electron backscatter diffraction EC Ethylene carbonate	DMAC	Dimethylacetamide
DOL Dioxlane DOLDME Dilute ether electrolyte with LiNO ₃ additive EBSD Electron backscatter diffraction EC Ethylene carbonate	DMC	Dimethyl carbonate
DOLDME Dilute ether electrolyte with LiNO ₃ additive EBSD Electron backscatter diffraction EC Ethylene carbonate	DME	Dimethoxyethane
EBSD Electron backscatter diffraction EC Ethylene carbonate	DOL	Dioxlane
EC Ethylene carbonate	DOLDME	Dilute ether electrolyte with LiNO ₃ additive
	EBSD	Electron backscatter diffraction
EDS Energy dispersive spectroscopy	EC	Ethylene carbonate
0/ 1 1/	EDS	Energy dispersive spectroscopy

FCOF Fluorinated covalent organic frameworks

Face-center cubic

FEC Fluoroethylene carbonate FEM Finite element method

F-Free Fluorine-free carbonate electrolyte

FIB Focused-ion beam

FCC

GIWAXS Grazing incidence small-angle X-ray scattering

GO Graphene oxide

HAADF High-angle annular dark-field HCP Hexagonal close-packed HCRG Hard carbon-riveted graphite

HE Hybrid electrolytes

HER Hydrogen evolution reaction

H-Nb₂O₅ Monoclinic Nb₂O₅

ICE Initial Coulombic efficiency IPF Inverse poly figure

KB Ketjen black

LDME Localized high-concentration electrolyte

LPSCl	Li ₆ PS ₅ Cl
LLZO	$\text{Li}_{7}\text{La}_{3}\text{Zr}_{2}\text{O}_{12}$
LIBs	Lithium-ion batteries
LiFSI	Lithium bis(fluorosulfonyl)imide
LMBs	Lithium metal batteries
LSV	Linear sweep voltammetry
LSW	Lifshitz-Slyozov-Wagner
LTO	$\text{Li}_4\text{Ti}_5\text{O}_{12}$
MC	Monte Carlo
MD	Molecular dynamics
MWCNT	Multiwall carbon nanotube
MXenes	Transition metal carbides/nitrides
PG	Propylene glycol
RCD	Relative current density
rGO	Reduced graphene oxide
RIM	Reflection interference microscope
SAED	Selected-area electron diffraction
SEI	Solid-electrolyte interphase
SEM	Scanning electron microscopy
SP	Super P
SSBs	Solid-state batteries
STEM	Scanning transmission electron microscopy
TEM	Transmission electron microscopy
TFSI	Bis(trifluoromethanesulfonyl)imide
TGC	Titration gas chromatography
TMO	Transition metal oxide
TMP	Trimethyl phosphate
$T-Nb_2O_5$	Orthorhombic Nb ₂ O ₅
ToF-SIMS	Time-of-flight secondary ion mass spectrometry
TSE	Ternary-salts electrolyte
TVD	Thermal vapor deposition
VC	Vinylene carbonate
WROs	Wadsley-Roth oxides
XPS	X-ray photoelectron spectroscopy
XRD	X-ray diffraction

REFERENCES

ZIF-8

(1) Cheng, X.; Yang, S.; Cao, B.; Tao, X.; Chen, Z. Single Crystal Perovskite Solar Cells: Development and Perspectives. *Adv. Funct. Mater.* **2020**, *30* (4), 1905021.

Zeolitic imidazolate framework

- (2) Zhang, L.; Dong, J.; Ding, F. Strategies, Status, and Challenges in Wafer Scale Single Crystalline Two-Dimensional Materials Synthesis. *Chem. Rev.* **2021**, *121* (11), 6321–6372.
- (3) Gierschner, J.; Varghese, S.; Park, S. Y. Organic Single Crystal Lasers: A Materials View. *Adv. Opt. Mater.* **2016**, *4* (3), 348–364.
- (4) Sakhatskyi, K.; Turedi, B.; Matt, G. J.; Wu, E.; Sakhatska, A.; Bartosh, V.; Lintangpradipto, M. N.; Naphade, R.; Shorubalko, I.; Mohammed, O. F.; Yakunin, S.; Bakr, O. M.; Kovalenko, M. V. Stable Perovskite Single-Crystal X-Ray Imaging Detectors with Single-Photon Sensitivity. *Nat. Photonics* **2023**, *17* (6), 510–517.
- (5) Bi, Y.; Tao, J.; Wu, Y.; Li, L.; Xu, Y.; Hu, E.; Wu, B.; Hu, J.; Wang, C.; Zhang, J.-G.; Qi, Y.; Xiao, J. Reversible Planar Gliding and Microcracking in a Single-Crystalline Ni-Rich Cathode. *Science* **2020**, 370 (6522), 1313–1317.
- (6) Klein, S.; Bärmann, P.; Fromm, O.; Borzutzki, K.; Reiter, J.; Fan, Q.; Winter, M.; Placke, T.; Kasnatscheew, J. Prospects and Limitations of Single-Crystal Cathode Materials to Overcome Cross-Talk Phenomena in High-Voltage Lithium Ion Cells. *J. Mater. Chem. A* **2021**, *9* (12), 7546–7555.
- (7) Zhu, B.; Ning, Y.; Xu, Z.; Wei, G.; Qu, J. Comparative Study of Polycrystalline and Single-Crystal NCM811 Cathode Materials: The Role of Crystal Defects in Electrochemical Performance. *J. Mater. Chem. A* **2024**, *12* (3), 1671–1684.

- (8) Bai, X.; Xie, F.; Zhang, Z.; Cao, M.; Wang, Q.; Wang, S.; Liu, C.; Su, X.; Lin, Z.; Cui, G. Prospects and Strategies for Single-Crystal NCM Materials to Solve All-Solid-State Battery Cathode Interface Problems. *Adv. Energy Mater.* **2024**, *14* (34), 2401336.
- (9) Zhao, X.; Cao, X.; Sheng, C.; Xu, L.; Wu, P.; Zhou, Y.; He, P.; Tang, Y.; Zhou, H. Perspective on High-Stability Single-Crystal Li-Rich Cathode Materials for Li-Ion Batteries. *ACS Appl. Mater. Interfaces* **2024**, *16* (19), 24147–24161.
- (10) Hosono, E.; Kudo, T.; Honma, I.; Matsuda, H.; Zhou, H. Synthesis of Single Crystalline Spinel $LiMn_2O_4$ Nanowires for a Lithium Ion Battery with High Power Density. *Nano Lett.* **2009**, 9 (3), 1045-1051.
- (11) Ma, X.; Zhang, M.; Liang, C.; Li, Y.; Wu, J.; Che, R. Inheritance of Crystallographic Orientation during Lithiation/Delithiation Processes of Single-Crystal α -Fe₂O₃ Nanocubes in Lithium-Ion Batteries. *ACS Appl. Mater. Interfaces* **2015**, 7 (43), 24191–24196.
- (12) Zhao, Y.; Peng, L.; Liu, B.; Yu, G. Single-Crystalline LiFePO₄ Nanosheets for High-Rate Li-Ion Batteries. *Nano Lett.* **2014**, *14* (5), 2849–2853.
- (13) Chan, C. K.; Peng, H.; Liu, G.; McIlwrath, K.; Zhang, X. F.; Huggins, R. A.; Cui, Y. High-Performance Lithium Battery Anodes Using Silicon Nanowires. *Nat. Nanotechnol.* **2008**, 3 (1), 31–35.
- (14) Tarascon, J.-M.; Armand, M. Issues and Challenges Facing Rechargeable Lithium Batteries. *Nature* **2001**, *414* (6861), 359–367.
- (15) Cheng, X.-B.; Zhang, R.; Zhao, C.-Z.; Zhang, Q. Toward Safe Lithium Metal Anode in Rechargeable Batteries: A Review. *Chem. Rev.* **2017**, *117* (15), 10403–10473.
- (16) Lin, D.; Liu, Y.; Cui, Y. Reviving the Lithium Metal Anode for High-Energy Batteries. *Nat. Nanotechnol.* **2017**, *12* (3), 194–206.
- (17) Wang, F.; Borodin, O.; Gao, T.; Fan, X.; Sun, W.; Han, F.; Faraone, A.; Dura, J. A.; Xu, K.; Wang, C. Highly Reversible Zinc Metal Anode for Aqueous Batteries. *Nat. Mater.* **2018**, *17* (6), 543–549.
- (18) Yang, Q.; Li, Q.; Liu, Z.; Wang, D.; Guo, Y.; Li, X.; Tang, Y.; Li, H.; Dong, B.; Zhi, C. Dendrites in Zn-Based Batteries. *Adv. Mater.* **2020**, 32 (48), No. e2001854.
- (19) Li, C.; Jin, S.; Archer, L. A.; Nazar, L. F. Toward Practical Aqueous Zinc-Ion Batteries for Electrochemical Energy Storage. *Joule* **2022**, *6* (8), 1733–1738.
- (20) Lee, B.; Paek, E.; Mitlin, D.; Lee, S. W. Sodium Metal Anodes: Emerging Solutions to Dendrite Growth. *Chem. Rev.* **2019**, *119* (8), 5416–5460.
- (21) He, J.; Bhargav, A.; Su, L.; Lamb, J.; Okasinski, J.; Shin, W.; Manthiram, A. Tuning the Solvation Structure with Salts for Stable Sodium-Metal Batteries. *Nat. Energy* **2024**, *9* (4), 446–456.
- (22) Xu, C.; Diemant, T.; Liu, X.; Passerini, S. Locally Concentrated Deep Eutectic Liquids Electrolytes for Low-Polarization Aluminum Metal Batteries. *Adv. Mater.* **2024**, *36* (24), No. e2400263.
- (23) Zhao, Z.; Zhang, Z.; Xu, T.; Wang, W.; Wang, B.; Yu, X. Solvation Structure Regulation for Highly Reversible Aqueous Al Metal Batteries. *J. Am. Chem. Soc.* **2024**, *146* (3), 2257–2266.
- (24) Long, J.; Liu, Y.; He, Z.; Tan, S.; Xiong, F.; Xu, H.; Wang, W.; Zhang, G.; Yang, Z.; An, Q. Redesigning Solvation Structure toward Passivation-Free Magnesium Metal Batteries. *ACS Nano* **2024**, *18* (23), 15239–15248.
- (25) Bi, J.; Liu, Y.; Du, Z.; Wang, K.; Guan, W.; Wu, H.; Ai, W.; Huang, W. Bottom-Up Magnesium Deposition Induced by Paper-Based Triple-Gradient Scaffolds toward Flexible Magnesium Metal Batteries. *Adv. Mater.* **2024**, *36* (9), No. e2309339.
- (26) Liu, J.; Bao, Z.; Cui, Y.; Dufek, E. J.; Goodenough, J. B.; Khalifah, P.; Li, Q.; Liaw, B. Y.; Liu, P.; Manthiram, A.; Meng, Y. S.; Subramanian, V. R.; Toney, M. F.; Viswanathan, V. V.; Whittingham, M. S.; Xiao, J.; Xu, W.; Yang, J.; Yang, X.-Q.; Zhang, J.-G. Pathways for Practical High-Energy Long-Cycling Lithium Metal Batteries. *Nat. Energy* **2019**, *4* (3), 180–186.
- (27) Zhang, J.-G.; Xu, W.; Xiao, J.; Cao, X.; Liu, J. Lithium Metal Anodes with Nonaqueous Electrolytes. *Chem. Rev.* **2020**, *120* (24), 13312–13348.
- (28) Chen, X.; Yao, Y.; Yan, C.; Zhang, R.; Cheng, X.; Zhang, Q. A Diffusion-Reaction Competition Mechanism to Tailor Lithium

- Deposition for Lithium-Metal Batteries. Angew. Chem., Int. Ed. 2020, 59 (20), 7743-7747.
- (29) Chen, H.; Zhao, Y.; Zhang, X.; Li, R.; Wang, A.; Zhang, H.; Liu, J.; Wen, B.; Zhang, L.; Hua, Q.; Liu, T.; Wu, K.; Amine, K.; Luo, J. Synthesis of Monocrystalline Lithium for High-Critical-Current-Density Solid-State Batteries. *Nat. Synth.* **2025**, *4*, 552.
- (30) Xiao, X.; Greenburg, L. C.; Li, Y.; Yang, M.; Tzeng, Y.-K.; Sui, C.; Peng, Y.; Wu, Y.; Zhang, Z.; Gao, X.; Xu, R.; Ye, Y.; Zhang, P.; Yang, Y.; Vailionis, A.; Hsu, P.; Qin, J.; Cui, Y. Epitaxial Electrodeposition of Zinc on Different Single Crystal Copper Substrates for High Performance Aqueous Batteries. *Nano Lett.* **2025**, 25 (4), 1305–1313.
- (31) Sun, Z.; Wang, Y.; Shen, S.; Li, X.; Hu, X.; Hu, M.; Su, Y.; Ding, S.; Xiao, C. Directing (110) Oriented Lithium Deposition through High-flux Solid Electrolyte Interphase for Dendrite-free Lithium Metal Batteries. *Angew. Chem., Int. Ed.* **2023**, *62* (41), No. e202309622.
- (32) Zhang, X.; Li, J.; Liu, Y.; Lu, B.; Liang, S.; Zhou, J. Single [0001]-Oriented Zinc Metal Anode Enables Sustainable Zinc Batteries. *Nat. Commun.* **2024**, *15* (1), 2735.
- (33) Becker, R.; Döring, W. Kinetische Behandlung Der Keimbildung in Übersättigten Dämpfen. Ann. Phys. 1935, 416 (8), 719–752.
- (34) Volmer, M.; Weber, A. Keimbildung in Übersättigten Gebilden. *Z. für Phys. Chem.* **1926**, *119U* (1), 277–301.
- (35) Frenkel, J. A General Theory of Heterophase Fluctuations and Pretransition Phenomena. J. Chem. Phys. 1939, 7 (7), 538-547.
- (36) Karthika, S.; Radhakrishnan, T. K.; Kalaichelvi, P. A Review of Classical and Nonclassical Nucleation Theories. *Cryst. Growth Des.* **2016**, *16* (11), 6663–6681.
- (37) Anderson, P. Assessment and Development of Executive Function (EF) During Childhood. *Child Neuropsychol.* **2002**, 8 (2), 71–82.
- (38) Wu, D. T. Nucleation Theory. Solid State Phys. 1996, 50, 37-187.
- (39) Scharifker, B.; Hills, G. Theoretical and Experimental Studies of Multiple Nucleation. *Electrochim. Acta* **1983**, 28 (7), 879–889.
- (40) Thirumalraj, B.; Hagos, T. T.; Huang, C.-J.; Teshager, M. A.; Cheng, J.-H.; Su, W.-N.; Hwang, B.-J. Nucleation and Growth Mechanism of Lithium Metal Electroplating. *J. Am. Chem. Soc.* **2019**, *141* (46), 18612–18623.
- (41) Cooper, E. R.; Li, M.; Gentle, I.; Xia, Q.; Knibbe, R. A Deeper Understanding of Metal Nucleation and Growth in Rechargeable Metal Batteries Through Theory and Experiment. *Angew. Chem., Int. Ed.* **2023**, *62* (51), No. e202309247.
- (42) Talapin, D. V.; Rogach, A. L.; Haase, M.; Weller, H. Evolution of an Ensemble of Nanoparticles in a Colloidal Solution: Theoretical Study. *J. Phys. Chem. B* **2001**, *105* (49), 12278–12285.
- (43) Kwon, S. G.; Hyeon, T. Formation Mechanisms of Uniform Nanocrystals via Hot-Injection and Heat-Up Methods. *Small* **2011**, 7 (19), 2685–2702.
- (44) Bai, P.; Li, J.; Brushett, F. R.; Bazant, M. Z. Transition of Lithium Growth Mechanisms in Liquid Electrolytes. *Energy Environ. Sci.* **2016**, 9 (10), 3221–3229.
- (45) Peng, X.; Manna, L.; Yang, W.; Wickham, J.; Scher, E.; Kadavanich, A.; Alivisatos, A. P. Shape Control of CdSe Nanocrystals. *Nature* **2000**, 404 (6773), 59–61.
- (46) Casalini, S.; Bortolotti, C. A.; Leonardi, F.; Biscarini, F. Self-Assembled Monolayers in Organic Electronics. *Chem. Soc. Rev.* **2017**, 46 (1), 40–71.
- (47) Ostwald, W. Über Die Vermeintliche Isomerie Des Roten Und Gelben Quecksilberoxyds Und Die Oberflächenspannung Fester Körper. *Z. für Phys. Chem.* **1900**, 34*U* (1), 495–503.
- (48) Lifshitz, I. M.; Slyozov, V. V. The Kinetics of Precipitation from Supersaturated Solid Solutions. *J. Phys. Chem. Solids* **1961**, *19* (1–2), 35–50.
- (49) Kahlweit, M. Ostwald Ripening of Precipitates. Adv. Colloid Interface Sci. 1975, 5 (1), 1–35.
- (50) Ely, D. R.; García, R. E. Heterogeneous Nucleation and Growth of Lithium Electrodeposits on Negative Electrodes. *J. Electrochem. Soc.* **2013**, *160* (4), A662–A668.

- (51) Yan, K.; Lu, Z.; Lee, H.-W.; Xiong, F.; Hsu, P.-C.; Li, Y.; Zhao, J.; Chu, S.; Cui, Y. Selective Deposition and Stable Encapsulation of Lithium through Heterogeneous Seeded Growth. *Nat. Energy* **2016**, *1* (3), 16010.
- (52) Wang, D.; Liu, H.; Liu, F.; Ma, G.; Yang, J.; Gu, X.; Zhou, M.; Chen, Z. Phase-Separation-Induced Porous Lithiophilic Polymer Coating for High-Efficiency Lithium Metal Batteries. *Nano Lett.* **2021**, *21* (11), 4757–4764.
- (53) Yin, Q.; Liu, Q.; Liu, Y.; Qu, Z.; Sun, F.; Wang, C.; Yuan, X.; Li, Y.; Shen, L.; Zhang, C.; Lu, Y. General Fabrication of Robust Alloyed Metal Anodes for High-Performance Metal Batteries. *Adv. Mater.* **2024**, 36 (30), No. e2404689.
- (54) Geng, L.; Liu, Q.; Chen, J.; Jia, P.; Ye, H.; Yan, J.; Zhang, L.; Tang, Y.; Huang, J. In Situ Observation of Electrochemical Ostwald Ripening during Sodium Deposition. *Nano Res.* **2022**, *15* (3), 2650–2654.
- (55) Kalidindi, S. B.; Jagirdar, B. R. Synthesis of Cu@ZnO Core-Shell Nanocomposite through Digestive Ripening of Cu and Zn Nanoparticles. *J. Phys. Chem. C* **2008**, *112* (11), 4042–4048.
- (56) Kalidindi, S. B.; Jagirdar, B. R. Highly Monodisperse Colloidal Magnesium Nanoparticles by Room Temperature Digestive Ripening. *Inorg. Chem.* **2009**, *48* (10), 4524–4529.
- (57) Wang, C.; Wang, H.; Tao, L.; Wang, X.; Cao, P.; Lin, F.; Xin, H. L. Direct Observation of Nucleation and Growth Behaviors of Lithium by In Situ Electron Microscopy. *ACS Energy Lett.* **2023**, *8* (4), 1929–1935
- (58) Zheng, H.; Smith, R. K.; Jun, Y.; Kisielowski, C.; Dahmen, U.; Alivisatos, A. P. Observation of Single Colloidal Platinum Nanocrystal Growth Trajectories. *Science* **2009**, 324 (5932), 1309–1312.
- (59) An, B.; Li, J.; Li, Z.; Li, R. The Mechanism of Aluminum Deposition and Dendrite Growth on a Copper Substrate in Anode-Free Aluminum Batteries. *ACS Appl. Mater. Interfaces* **2024**, *16* (46), 63553–63559.
- (60) Kim, M.-H.; Kim, D. Y.; Li, Y.; Kim, J.; Kim, M. H.; Seo, J.; Cunning, B. V.; Kim, T.; Park, S.-W.; Ruoff, R. S.; Seo, D.-H.; Jin, S.; Lee, H.-W. Horizontal Lithium Growth Driven by Surface Dynamics on Single Crystal Cu(111) Foil. *Energy Environ. Sci.* **2024**, *17* (18), 6521–6532.
- (61) Yang, G.; Li, Y.; Zhang, C.; Wang, J.; Bai, Y.; Lim, C. Y. J.; Ng, M.-F.; Chang, Z.; Kumar, S.; Sofer, Z.; Liu, W.; Seh, Z. W. In Situ Formed Magnesiophilic Sites Guiding Uniform Deposition for Stable Magnesium Metal Anodes. *Nano Lett.* **2022**, 22 (22), 9138–9146.
- (62) Hao, B.; Zhou, J.; Yang, H.; Zhu, C.; Wang, Z.; Liu, J.; Yan, C.; Qian, T. Concentration Polarization Induced Phase Rigidification in Ultralow Salt Colloid Chemistry to Stabilize Cryogenic Zn Batteries. *Nat. Commun.* **2024**, *15* (1), 9465.
- (63) Monroe, C.; Newman, J. Dendrite Growth in Lithium/Polymer Systems: A Propagation Model for Liquid Electrolytes under Galvanostatic Conditions. *J. Electrochem. Soc.* **2003**, *150* (10), A1377—A1384.
- (64) Pei, A.; Zheng, G.; Shi, F.; Li, Y.; Cui, Y. Nanoscale Nucleation and Growth of Electrodeposited Lithium Metal. *Nano Lett.* **2017**, *17* (2), 1132–1139.
- (65) Wang, J.; Huang, W.; Pei, A.; Li, Y.; Shi, F.; Yu, X.; Cui, Y. Improving Cyclability of Li Metal Batteries at Elevated Temperatures and Its Origin Revealed by Cryo-Electron Microscopy. *Nat. Energy* **2019**, *4* (8), 664–670.
- (66) Frank, F. C.; Merwe, J. H. V. D. One-Dimensional Dislocations. II. Misfitting Monolayers and Oriented Overgrowth. *Proc. R. Soc. London Ser. A Math. Phys. Sci.* 1949, 198 (1053), 216–225.
- (67) Meier, G. H. Interphaseinterfaces. In *Thermodynamics of Surfaces and Interfaces*; Cambridge University Press, 2014; pp 128–147.
- (68) Porter, D. A.; Easterling, K. E.; Easterling, K. E. Phase Transformations in Metals and Alloys (Revised Reprint); CRC Press, 2019. DOI: 10.1201/9781439883570
- (69) Akolkar, R. Modeling Dendrite Growth during Lithium Electrodeposition at Sub-Ambient Temperature. *J. Power Sources* **2014**, 246, 84–89.

- (70) Su, J.; Yin, X.; Zhao, H.; Yang, H.; Yang, D.; He, L.; Wang, M.; Jin, S.; Zhao, K.; Wang, Y.; Wei, Y. Temperature-Dependent Nucleation and Electrochemical Performance of Zn Metal Anodes. *Nano Lett.* **2022**, 22 (4), 1549–1556.
- (71) Yan, K.; Wang, J.; Zhao, S.; Zhou, D.; Sun, B.; Cui, Y.; Wang, G. Temperature-Dependent Nucleation and Growth of Dendrite-Free Lithium Metal Anodes. *Angew. Chem., Int. Ed.* **2019**, *58* (33), 11364–11368.
- (72) Guo, Y.; Li, D.; Xiong, R.; Li, H. Investigation of the Temperature-Dependent Behaviours of Li Metal Anode. *Chem. Commun.* **2019**, *55* (66), 9773–9776.
- (73) Thenuwara, A. C.; Shetty, P. P.; McDowell, M. T. Distinct Nanoscale Interphases and Morphology of Lithium Metal Electrodes Operating at Low Temperatures. *Nano Lett.* **2019**, 19 (12), 8664–
- (74) Fang, C.; Lu, B.; Pawar, G.; Zhang, M.; Cheng, D.; Chen, S.; Ceja, M.; Doux, J.-M.; Musrock, H.; Cai, M.; Liaw, B.; Meng, Y. S. Pressure-Tailored Lithium Deposition and Dissolution in Lithium Metal Batteries. *Nat. Energy* **2021**, *6* (10), 987–994.
- (75) Louli, A. J.; Eldesoky, A.; Weber, R.; Genovese, M.; Coon, M.; deGooyer, J.; Deng, Z.; White, R. T.; Lee, J.; Rodgers, T.; Petibon, R.; Hy, S.; Cheng, S. J. H.; Dahn, J. R. Diagnosing and Correcting Anode-Free Cell Failure via Electrolyte and Morphological Analysis. *Nat. Energy* **2020**, *5* (9), 693–702.
- (76) Zhang, X.; Wang, Q. J.; Harrison, K. L.; Jungjohann, K.; Boyce, B. L.; Roberts, S. A.; Attia, P. M.; Harris, S. J. Rethinking How External Pressure Can Suppress Dendrites in Lithium Metal Batteries. *J. Electrochem. Soc.* **2019**, *166* (15), A3639–A3652.
- (77) Shen, X.; Zhang, R.; Shi, P.; Chen, X.; Zhang, Q. How Does External Pressure Shape Li Dendrites in Li Metal Batteries? *Adv. Energy Mater.* **2021**, *11* (10), 2003416.
- (78) Biswal, P.; Stalin, S.; Kludze, A.; Choudhury, S.; Archer, L. A. Nucleation and Early Stage Growth of Li Electrodeposits. *Nano Lett.* **2019**, *19* (11), 8191–8200.
- (79) Dong, K.; Xu, Y.; Tan, J.; Osenberg, M.; Sun, F.; Kochovski, Z.; Pham, D. T.; Mei, S.; Hilger, A.; Ryan, E.; Lu, Y.; Banhart, J.; Manke, I. Unravelling the Mechanism of Lithium Nucleation and Growth and the Interaction with the Solid Electrolyte Interface. *ACS Energy Lett.* **2021**, *6* (5), 1719–1728.
- (80) Nagy, K. S.; Kazemiabnavi, S.; Thornton, K.; Siegel, D. J. Thermodynamic Overpotentials and Nucleation Rates for Electrodeposition on Metal Anodes. *ACS Appl. Mater. Interfaces* **2019**, *11* (8), 7954–7964.
- (81) Feng, G.; Shi, Y.; Jia, H.; Risal, S.; Yang, X.; Ruchhoeft, P.; Shih, W.-C.; Fan, Z.; Xu, W.; Shan, X. Progressive and Instantaneous Nature of Lithium Nucleation Discovered by Dynamic and Operando Imaging. *Sci. Adv.* **2023**, *9* (21), No. eadg6813.
- (82) Jo, S.; Kwon, B.; Oh, J.; Lee, J.; Park, K.; Lee, K. T. The Roles of Nucleation and Growth Kinetics in Determining Li Metal Morphology for Li Metal Batteries: Columnar versus Spherical Growth. *J. Mater. Chem. A* **2022**, *10* (10), 5520–5529.
- (83) Zou, P.; Sui, Y.; Zhan, H.; Wang, C.; Xin, H. L.; Cheng, H.-M.; Kang, F.; Yang, C. Polymorph Evolution Mechanisms and Regulation Strategies of Lithium Metal Anode under Multiphysical Fields. *Chem. Rev.* **2021**, *121* (10), 5986–6056.
- (84) Ding, F.; Xu, W.; Graff, G. L.; Zhang, J.; Sushko, M. L.; Chen, X.; Shao, Y.; Engelhard, M. H.; Nie, Z.; Xiao, J.; Liu, X.; Sushko, P. V.; Liu, J.; Zhang, J.-G. Dendrite-Free Lithium Deposition via Self-Healing Electrostatic Shield Mechanism. *J. Am. Chem. Soc.* **2013**, *135* (11), 4450–4456.
- (85) Xiong, S.; Xie, K.; Diao, Y.; Hong, X. Properties of Surface Film on Lithium Anode with LiNO $_3$ as Lithium Salt in Electrolyte Solution for Lithium-Sulfur Batteries. *Electrochim. Acta* **2012**, 83, 78–86.
- (86) Li, W.; Yao, H.; Yan, K.; Zheng, G.; Liang, Z.; Chiang, Y.-M.; Cui, Y. The Synergetic Effect of Lithium Polysulfide and Lithium Nitrate to Prevent Lithium Dendrite Growth. *Nat. Commun.* **2015**, *6* (1), 7436.
- (87) Kim, M. S.; Ryu, J.-H.; Deepika; Lim, Y. R.; Nah, I. W.; Lee, K.-R.; Archer, L. A.; Cho, W. I. Langmuir-Blodgett Artificial Solid-

- Electrolyte Interphases for Practical Lithium Metal Batteries. *Nat. Energy* **2018**, 3 (10), 889–898.
- (88) Zheng, G.; Lee, S. W.; Liang, Z.; Lee, H.-W.; Yan, K.; Yao, H.; Wang, H.; Li, W.; Chu, S.; Cui, Y. Interconnected Hollow Carbon Nanospheres for Stable Lithium Metal Anodes. *Nat. Nanotechnol.* **2014**, 9 (8), 618–623.
- (89) Huang, Z.; Lai, J.-C.; Liao, S.-L.; Yu, Z.; Chen, Y.; Yu, W.; Gong, H.; Gao, X.; Yang, Y.; Qin, J.; Cui, Y.; Bao, Z. A Salt-Philic, Solvent-Phobic Interfacial Coating Design for Lithium Metal Electrodes. *Nat. Energy* **2023**, *8* (6), 577–585.
- (90) Yang, C.-P.; Yin, Y.-X.; Zhang, S.-F.; Li, N.-W.; Guo, Y.-G. Accommodating Lithium into 3D Current Collectors with a Submicron Skeleton towards Long-Life Lithium Metal Anodes. *Nat. Commun.* **2015**, *6* (1), 8058.
- (91) Zhao, H.; Lei, D.; He, Y.; Yuan, Y.; Yun, Q.; Ni, B.; Lv, W.; Li, B.; Yang, Q.; Kang, F.; Lu, J. Compact 3D Copper with Uniform Porous Structure Derived by Electrochemical Dealloying as Dendrite-Free Lithium Metal Anode Current Collector. *Adv. Energy Mater.* **2018**, 8 (19), 1800266.
- (92) Li, Y.; Li, Y.; Pei, A.; Yan, K.; Sun, Y.; Wu, C.-L.; Joubert, L.-M.; Chin, R.; Koh, A. L.; Yu, Y.; Perrino, J.; Butz, B.; Chu, S.; Cui, Y. Atomic Structure of Sensitive Battery Materials and Interfaces Revealed by Cryo-Electron Microscopy. *Science* **2017**, *358* (6362), 506–510.
- (93) Zhao, Q.; Deng, Y.; Utomo, N. W.; Zheng, J.; Biswal, P.; Yin, J.; Archer, L. A. On the Crystallography and Reversibility of Lithium Electrodeposits at Ultrahigh Capacity. *Nat. Commun.* **2021**, *12* (1), 6034.
- (94) Hu, X.; Gao, Y.; Zhang, B.; Shi, L.; Li, Q. Superior Cycle Performance of Li Metal Electrode with {110} Surface Texturing. *EcoMat* **2022**, *4* (6), No. e12264.
- (95) Hu, X.; Gao, Y.; Sun, Y.; Hou, Z.; Luo, Y.; Wang, D.; Wang, J.; Zhang, B.; Zheng, Z.; Li, Q. Preserving the Li {110} Texture to Achieve Long Cycle Life in Li Metal Electrode at High Rates. *Adv. Funct. Mater.* **2024**, *34* (11), 2307404.
- (96) Baek, M.; Kim, J.; Jeong, K.; Yang, S.; Kim, H.; Lee, J.; Kim, M.; Kim, K. J.; Choi, J. W. Naked Metallic Skin for Homo-Epitaxial Deposition in Lithium Metal Batteries. *Nat. Commun.* **2023**, *14* (1), 1296.
- (97) Rospars, N.; Srout, M.; Fu, C.; Mourouga, G.; Mensi, M.; Ingenito, A. High Performance Ultra-Thin Lithium Metal Anode Enabled by Vacuum Thermal Evaporation. *Commun. Mater.* **2024**, *5* (1), 179.
- (98) Sun, Z.; Wang, Y.; Shen, S.; Li, X.; Hu, X.; Hu, M.; Su, Y.; Ding, S.; Xiao, C. Directing (110) Oriented Lithium Deposition through High-flux Solid Electrolyte Interphase for Dendrite-free Lithium Metal Batteries. *Angew. Chem.* **2023**, *135* (41), No. e202309622.
- (99) Jin, S.; Ye, Y.; Niu, Y.; Xu, Y.; Jin, H.; Wang, J.; Sun, Z.; Cao, A.; Wu, X.; Luo, Y.; Ji, H.; Wan, L.-J. Solid-Solution-Based Metal Alloy Phase for Highly Reversible Lithium Metal Anode. *J. Am. Chem. Soc.* **2020**, *142* (19), 8818–8826.
- (100) Yang, C.; Yao, Y.; He, S.; Xie, H.; Hitz, E.; Hu, L. Ultrafine Silver Nanoparticles for Seeded Lithium Deposition toward Stable Lithium Metal Anode. *Adv. Mater.* **2017**, *29* (38), 1702714.
- (101) Fang, Y.; Zhang, S. L.; Wu, Z.-P.; Luan, D.; Lou, X. W. (David). A Highly Stable Lithium Metal Anode Enabled by Ag Nanoparticle-Embedded Nitrogen-Doped Carbon Macroporous Fibers. *Sci. Adv.* **2021**, *7* (21), No. eabg3626.
- (102) Zhang, H.; Liao, X.; Guan, Y.; Xiang, Y.; Li, M.; Zhang, W.; Zhu, X.; Ming, H.; Lu, L.; Qiu, J.; Huang, Y.; Cao, G.; Yang, Y.; Mai, L.; Zhao, Y.; Zhang, H. Lithiophilic-Lithiophobic Gradient Interfacial Layer for a Highly Stable Lithium Metal Anode. *Nat. Commun.* **2018**, *9* (1), 3729. (103) Zhang, N.; Yu, S.-H.; Abruña, H. D. Regulating Lithium
- Nucleation and Growth by Zinc Modified Current Collectors. *Nano Res.* **2020**, *13* (1), 45–51.
- (104) Zhao, J.; Zhou, G.; Yan, K.; Xie, J.; Li, Y.; Liao, L.; Jin, Y.; Liu, K.; Hsu, P.-C.; Wang, J.; Cheng, H.-M.; Cui, Y. Air-Stable and Freestanding Lithium Alloy/Graphene Foil as an Alternative to Lithium Metal Anodes. *Nat. Nanotechnol.* **2017**, *12* (10), 993–999.

- (105) Park, J. B.; Choi, C.; Yu, S.; Chung, K. Y.; Kim, D. Porous Lithiophilic Li-Si Alloy-Type Interfacial Framework via Self-Discharge Mechanism for Stable Lithium Metal Anode with Superior Rate. *Adv. Energy Mater.* **2021**, *11* (37), 2101544.
- (106) Liang, Z.; Lin, D.; Zhao, J.; Lu, Z.; Liu, Y.; Liu, C.; Lu, Y.; Wang, H.; Yan, K.; Tao, X.; Cui, Y. Composite Lithium Metal Anode by Melt Infusion of Lithium into a 3D Conducting Scaffold with Lithiophilic Coating. *Proc. Natl. Acad. Sci. U. S. A.* **2016**, *113* (11), 2862–2867.
- (107) Wan, M.; Kang, S.; Wang, L.; Lee, H.-W.; Zheng, G. W.; Cui, Y.; Sun, Y. Mechanical Rolling Formation of Interpenetrated Lithium Metal/Lithium Tin Alloy Foil for Ultrahigh-Rate Battery Anode. *Nat. Commun.* **2020**, *11* (1), 829.
- (108) Røe, I. T.; Selbach, S. M.; Schnell, S. K. Crystal Structure Influences Migration along Li and Mg Surfaces. J. Phys. Chem. Lett. 2020, 11 (8), 2891–2895.
- (109) Gao, P.; Wu, H.; Zhang, X.; Jia, H.; Kim, J.; Engelhard, M. H.; Niu, C.; Xu, Z.; Zhang, J.; Xu, W. Optimization of Magnesium-Doped Lithium Metal Anode for High Performance Lithium Metal Batteries through Modeling and Experiment. *Angew. Chem., Int. Ed.* **2021**, *60* (30), 16506–16513.
- (110) Nan, W.; Yan, S.; Zhang, C.; Peng, S.; Li, X.; Dai, S. Realizing Stable Lithium Metal Anode with Surface-Preferred Crystal Plane through Mg Doping. *J. Energy Storage* **2024**, *100*, 113559.
- (111) Zhang, L.; Xu, D.; Chen, H.; Li, R.; Hu, Z.; Wen, B.; Chen, A.; Liu, X.; Luo, J.; Wang, A. Single-Crystalline LiMg Alloy Anode for Deep Cycling All Solid State Lithium Metal Batteries. *Adv. Funct. Mater.* **2025**, 35 (9), 2416013.
- (112) Cao, J.; Shi, Y.; Gao, A.; Du, G.; Dilxat, M.; Zhang, Y.; Cai, M.; Qian, G.; Lu, X.; Xie, F.; Sun, Y.; Lu, X. Hierarchical Li Electrochemistry Using Alloy-Type Anode for High-Energy-Density Li Metal Batteries. *Nat. Commun.* **2024**, *15* (1), 1354.
- (113) Hu, Y.; Li, H.; Chen, Z.; Cen, W.; Wang, Q.; Chen, Y.; Davoodi, A.; Liu, W. Li-Alloy Texture Creates in-Built Li(110) Epitaxy in a Thin Li-Metal Anode Allowing High Depth-of-Discharge Cycling in Carbonate Electrolyte. *Chem. Eng. J.* **2023**, *466*, 143084.
- (114) Wang, A.; Huang, S.; Xie, Z.; Liao, J.; Li, W.; Chen, Y.; Li, H.; Wang, Z.; Wu, Z.; Chen, L. In₃Li₁₃(311)/Li(110) Coherent Heterogeneous Induced Uniform Epitaxial Electrodeposition Enabling the Stable Ultrathin Lithium Metal Anode. *Acta Mater.* **2025**, 287, 120780.
- (115) Niu, C.; Liu, D.; Lochala, J. A.; Anderson, C. S.; Cao, X.; Gross, M. E.; Xu, W.; Zhang, J.-G.; Whittingham, M. S.; Xiao, J.; Liu, J. Balancing Interfacial Reactions to Achieve Long Cycle Life in High-Energy Lithium Metal Batteries. *Nat. Energy* **2021**, *6* (7), 723–732.
- (116) Weber, R.; Genovese, M.; Louli, A. J.; Hames, S.; Martin, C.; Hill, I. G.; Dahn, J. R. Long Cycle Life and Dendrite-Free Lithium Morphology in Anode-Free Lithium Pouch Cells Enabled by a Dual-Salt Liquid Electrolyte. *Nat. Energy* **2019**, *4* (8), 683–689.
- (117) Ishikawa, K.; Ito, Y.; Harada, S.; Tagawa, M.; Ujihara, T. Crystal Orientation Dependence of Precipitate Structure of Electrodeposited Li Metal on Cu Current Collectors. *Cryst. Growth Des.* **2017**, *17* (5), 2379–2385.
- (118) Gu, Y.; Xu, H.; Zhang, X.; Wang, W.; He, J.; Tang, S.; Yan, J.; Wu, D.; Zheng, M.; Dong, Q.; Mao, B. Lithiophilic Faceted Cu(100) Surfaces: High Utilization of Host Surface and Cavities for Lithium Metal Anodes. *Angew. Chem., Int. Ed.* **2019**, 58 (10), 3092–3096.
- (119) Shen, C.; Gu, J.; Li, N.; Peng, Z.; Xie, K. Single Crystal Cu (110) Inducing Lateral Growth of Electrodeposition Li for Dendrite-Free Li Metal-Based Batteries. *J. Power Sources* **2021**, *501*, 229969.
- (120) Kim, Y.-J.; Kwon, S. H.; Noh, H.; Yuk, S.; Lee, H.; Jin, H. s.; Lee, J.; Zhang, J.-G.; Lee, S. G.; Guim, H.; Kim, H.-T. Facet Selectivity of Cu Current Collector for Li Electrodeposition. *Energy Storage Mater.* **2019**, 19, 154–162.
- (121) Lai, G.; Jiao, J.; Fang, C.; Jiang, Y.; Sheng, L.; Xu, B.; Ouyang, C.; Zheng, J. The Mechanism of Li Deposition on the Cu Substrates in the Anode-Free Li Metal Batteries. *Small* **2023**, *19* (3), No. e2205416. (122) Ishikawa, K.; Harada, S.; Tagawa, M.; Ujihara, T. Effect of Crystal Orientation of Cu Current Collectors on Cycling Stability of Li Metal Anodes. *ACS Appl. Mater. Interfaces* **2020**, *12* (8), 9341–9346.

- (123) Hao, Z.; Li, G.; Zheng, C.; Liu, X.; Wu, S.; Li, H.; Zhang, K.; Yan, Z.; Chen, J. The Dependence of Solid Electrolyte Interphase on the Crystal Facet of Current Collector in Li Metal Battery. *Angew. Chem., Int. Ed.* **2024**, *63* (37), No. e202407064.
- (124) Zhan, J.; Deng, L.; Liu, Y.; Hao, M.; Wang, Z.; Dong, L.; Yang, Y.; Song, K.; Qi, D.; Wang, J.; Wang, S.; Liu, H.; Zhou, W.; Chen, H. Self-Selective (220) Directional Grown Copper Current Collector Design for Cycling-Stable Anode-Less Lithium Metal Batteries. *Adv. Mater.* **2025**, *37* (5), No. e2413420.
- (125) Li, N.; Zhang, K.; Xie, K.; Wei, W.; Gao, Y.; Bai, M.; Gao, Y.; Hou, Q.; Shen, C.; Xia, Z.; Wei, B. Reduced-Graphene-Oxide-Guided Directional Growth of Planar Lithium Layers. *Adv. Mater.* **2020**, 32 (7), No. e1907079.
- (126) Wu, Z.; Wang, C.; Hui, Z.; Liu, H.; Wang, S.; Yu, S.; Xing, X.; Holoubek, J.; Miao, Q.; Xin, H. L.; Liu, P. Growing Single-Crystalline Seeds on Lithiophobic Substrates to Enable Fast-Charging Lithium-Metal Batteries. *Nat. Energy* **2023**, *8* (4), 340–350.
- (127) Zhang, Y.; Zhao, P.; Nie, Q.; Li, Y.; Guo, R.; Hong, Y.; Deng, J.; Song, J. Enabling 420 Wh kg⁻¹ Stable Lithium-Metal Pouch Cells by Lanthanum Doping. *Adv. Mater.* **2023**, *35* (15), 2211032.
- (128) Yu, S.; Yu, X.; Shivakumar, S.; Wang, S.; Qiu, E.; Miao, Q.; Gao, J.; Wei, M.; Zhou, J.; Chen, Z.; Liu, P. Defect-Mediated Faceted Lithium Nucleation on Carbon Composite Substrates. *ACS Nano* **2024**, *18* (26), 17031–17040.
- (129) Yuan, X.; Liu, B.; Mecklenburg, M.; Li, Y. Ultrafast Deposition of Faceted Lithium Polyhedra by Outpacing SEI Formation. *Nature* **2023**, 620 (7972), 86–91.
- (130) Boyle, D. T.; Li, Y.; Pei, A.; Vilá, R. A.; Zhang, Z.; Sayavong, P.; Kim, M. S.; Huang, W.; Wang, H.; Liu, Y.; Xu, R.; Sinclair, R.; Qin, J.; Bao, Z.; Cui, Y. Resolving Current-Dependent Regimes of Electroplating Mechanisms for Fast Charging Lithium Metal Anodes. *Nano Lett.* 2022, 22 (20), 8224–8232.
- (131) Holoubek, J.; Kim, K.; Yin, Y.; Wu, Z.; Liu, H.; Li, M.; Chen, A.; Gao, H.; Cai, G.; Pascal, T. A.; Liu, P.; Chen, Z. Electrolyte Design Implications of Ion-Pairing in Low-Temperature Li Metal Batteries. *Energy Environ. Sci.* **2022**, *15* (4), 1647–1658.
- (132) Holoubek, J.; Yu, K.; Wu, J.; Wang, S.; Li, M.; Gao, H.; Hui, Z.; Hyun, G.; Yin, Y.; Mu, A. U.; Kim, K.; Liu, A.; Yu, S.; Pascal, T. A.; Liu, P.; Chen, Z. Toward a Quantitative Interfacial Description of Solvation for Li Metal Battery Operation under Extreme Conditions. *Proc. Natl. Acad. Sci. U. S. A.* 2023, *120* (41), No. e2310714120.
- (133) Yin, Y.; Holoubek, J.; Kim, K.; Liu, A.; Bhamwala, B.; Wang, S.; Lu, B.; Yu, K.; Gao, H.; Li, M.; Raghavendran, G.; Cai, G.; Li, W.; Liu, P.; Meng, Y. S.; Chen, Z. Coulombic Condensation of Liquefied Gas Electrolytes for Li Metal Batteries at Ambient Pressure. *Angew. Chem., Int. Ed.* 2025, 64 (8), No. e202420411.
- (134) Yang, Y.; Davies, D. M.; Yin, Y.; Borodin, O.; Lee, J. Z.; Fang, C.; Olguin, M.; Zhang, Y.; Sablina, E. S.; Wang, X.; Rustomji, C. S.; Meng, Y. S. High-Efficiency Lithium-Metal Anode Enabled by Liquefied Gas Electrolytes. *Joule* **2019**, *3* (8), 1986–2000.
- (135) Thenuwara, A. C.; Shetty, P. P.; Kondekar, N.; Sandoval, S. E.; Cavallaro, K.; May, R.; Yang, C.-T.; Marbella, L. E.; Qi, Y.; McDowell, M. T. Efficient Low-Temperature Cycling of Lithium Metal Anodes by Tailoring the Solid-Electrolyte Interphase. *ACS Energy Lett.* **2020**, *5* (7), 2411–2420.
- (136) Holoubek, J.; Liu, H.; Wu, Z.; Yin, Y.; Xing, X.; Cai, G.; Yu, S.; Zhou, H.; Pascal, T. A.; Chen, Z.; Liu, P. Tailoring Electrolyte Solvation for Li Metal Batteries Cycled at Ultra-Low Temperature. *Nat. Energy* **2021**, *6* (3), 303–313.
- (137) Zhang, N.; Deng, T.; Zhang, S.; Wang, C.; Chen, L.; Wang, C.; Fan, X. Critical Review on Low-Temperature Li-Ion/Metal Batteries. *Adv. Mater.* **2022**, *34* (15), No. e2107899.
- (138) Li, L.; Basu, S.; Wang, Y.; Chen, Z.; Hundekar, P.; Wang, B.; Shi, J.; Shi, Y.; Narayanan, S.; Koratkar, N. Self-Heating-Induced Healing of Lithium Dendrites. *Science* **2018**, *359* (6383), 1513–1516.
- (139) Li, X.; Chen, C.; Fu, Z.; Wang, J.; Hu, C. Compression Promotes the Formation of {110} Textures during Homoepitaxial Deposition of Lithium. *Energy Storage Mater.* **2023**, *58*, 155–164.

- (140) Shi, F.; Pei, A.; Vailionis, A.; Xie, J.; Liu, B.; Zhao, J.; Gong, Y.; Cui, Y. Strong Texturing of Lithium Metal in Batteries. *Proc. Natl. Acad. Sci. U. S. A.* **2017**, *114* (46), 12138–12143.
- (141) Hobold, G. M.; Wang, C.; Steinberg, K.; Li, Y.; Gallant, B. M. High Lithium Oxide Prevalence in the Lithium Solid-Electrolyte Interphase for High Coulombic Efficiency. *Nat. Energy* **2024**, 9 (5), 580–591.
- (142) Yu, W.; Lin, K.-Y.; Boyle, D. T.; Tang, M. T.; Cui, Y.; Chen, Y.; Yu, Z.; Xu, R.; Lin, Y.; Feng, G.; Huang, Z.; Michalek, L.; Li, W.; Harris, S. J.; Jiang, J.-C.; Abild-Pedersen, F.; Qin, J.; Cui, Y.; Bao, Z. Electrochemical Formation of Bis(Fluorosulfonyl)Imide-Derived Solid-Electrolyte Interphase at Li-Metal Potential. *Nat. Chem.* 2025, 17 (2), 246–255.
- (143) He, Y.; Ren, X.; Xu, Y.; Engelhard, M. H.; Li, X.; Xiao, J.; Liu, J.; Zhang, J.-G.; Xu, W.; Wang, C. Origin of Lithium Whisker Formation and Growth under Stress. *Nat. Nanotechnol.* **2019**, *14* (11), 1042–1047.
- (144) Koh, K. H.; Lee, D. J.; Mu, A.; Kim, K.; Kim, T.; Chen, Z. Microstructural Evolution in Lithium Plating Process and Its Effect on the Calendar Storage Life. *Nano Res.* **2024**, *17* (10), 8834–8841.
- (145) Camacho-Forero, L. E.; Smith, T. W.; Balbuena, P. B. Effects of High and Low Salt Concentration in Electrolytes at Lithium-Metal Anode Surfaces. *J. Phys. Chem. C* **2017**, *121* (1), 182–194.
- (146) Qian, J.; Henderson, W. A.; Xu, W.; Bhattacharya, P.; Engelhard, M.; Borodin, O.; Zhang, J.-G. High Rate and Stable Cycling of Lithium Metal Anode. *Nat. Commun.* **2015**, *6* (1), 6362.
- (147) Kwon, H.; Choi, H.-J.; Jang, J.; Lee, J.; Jung, J.; Lee, W.; Roh, Y.; Baek, J.; Shin, D. J.; Lee, J.-H.; Choi, N.-S.; Meng, Y. S.; Kim, H.-T. Weakly Coordinated Li Ion in Single-Ion-Conductor-Based Composite Enabling Low Electrolyte Content Li-Metal Batteries. *Nat. Commun.* 2023, 14 (1), 4047.
- (148) Kwon, H.; Kim, H.; Hwang, J.; Oh, W.; Roh, Y.; Shin, D.; Kim, H.-T. Borate-Pyran Lean Electrolyte-Based Li-Metal Batteries with Minimal Li Corrosion. *Nat. Energy* **2024**, *9* (1), 57–69.
- (149) Choi, I. R.; Chen, Y.; Shah, A.; Florian, J.; Serrao, C.; Holoubek, J.; Lyu, H.; Zhang, E.; Lee, J. H.; Lin, Y.; Kim, S. C.; Park, H.; Zhang, P.; Lee, J.; Qin, J.; Cui, Y.; Bao, Z. Asymmetric Ether Solvents for High-Rate Lithium Metal Batteries. *Nat. Energy* **2025**, *10* (3), 365–379.
- (150) Wang, A.; Kadam, S.; Li, H.; Shi, S.; Qi, Y. Review on Modeling of the Anode Solid Electrolyte Interphase (SEI) for Lithium-Ion Batteries. *npj Comput. Mater.* **2018**, *4* (1), 15.
- (151) Chen, X.; Zhang, Q. Atomic Insights into the Fundamental Interactions in Lithium Battery Electrolytes. *Acc. Chem. Res.* **2020**, *53* (9), 1992–2002.
- (152) Hui, Z.; Yu, S.; Wang, S.; Hyun, G.; Holoubek, J.; Zhou, K.; Nicolas, J.; Liu, M.; Miao, Q.; Tan, S.; Petrova, V.; Lin, H.; Zhou, J.; Liu, H.; Liu, P. Nucleation Processes at Interfaces with Both Substrate and Electrolyte Control Lithium Growth. *Nat. Chem.* **2025**, 1–10.
- (153) Janek, J.; Zeier, W. G. A Solid Future for Battery Development. *Nat. Energy* **2016**, *1* (9), 16141.
- (154) Janek, J.; Zeier, W. G. Challenges in Speeding up Solid-State Battery Development. *Nat. Energy* **2023**, *8* (3), 230–240.
- (155) Tang, W.; Xu, D.; Wu, J.; Lee, D. J.; Fuqua, A.; Li, F.; Jeon, Y.; Bian, W.; Chen, Z. Stable Cycling of Sodium All-Solid-State Batteries with High-Capacity Cathode Presodiation. *Adv. Energy Mater.* **2025**, *15* (23), 2405678.
- (156) Xu, D.; Tang, W.; Li, F.; Zhou, K.; Wu, J.; Fuqua, A.; Chen, Y.; Lee, D. J.; Qin, J.; Tao, A. R.; Liu, P.; Chen, Z. Insights on Na₃PS₄ Solid-State Electrolyte Dry Films: Interfacial Stability and Dry Room Compatibility. *ACS Energy Lett.* **2024**, *9* (5), 2293–2302.
- (157) Fuchs, T.; Ortmann, T.; Becker, J.; Haslam, C. G.; Ziegler, M.; Singh, V. K.; Rohnke, M.; Mogwitz, B.; Peppler, K.; Nazar, L. F.; Sakamoto, J.; Janek, J. Imaging the Microstructure of Lithium and Sodium Metal in Anode-Free Solid-State Batteries Using Electron Backscatter Diffraction. *Nat. Mater.* **2024**, *23*, 1678.
- (158) Becker, J.; Fuchs, T.; Ortmann, T.; Kremer, S.; Richter, F. H.; Janek, J. Microstructure of Lithium Metal Electrodeposited at the Steell Li₆PS₅Cl Interface in "Anode-Free" Solid-State Batteries. *Adv. Energy Mater.* **2025**, *15* (16), 2404975.

- (159) Becker, J.; Fuchs, T.; Ortmann, T.; Schuster, L.; Kremer, S.; Richter, F. H.; Janek, J. Analysis of the Microstructural Evolution of Lithium Metal during Electrodeposition and Subsequent Dissolution in "Anode-Free" Solid-State Batteries Using Electron-Backscatter Diffraction on Millimeter-Sized Cross-Sections. *Microsc. Microanal.* 2025, 31 (Supplement_1), ozaf048.642.
- (160) Zhang, M.; Tantratian, K.; Ham, S.-Y.; Wang, Z.; Chouchane, M.; Shimizu, R.; Bai, S.; Yang, H.; Liu, Z.; Li, L.; Avishai, A.; Chen, L.; Meng, Y. S. Grain Selection Growth of Soft Metal in Electrochemical Processes. *Joule* **2025**, *9*, 101847.
- (161) Yang, M.; Liu, Y.; Mo, Y. Lithium Crystallization at Solid Interfaces. *Nat. Commun.* **2023**, *14* (1), 2986.
- (162) Yang, M.; Liu, Y.; Nolan, A. M.; Mo, Y. Interfacial Atomistic Mechanisms of Lithium Metal Stripping and Plating in Solid-State Batteries. *Adv. Mater.* **2021**, *33* (11), No. e2008081.
- (163) Yang, M.; Mo, Y. Interfacial Defect of Lithium Metal in Solid-State Batteries. *Angew. Chem., Int. Ed.* **2021**, *60* (39), 21494–21501.
- (164) Nie, C.; Wang, G.; Wang, D.; Wang, M.; Gao, X.; Bai, Z.; Wang, N.; Yang, J.; Xing, Z.; Dou, S. Recent Progress on Zn Anodes for Advanced Aqueous Zinc-Ion Batteries. *Adv. Energy Mater.* **2023**, *13* (28), 2300606.
- (165) Guo, X.; He, G. Opportunities and Challenges of Zinc Anodes in Rechargeable Aqueous Batteries. *J. Mater. Chem. A* **2023**, *11* (23), 11987–12001.
- (166) Zhu, Y.; Liang, G.; Cui, X.; Liu, X.; Zhong, H.; Zhi, C.; Yang, Y. Engineering Hosts for Zn Anodes in Aqueous Zn-Ion Batteries. *Energy Environ. Sci.* **2024**, *17* (2), 369–385.
- (167) Gan, H.; Li, H.; Xu, M.; Han, C.; Cheng, H.-M. Failure Mechanisms and Remedy of an Ultrathin Zn Metal Anode in Pouch Cells. *Joule* **2024**, *8* (11), 3054–3071.
- (168) Zheng, J.; Zhao, Q.; Tang, T.; Yin, J.; Quilty, C. D.; Renderos, G. D.; Liu, X.; Deng, Y.; Wang, L.; Bock, D. C.; Jaye, C.; Zhang, D.; Takeuchi, E. S.; Takeuchi, K. J.; Marschilok, A. C.; Archer, L. A. Reversible Epitaxial Electrodeposition of Metals in Battery Anodes. *Science* 2019, 366 (6465), 645–648.
- (169) Zhou, J.; Xie, M.; Wu, F.; Mei, Y.; Hao, Y.; Huang, R.; Wei, G.; Liu, A.; Li, L.; Chen, R. Ultrathin Surface Coating of Nitrogen-Doped Graphene Enables Stable Zinc Anodes for Aqueous Zinc-Ion Batteries. *Adv. Mater.* **2021**, *33* (33), No. e2101649.
- (170) Gan, H.; Wu, J.; Li, R.; Huang, B.; Liu, H. Ultra-Stable and Deeply Rechargeable Zinc Metal Anode Enabled by a Multifunctional Protective Layer. *Energy Storage Mater.* **2022**, 47, 602–610.
- (171) Yang, X.; Lv, J.; Cheng, C.; Shi, Z.; Peng, J.; Chen, Z.; Lian, X.; Li, W.; Zou, Y.; Zhao, Y.; Rümmeli, M. H.; Dou, S.; Sun, J. Mosaic Nanocrystalline Graphene Skin Empowers Highly Reversible Zn Metal Anodes. *Adv. Sci.* **2023**, *10* (4), 2206077.
- (172) Li, X.; Li, Q.; Hou, Y.; Yang, Q.; Chen, Z.; Huang, Z.; Liang, G.; Zhao, Y.; Ma, L.; Li, M.; Huang, Q.; Zhi, C. Toward a Practical Zn Powder Anode: $\mathrm{Ti_3C_2T_x}$ MXene as a Lattice-Match Electrons/Ions Redistributor. ACS Nano 2021, 15 (9), 14631–14642.
- (173) Wang, Y.; Ren, T.; Wang, Z.; Liu, C.; Zhang, Y.; Xu, A.; Chen, C.; Bai, J.; Wang, H.; Liu, X. Enabling and Boosting Preferential Epitaxial Zinc Growth via Multi-Interface Regulation for Stable and Dendrite-Free Zinc Metal Batteries. *Adv. Energy Mater.* **2024**, *14* (26), 2400613.
- (174) Zhao, Z.; Wang, R.; Peng, C.; Chen, W.; Wu, T.; Hu, B.; Weng, W.; Yao, Y.; Zeng, J.; Chen, Z.; Liu, P.; Liu, Y.; Li, G.; Guo, J.; Lu, H.; Guo, Z. Horizontally Arranged Zinc Platelet Electrodeposits Modulated by Fluorinated Covalent Organic Framework Film for High-Rate and Durable Aqueous Zinc Ion Batteries. *Nat. Commun.* **2021**, *12* (1), 6606
- (175) Li, Y.; Wong, H.; Wang, J.; Peng, W.; Shen, Y.; Xu, M.; An, Q.; Kim, J.; Yuan, B.; Goddard, W. A.; Luo, Z. Deposition of Horizontally Stacked Zn Crystals on Single Layer 1T-VSe2 for Dendrite-Free Zn Metal Anodes. *Adv. Energy Mater.* **2022**, *12* (47), 2202983.
- (176) Wang, Y.; Xu, X.; Yin, J.; Huang, G.; Guo, T.; Tian, Z.; Alsaadi, R.; Zhu, Y.; Alshareef, H. N. MoS₂-Mediated Epitaxial Plating of Zn Metal Anodes. *Adv. Mater.* **2023**, *35* (6), No. e2208171.

- (177) Wright, S. C.; Brea, C.; Baxter, J. S.; Saini, S.; Alsaç, E. P.; Yoon, S. G.; Boebinger, M. G.; Hu, G.; McDowell, M. T. Epitaxial Metal Electrodeposition Controlled by Graphene Layer Thickness. *ACS Nano* **2024**, *18* (21), 13866–13875.
- (178) Zou, Y.; Wu, Y.; Wei, W.; Qiao, C.; Lu, M.; Su, Y.; Guo, W.; Yang, X.; Song, Y.; Tian, M.; Dou, S.; Liu, Z.; Sun, J. Establishing Pinhole Deposition Mode of Zn via Scalable Monolayer Graphene Film. *Adv. Mater.* **2024**, *36* (19), No. e2313775.
- (179) Ji, J.; Zhu, Z.; Du, H.; Qi, X.; Yao, J.; Wan, H.; Wang, H.; Qie, L.; Huang, Y. Zinc-Contained Alloy as a Robustly Adhered Interfacial Lattice Locking Layer for Planar and Stable Zinc Electrodeposition. *Adv. Mater.* **2023**, *35* (20), No. e2211961.
- (180) Zhang, M.; Sun, C.; Chen, G.; Kang, Y.; Lv, Z.; Yang, J.; Li, S.; Lin, P.; Tang, R.; Wen, Z.; Li, C. C.; Zhao, J.; Yang, Y. Synergetic Bifunctional Cu-In Alloy Interface Enables Ah-Level Zn Metal Pouch Cells. *Nat. Commun.* **2024**, *15* (1), 9455.
- (181) Yang, X.; Li, C.; Sun, Z.; Yang, S.; Shi, Z.; Huang, R.; Liu, B.; Li, S.; Wu, Y.; Wang, M.; Su, Y.; Dou, S.; Sun, J. Interfacial Manipulation via In Situ Grown ZnSe Cultivator toward Highly Reversible Zn Metal Anodes. *Adv. Mater.* **2021**, 33 (52), No. e2105951.
- (182) Wang, R.; Xin, S.; Chao, D.; Liu, Z.; Wan, J.; Xiong, P.; Luo, Q.; Hua, K.; Hao, J.; Zhang, C. Fast and Regulated Zinc Deposition in a Semiconductor Substrate toward High-Performance Aqueous Rechargeable Batteries. *Adv. Funct. Mater.* **2022**, 32 (51), 2207751.
- (183) Lu, H.; Jin, Q.; Jiang, X.; Dang, Z.; Zhang, D.; Jin, Y. Vertical Crystal Plane Matching between AgZn₃ (002) and Zn (002) Achieving a Dendrite-Free Zinc Anode. *Small* **2022**, *18* (16), No. e2200131.
- (184) Zheng, J.; Cao, Z.; Ming, F.; Liang, H.; Qi, Z.; Liu, W.; Xia, C.; Chen, C.; Cavallo, L.; Wang, Z.; Alshareef, H. N. Preferred Orientation of TiN Coatings Enables Stable Zinc Anodes. *ACS Energy Lett.* **2022**, 7 (1), 197–203.
- (185) Yang, Z.; Lv, C.; Li, W.; Wu, T.; Zhang, Q.; Tang, Y.; Shao, M.; Wang, H. Revealing the Two-Dimensional Surface Diffusion Mechanism for Zinc Dendrite Formation on Zinc Anode. *Small* **2022**, *18* (43), No. e2104148.
- (186) Han, Y.; Wang, F.; Zhang, B.; Yan, L.; Hao, J.; Zhu, C.; Zou, X.; Zhou, Y.; Xiang, B. Building Block Effect Induces Horizontally Oriented Bottom Zn(002) Deposition for a Highly Stable Zinc Anode. *Energy Storage Mater.* **2023**, *62*, 102928.
- (187) Chen, X.; Li, W.; Hu, S.; Akhmedov, N. G.; Reed, D.; Li, X.; Liu, X. Polyvinyl Alcohol Coating Induced Preferred Crystallographic Orientation in Aqueous Zinc Battery Anodes. *Nano Energy* **2022**, *98*, 107269.
- (188) Hu, X.; Dong, H.; Gao, N.; Wang, T.; He, H.; Gao, X.; Dai, Y.; Liu, Y.; Brett, D. J. L.; Parkin, I. P.; He, G. Self-Assembled Polyelectrolytes with Ion-Separation Accelerating Channels for Highly Stable Zn-Ion Batteries. *Nat. Commun.* **2025**, *16* (1), 2316.
- (189) Gao, N.; Cui, M.; Xi, K.; Deng, T.; Yin, D.; He, J.; Cui, X.; Liu, L.; Li, W.; Ding, S.; Gao, G.; Zhao, H. Elimination of Concentration Polarization Under Ultra-High Current Density Zinc Deposition by Nanofluid Self-Driven Ion Enrichment. *Adv. Mater.* **2025**, *37*, No. e2419034.
- (190) Deng, D.; Fu, K.; Yu, R.; Zhu, J.; Cai, H.; Zhang, X.; Wu, J.; Luo, W.; Mai, L. Ion Tunnel Matrix Initiated Oriented Attachment for Highly Utilized Zn Anodes. *Adv. Mater.* **2023**, *35* (33), No. e2302353.
- (191) Zhou, M.; Guo, S.; Li, J.; Luo, X.; Liu, Z.; Zhang, T.; Cao, X.; Long, M.; Lu, B.; Pan, A.; Fang, G.; Zhou, J.; Liang, S. Surface-Preferred Crystal Plane for a Stable and Reversible Zinc Anode. *Adv. Mater.* **2021**, 33 (21), No. e2100187.
- (192) Pu, S. D.; Gong, C.; Tang, Y. T.; Ning, Z.; Liu, J.; Zhang, S.; Yuan, Y.; Melvin, D.; Yang, S.; Pi, L.; Marie, J.; Hu, B.; Jenkins, M.; Li, Z.; Liu, B.; Tsang, S. C. E.; Marrow, T. J.; Reed, R. C.; Gao, X.; Bruce, P. G.; Robertson, A. W. Achieving Ultrahigh-Rate Planar and Dendrite-Free Zinc Electroplating for Aqueous Zinc Battery Anodes. *Adv. Mater.* **2022**, 34 (28), No. e2202552.
- (193) Chen, S.; Luo, Z.; Xia, Y.; Wu, X.; Wang, K.; Yan, M.; Pan, H.; Xu, B. B.; Jiang, Y. Step-Edge Guided Homoepitaxy Enables Highly Reversible Zn Plating/Stripping. *Angew. Chem., Int. Ed.* **2025**, *137*, No. e202501176.

- (194) Liu, Z.; Guo, Z.; Fan, L.; Zhao, C.; Chen, A.; Wang, M.; Li, M.; Lu, X.; Zhang, J.; Zhang, Y.; Zhang, N. Construct Robust Epitaxial Growth of (101) Textured Zinc Metal Anode for Long Life and High Capacity in Mild Aqueous Zinc-Ion Batteries. *Adv. Mater.* **2024**, *36* (5), No. e2305988.
- (195) Chen, Z.; Wang, Y.; Wu, Q.; Wang, C.; He, Q.; Hu, T.; Han, X.; Chen, J.; Zhang, Y.; Chen, J.; Yang, L.; Wang, X.; Ma, Y.; Zhao, J. Grain Boundary Filling Empowers (002)-Textured Zn Metal Anodes with Superior Stability. *Adv. Mater.* **2024**, *36* (46), No. e2411004.
- (196) Zhao, Y.; Guo, S.; Chen, M.; Lu, B.; Zhang, X.; Liang, S.; Zhou, J. Tailoring Grain Boundary Stability of Zinc-Titanium Alloy for Long-Lasting Aqueous Zinc Batteries. *Nat. Commun.* **2023**, *14* (1), 7080.
- (197) Su, Y.; Chen, B.; Sun, Y.; Xue, Z.; Zou, Y.; Yang, D.; Sun, L.; Yang, X.; Li, C.; Yang, Y.; Song, X.; Guo, W.; Dou, S.; Chao, D.; Liu, Z.; Sun, J. Rationalized Electroepitaxy toward Scalable Single-Crystal Zn Anodes. *Adv. Mater.* **2023**, 35 (28), No. e2301410.
- (198) Yi, Z.; Liu, J.; Tan, S.; Sang, Z.; Mao, J.; Yin, L.; Liu, X.; Wang, L.; Hou, F.; Dou, S. X.; Cheng, H.; Liang, J. An Ultrahigh Rate and Stable Zinc Anode by Facet-Matching-Induced Dendrite Regulation. *Adv. Mater.* **2022**, *34* (37), No. e2203835.
- (199) Xie, C.; Ji, H.; Zhang, Q.; Yang, Z.; Hu, C.; Ji, X.; Tang, Y.; Wang, H. High-Index Zinc Facet Exposure Induced by Preferentially Orientated Substrate for Dendrite-Free Zinc Anode. *Adv. Energy Mater.* **2023**, *13* (3), 2203203.
- (200) Yan, Y.; Shu, C.; Zeng, T.; Wen, X.; Liu, S.; Deng, D.; Zeng, Y. Surface-Preferred Crystal Plane Growth Enabled by Underpotential Deposited Monolayer toward Dendrite-Free Zinc Anode. *ACS Nano* **2022**, *16* (6), 9150–9162.
- (201) Huang, C.; Zhao, X.; Liu, S.; Hao, Y.; Tang, Q.; Hu, A.; Liu, Z.; Chen, X. Stabilizing Zinc Anodes by Regulating the Electrical Double Layer with Saccharin Anions. *Adv. Mater.* **2021**, *33* (38), No. e2100445.
- (202) Ma, L.; Schroeder, M. A.; Borodin, O.; Pollard, T. P.; Ding, M. S.; Wang, C.; Xu, K. Realizing High Zinc Reversibility in Rechargeable Batteries. *Nat. Energy* **2020**, *S* (10), 743–749.
- (203) Li, C.; Kingsbury, R.; Zhou, L.; Shyamsunder, A.; Persson, K. A.; Nazar, L. F. Tuning the Solvation Structure in Aqueous Zinc Batteries to Maximize Zn-Ion Intercalation and Optimize Dendrite-Free Zinc Plating. ACS Energy Lett. 2022, 7 (1), 533–540.
- (204) Liu, Q.; Liu, X.; Liu, Y.; Huang, M.; Wang, W.; Cheng, Y.; Zhang, H.; Xu, L. Atomic-Level Customization of Zinc Crystallization Kinetics at the Interface for High-Utilization Zn Anodes. *ACS Nano* **2024**, *18* (6), 4932–4943.
- (205) Yuan, W.; Nie, X.; Wang, Y.; Li, X.; Ma, G.; Wang, Y.; Shen, S.; Zhang, N. Orientational Electrodeposition of Highly (002)-Textured Zinc Metal Anodes Enabled by Iodide Ions for Stable Aqueous Zinc Batteries. ACS Nano 2023, 17 (23), 23861–23871.
- (206) Wang, Y.; Wang, Z.; Pang, W. K.; Lie, W.; Yuwono, J. A.; Liang, G.; Liu, S.; Angelo, A. M. D.; Deng, J.; Fan, Y.; Davey, K.; Li, B.; Guo, Z. Solvent Control of Water O-H Bonds for Highly Reversible Zinc Ion Batteries. *Nat. Commun.* **2023**, *14* (1), 2720.
- (207) Li, J.; Zhou, S.; Chen, Y.; Meng, X.; Azizi, A.; He, Q.; Li, H.; Chen, L.; Han, C.; Pan, A. Self-Smoothing Deposition Behavior Enabled by Beneficial Potential Compensating for Highly Reversible Zn-Metal Anodes. *Adv. Funct. Mater.* **2023**, *33* (52), 2307201.
- (208) Huang, Z.; Li, Z.; Wang, Y.; Cong, J.; Wu, X.; Song, X.; Ma, Y.; Xiang, H.; Huang, Y. Regulating Zn(002) Deposition toward Long Cycle Life for Zn Metal Batteries. ACS Energy Lett. 2023, 8 (1), 372–380.
- (209) Li, Y.; Zheng, X.; Carlson, E. Z.; Xiao, X.; Chi, X.; Cui, Y.; Greenburg, L. C.; Zhang, G.; Zhang, E.; Liu, C.; Yang, Y.; Kim, M. S.; Feng, G.; Zhang, P.; Su, H.; Guan, X.; Zhou, J.; Wu, Y.; Xue, Z.; Li, W.; Bajdich, M.; Cui, Y. In Situ Formation of Liquid Crystal Interphase in Electrolytes with Soft Templating Effects for Aqueous Dual-Electrode-Free Batteries. *Nat. Energy* **2024**, *9* (11), 1350–1359.
- (210) Ma, G.; Yuan, W.; Li, X.; Bi, T.; Niu, L.; Wang, Y.; Liu, M.; Wang, Y.; Shen, Z.; Zhang, N. Organic Cations Texture Zinc Metal Anodes for Deep Cycling Aqueous Zinc Batteries. *Adv. Mater.* **2024**, *36* (35), No. e2408287.

- (211) Zhang, H.; Zhong, Y.; Li, J.; Liao, Y.; Zeng, J.; Shen, Y.; Yuan, L.; Li, Z.; Huang, Y. Inducing the Preferential Growth of Zn (002) Plane for Long Cycle Aqueous Zn-Ion Batteries. *Adv. Energy Mater.* **2023**, *13* (1), 2203254.
- (212) Xie, W.; Zhu, K.; Jiang, W.; Yang, H.; Ma, M.; Zhao, L.; Yang, W. Highly 002-Oriented Dendrite-Free Anode Achieved by Enhanced Interfacial Electrostatic Adsorption for Aqueous Zinc-Ion Batteries. *ACS Nano* **2024**, *18* (32), 21184–21197.
- (213) Allen, L. N.; Wang, Z.; Shan, L.; Tang, B.; Mullins, C. B. Promoting Preferential Zn (002) Deposition with a Low-Concentration Electrolyte Additive for Highly Reversible Zn-Ion Batteries. ACS Appl. Mater. Interfaces 2024, 16 (36), 47599–47609.
- (214) Wei, T.; Zhang, H.; Ren, Y.; Mo, L.; He, Y.; Tan, P.; Huang, Y.; Li, Z.; Zhu, D.; Hu, L. Building Near-Unity Stacked (002) Texture for High-Stable Zinc Anode. *Adv. Funct. Mater.* **2024**, 34 (14), 2312506.
- (215) Wan, J.; Wang, R.; Liu, Z.; Zhang, L.; Liang, F.; Zhou, T.; Zhang, S.; Zhang, L.; Lu, Q.; Zhang, C.; Guo, Z. A Double-Functional Additive Containing Nucleophilic Groups for High-Performance Zn-Ion Batteries. ACS Nano 2023, 17 (2), 1610–1621.
- (216) Deng, R.; He, Z.; Chu, F.; Lei, J.; Cheng, Y.; Zhou, Y.; Wu, F. An Aqueous Electrolyte Densified by Perovskite SrTiO₃ Enabling High-Voltage Zinc-Ion Batteries. *Nat. Commun.* **2023**, *14* (1), 4981.
- (217) Chen, Y.; Zhou, S.; Li, J.; Zhang, X.; Zhou, C.; Shi, X.; Zhang, C.; Fang, G.; Liang, S.; Su, Z.; Pan, A. Tuning Zn²⁺ Deposition Kinetics towards Deep-Reversible Zinc Metal Batteries with All-Climate Adaptability. *Angew. Chem., Int. Ed.* **2025**, *64*, No. e202423252.
- (218) Wu, F.; Zhang, J.; Ma, L.; Ruan, P.; Chen, Y.; Meng, S.; Yin, R.; Shi, W.; Liu, W.; Zhou, J.; Cao, X. Directing Zn Growth with Biased Adsorption of Straight-chain Molecules for Superior Zn Anode Stability. *Angew. Chem., Int. Ed.* **2025**, *64* (11), No. e202421787.
- (219) Huang, H.; Xu, J.; Huang, Y.; He, Z.; Feng, H.; Hu, C.; Chen, Z.; Yang, Z.; Tian, T.; Zhang, W. Adjusting Interface Dynamics: A New Insight into the Role of Electrolyte Additive in Facilitating Highly Reversible (002)-Textured Zinc Anode at High Current and Areal Densities. *Adv. Energy Mater.* **2024**, *14* (41), 2401643.
- (220) Xiao, Z.; Dai, X.; Zhu, J.; Liu, D.; Liu, L.; Liu, X.; Li, Y.; Qian, Z.; Wang, R. Hydrogen Bond Competition Optimizing Aqueous Zn Ion Solvation and (002) Interfacial Deposition with Ultralong Stability. *Adv. Funct. Mater.* **2025**, 35 (23), 2424860.
- (221) Cheng, Z.; Wang, K.; Fu, J.; Mo, F.; Lu, P.; Gao, J.; Ho, D.; Li, B.; Hu, H. Texture Exposure of Unconventional (101)Zn Facet: Enabling Dendrite-Free Zn Deposition on Metallic Zinc Anodes. *Adv. Energy Mater.* **2024**, *14* (16), 2304003.
- (222) Wang, Y.; Lv, J.; Hong, L.; Zhang, J.; Chen, C.; Xu, A.; Huang, M.; Ren, X.; Bai, J.; Wang, H.; Liu, X. Customizing H₂O-Poor Electric Double Layer and Boosting Texture Exposure of Zn (101) Plane towards Super-High Areal Capacity Zinc Metal Batteries. *Angew. Chem.* **2025**, 137 (2), No. e202414757.
- (223) Yang, H.; Fang, K.; Duan, J.; Dong, J.; Li, Y.; Yang, S.; Liang, J.; Jiang, Y.; Li, M.; Liu, Y.; Shen, Z.; Liu, R.; Cao, R.; Li, F.; Huang, Y. Selective Facet Shielding Induced Epitaxial Deposition along the Zn (101) Plane for Highly Reversible Zn-Ion Batteries. *Energy Storage Mater.* 2025, 75, 103995.
- (224) Su, Y.; Xu, L.; Sun, Y.; Guo, W.; Yang, X.; Zou, Y.; Ding, M.; Zhang, Q.; Qiao, C.; Dou, S.; Cheng, T.; Sun, J. A Holistic Additive Protocol Steers Dendrite-Free Zn(101) Orientational Electrodeposition. *Small* **2024**, 20 (11), No. e2308209.
- (225) Zhu, Q.; Sun, G.; Qiao, S.; Wang, D.; Cui, Z.; Zhang, W.; Liu, J. Selective Shielding of the (002) Plane Enabling Vertically Oriented Zinc Plating for Dendrite-Free Zinc Anode. *Adv. Mater.* **2024**, *36* (11), No. e2308577.
- (226) Zhang, J.-Z.; Zhao, Q.-Y.; Wei, X.; Li, A.; Xu, H.; Chen, G.; Zheng, Y.-S.; Xu, Y.-T.; Wang, X.-F. Crystallographic Customization of Zinc Anode for High Performance Aqueous Metal Batteries. *Nano Lett.* **2025**, 25 (2), 648–654.
- (227) Yuan, W.; Nie, X.; Ma, G.; Liu, M.; Wang, Y.; Shen, S.; Zhang, N. Realizing Textured Zinc Metal Anodes through Regulating Electrodeposition Current for Aqueous Zinc Batteries. *Angew. Chem., Int. Ed.* **2023**, *62* (10), No. e202218386.

- (228) Cai, Z.; Wang, J.; Lu, Z.; Zhan, R.; Ou, Y.; Wang, L.; Dahbi, M.; Alami, J.; Lu, J.; Amine, K.; Sun, Y. Ultrafast Metal Electrodeposition Revealed by In Situ Optical Imaging and Theoretical Modeling towards Fast-Charging Zn Battery Chemistry. *Angew. Chem., Int. Ed.* **2022**, *61* (14), No. e202116560.
- (229) Zhang, J.; Huang, W.; Li, L.; Chang, C.; Yang, K.; Gao, L.; Pu, X. Nonepitaxial Electrodeposition of (002)-Textured Zn Anode on Textureless Substrates for Dendrite-Free and Hydrogen Evolution-Suppressed Zn Batteries. *Adv. Mater.* **2023**, *35* (21), No. e2300073.
- (230) Zheng, J. X. K.; Yin, J.; Tang, T.; Archer, L. A. Moss-like Growth of Metal Electrodes: On the Role of Competing Faradaic Reactions and Fast Charging. *ACS Energy Lett.* **2023**, *8* (5), 2113–2121.
- (231) Liu, Z.; Liu, J.; Xiao, X.; Zheng, Z.; Zhong, X.; Fu, Q.; Wang, S.; Zhou, G. Unraveling Paradoxical Effects of Large Current Density on Zn Deposition. *Adv. Mater.* **2024**, *36* (27), No. e2404140.
- (232) Zhang, B.; Dong, P.; Yuan, S.; Zhang, Y.; Zhang, Y.; Wang, Y. Manganese-Based Oxide Cathode Materials for Aqueous Zinc-Ion Batteries: Materials, Mechanism, Challenges, and Strategies. *Chem. Bio Eng.* **2024**, *1* (2), 113–132.
- (233) Li, G.; Sun, L.; Zhang, S.; Zhang, C.; Jin, H.; Davey, K.; Liang, G.; Liu, S.; Mao, J.; Guo, Z. Developing Cathode Materials for Aqueous Zinc Ion Batteries: Challenges and Practical Prospects. *Adv. Funct. Mater.* **2024**, 34 (5), 2301291.
- (234) Li, Y.; Chen, W.; Jia, S.; Tang, M.; Zhai, Y.; Zhan, L.; Chen, W. Ultrathin Zn(002) Textured Zinc Anodes for Dendrite-Free and Hydrogen Evolution-Inhibited Zinc Batteries. *J. Power Sources* **2024**, *614*, 235040.
- (235) Li, Z.; Yuan, Y.; Pu, S. D.; Qi, R.; Ding, S.; Qin, R.; Kareer, A.; Bruce, P. G.; Robertson, A. W. Achieving Planar Zn Electroplating in Aqueous Zinc Batteries with Cathode-Compatible Current Densities by Cycling under Pressure. *Adv. Mater.* **2024**, *36* (32), No. e2401576. (236) Deng, T.; Ji, X.; Zou, L.; Chiekezi, O.; Cao, L.; Fan, X.; Adebisi, T. R.; Chang, H.-J.; Wang, H.; Li, B.; Li, X.; Wang, C.; Reed, D.; Zhang, J.-G.; Sprenkle, V. L.; Wang, C.; Lu, X. Interfacial-Engineering-Enabled Practical Low-Temperature Sodium Metal Battery. *Nat. Nanotechnol.* **2022**, *17* (3), 269–277.
- (237) Zhong, Y.; Shi, Q.; Zhu, C.; Zhang, Y.; Li, M.; Francisco, J. S.; Wang, H. Mechanistic Insights into Fast Charging and Discharging of the Sodium Metal Battery Anode: A Comparison with Lithium. *J. Am. Chem. Soc.* **2021**, *143* (34), 13929–13936.
- (238) Li, H.; Wu, F.; Wang, J.; Wang, J.; Qu, H.; Chen, M.; Zhang, H.; Passerini, S. Anode-Free Sodium Metal Batteries: Optimisation of Electrolytes and Interphases. *Energy Environ. Sci.* **2025**, *18*, 3887–3916. (239) Cohn, A. P.; Muralidharan, N.; Carter, R.; Share, K.; Pint, C. L. Anode-Free Sodium Battery through in Situ Plating of Sodium Metal. *Nano Lett.* **2017**, *17* (2), 1296–1301.
- (240) Wu, S.; Hwang, J.; Matsumoto, K.; Hagiwara, R. The Rational Design of Low-Barrier Fluorinated Aluminum Substrates for Anode-Free Sodium Metal Battery. *Adv. Energy Mater.* **2023**, *13* (48), 2302468. (241) Tang, F.; Yang, Y.; Liu, C.; Yang, S.; Xu, S.; Yao, Y.; Yang, H.; Yang, Y.; He, S.; Pan, H.; Rui, X.; Yu, Y. Initially Anode-Free Sodium Metal Battery Enabled by Strain-Engineered Single-Crystal Aluminum Substrate with (100)-Preferred Orientation. *Nat. Commun.* **2025**, *16* (1), 2280.
- (242) Lin, M.-C.; Gong, M.; Lu, B.; Wu, Y.; Wang, D.-Y.; Guan, M.; Angell, M.; Chen, C.; Yang, J.; Hwang, B.-J.; Dai, H. An Ultrafast Rechargeable Aluminium-Ion Battery. *Nature* **2015**, *520* (7547), 324–328
- (243) Muldoon, J.; Bucur, C. B.; Gregory, T. Quest for Nonaqueous Multivalent Secondary Batteries: Magnesium and Beyond. *Chem. Rev.* **2014**, *114* (23), 11683–11720.
- (244) Jayaprakash, N.; Das, S. K.; Archer, L. A. The Rechargeable Aluminum-Ion Battery. *Chem. Commun.* **2011**, 47 (47), 12610–12612. (245) Wang, S.; Guo, Y.; Du, X.; Xiong, L.; Liang, Z.; Ma, M.; Xie, Y.; You, W.; Meng, Y.; Liu, Y.; Liu, M. Preferred Crystal Plane Electrodeposition of Aluminum Anode with High Lattice-Matching for Long-Life Aluminum Batteries. *Nat. Commun.* **2024**, 15 (1), 6476.

- (246) Zhao, Q.; Zheng, J.; Deng, Y.; Archer, L. Regulating the Growth of Aluminum Electrodeposits: Towards Anode-Free Al Batteries. *J. Mater. Chem. A* **2020**, 8 (44), 23231–23238.
- (247) Meng, Y.; Wang, J.; Wang, M.; Peng, Q.; Xie, Z.; Zhu, Z.; Liu, Z.; Wang, W.; Zhang, K.; Liu, H.; Ma, Y.; Li, Z.; Chen, W. Anode-Free Aluminum Electrode with Ultralong Cycle Life and High Coulombic Efficiency Exceeding 99.92% Enabled by a Lattice-Matching Layer. *Adv. Energy Mater.* **2023**, *13* (30), 2301322.
- (248) Matsui, M. Study on Electrochemically Deposited Mg Metal. J. Power Sources 2011, 196 (16), 7048–7055.
- (249) Liu, J.; Zhang, J.; Zhang, Z.; Du, A.; Dong, S.; Zhou, Z.; Guo, X.; Wang, Q.; Li, Z.; Li, G.; Cui, G. Epitaxial Electrocrystallization of Magnesium via Synergy of Magnesiophilic Interface, Lattice Matching, and Electrostatic Confinement. ACS Nano 2022, 16 (6), 9894–9907.
- (250) Li, Y.; Feng, X.; Lieu, W. Y.; Fu, L.; Zhang, C.; Ghosh, T.; Thakur, A.; Wyatt, B. C.; Anasori, B.; Liu, W.; Zhang, Q.; Lu, J.; Seh, Z. W. MXene-Based Anode-Free Magnesium Metal Battery. *Adv. Funct. Mater.* **2023**, 33 (33), 2303067.
- (251) Li, C.; Guha, R. D.; House, S. D.; Bazak, J. D.; Yu, Y.; Zhou, L.; Zavadil, K.; Persson, K. A.; Nazar, L. F. A Dynamically Bare Metal Interface Enables Reversible Magnesium Electrodeposition at 50 mAh cm⁻². *Joule* **2025**, *9* (2), 101790.
- (252) Yang, G.; Li, Y.; Wang, J.; Lum, Y.; Lim, C. Y. J.; Ng, M.-F.; Zhang, C.; Chang, Z.; Zhang, Z.; Handoko, A. D.; Ghosh, T.; Li, S.; Sofer, Z.; Liu, W.; Yao, Y.; Seh, Z. W. Realizing Horizontal Magnesium Platelet Deposition and Suppressed Surface Passivation for High-Performance Magnesium Metal Batteries. *Energy Environ. Sci.* **2024**, *17* (3), 1141–1152.
- (253) Lee, S. W.; McDowell, M. T.; Choi, J. W.; Cui, Y. Anomalous Shape Changes of Silicon Nanopillars by Electrochemical Lithiation. *Nano Lett.* **2011**, *11* (7), 3034–3039.
- (254) Chen, S.; Du, A.; Yan, C. Molecular Dynamic Investigation of the Structure and Stress in Crystalline and Amorphous Silicon during Lithiation. *Comput. Mater. Sci.* **2020**, *183*, 109811.
- (255) Yang, H.; Huang, S.; Huang, X.; Fan, F.; Liang, W.; Liu, X. H.; Chen, L.-Q.; Huang, J. Y.; Li, J.; Zhu, T.; Zhang, S. Orientation-Dependent Interfacial Mobility Governs the Anisotropic Swelling in Lithiated Silicon Nanowires. *Nano Lett.* **2012**, *12* (4), 1953–1958.
- (256) Liu, X. H.; Wang, J. W.; Huang, S.; Fan, F.; Huang, X.; Liu, Y.; Krylyuk, S.; Yoo, J.; Dayeh, S. A.; Davydov, A. V.; Mao, S. X.; Picraux, S. T.; Zhang, S.; Li, J.; Zhu, T.; Huang, J. Y. In Situ Atomic-Scale Imaging of Electrochemical Lithiation in Silicon. *Nat. Nanotechnol.* **2012**, *7* (11), 749–756.
- (257) Goldman, J. L.; Long, B. R.; Gewirth, A. A.; Nuzzo, R. G. Strain Anisotropies and Self-Limiting Capacities in Single-Crystalline 3D Silicon Microstructures: Models for High Energy Density Lithium-Ion Battery Anodes. *Adv. Funct. Mater.* **2011**, 21 (13), 2412–2422.
- (258) Lee, S. W.; McDowell, M. T.; Berla, L. A.; Nix, W. D.; Cui, Y. Fracture of Crystalline Silicon Nanopillars during Electrochemical Lithium Insertion. *Proc. Natl. Acad. Sci. U. S. A.* **2012**, *109* (11), 4080–4085
- (259) Lee, S. W.; Lee, H.-W.; Ryu, I.; Nix, W. D.; Gao, H.; Cui, Y. Kinetics and Fracture Resistance of Lithiated Silicon Nanostructure Pairs Controlled by Their Mechanical Interaction. *Nat. Commun.* **2015**, 6 (1), 7533.
- (260) Häusler, M.; Stamati, O.; Gammer, C.; Moitzi, F.; Sinojiya, R. J.; Villanova, J.; Sartory, B.; Scheiber, D.; Keckes, J.; Fuchsbichler, B.; Koller, S.; Brunner, R. Amorphous Shear Band Formation in Crystalline Si-Anodes Governs Lithiation and Capacity Fading in Li-Ion Batteries. *Commun. Mater.* **2024**, *5* (1), 163.
- (261) Shi, F.; Song, Z.; Ross, P. N.; Somorjai, G. A.; Ritchie, R. O.; Komvopoulos, K. Failure Mechanisms of Single-Crystal Silicon Electrodes in Lithium-Ion Batteries. *Nat. Commun.* **2016**, *7* (1), 11886. (262) Hertzberg, B.; Alexeev, A.; Yushin, G. Deformations in Si-Li Anodes Upon Electrochemical Alloying in Nano-Confined Space. *J. Am. Chem. Soc.* **2010**, 132 (25), 8548–8549.
- (263) Wu, H.; Chan, G.; Choi, J. W.; Ryu, I.; Yao, Y.; McDowell, M. T.; Lee, S. W.; Jackson, A.; Yang, Y.; Hu, L.; Cui, Y. Stable Cycling of Double-Walled Silicon Nanotube Battery Anodes through Solid-

- Electrolyte Interphase Control. Nat. Nanotechnol. 2012, 7 (5), 310–315.
- (264) Yao, Y.; McDowell, M. T.; Ryu, I.; Wu, H.; Liu, N.; Hu, L.; Nix, W. D.; Cui, Y. Interconnected Silicon Hollow Nanospheres for Lithium-Ion Battery Anodes with Long Cycle Life. *Nano Lett.* **2011**, *11* (7), 2949–2954.
- (265) He, Y.; Jiang, L.; Chen, T.; Xu, Y.; Jia, H.; Yi, R.; Xue, D.; Song, M.; Genc, A.; Bouchet-Marquis, C.; Pullan, L.; Tessner, T.; Yoo, J.; Li, X.; Zhang, J.-G.; Zhang, S.; Wang, C. Progressive Growth of the Solid-Electrolyte Interphase towards the Si Anode Interior Causes Capacity Fading. *Nat. Nanotechnol.* **2021**, *16* (10), 1113–1120.
- (266) Liu, N.; Wu, H.; McDowell, M. T.; Yao, Y.; Wang, C.; Cui, Y. A Yolk-Shell Design for Stabilized and Scalable Li-Ion Battery Alloy Anodes. *Nano Lett.* **2012**, *12* (6), 3315–3321.
- (267) Liu, N.; Lu, Z.; Zhao, J.; McDowell, M. T.; Lee, H.-W.; Zhao, W.; Cui, Y. A Pomegranate-Inspired Nanoscale Design for Large-Volume-Change Lithium Battery Anodes. *Nat. Nanotechnol.* **2014**, *9* (3), 187–192.
- (268) Li, Y.; Yan, K.; Lee, H.-W.; Lu, Z.; Liu, N.; Cui, Y. Growth of Conformal Graphene Cages on Micrometre-Sized Silicon Particles as Stable Battery Anodes. *Nat. Energy* **2016**, *1* (2), 15029.
- (269) Ko, M.; Chae, S.; Ma, J.; Kim, N.; Lee, H.-W.; Cui, Y.; Cho, J. Scalable Synthesis of Silicon-Nanolayer-Embedded Graphite for High-Energy Lithium-Ion Batteries. *Nat. Energy* **2016**, *1* (9), 16113.
- (270) Sung, J.; Kim, N.; Ma, J.; Lee, J. H.; Joo, S. H.; Lee, T.; Chae, S.; Yoon, M.; Lee, Y.; Hwang, J.; Kwak, S. K.; Cho, J. Subnano-Sized Silicon Anode via Crystal Growth Inhibition Mechanism and Its Application in a Prototype Battery Pack. *Nat. Energy* **2021**, *6* (12), 1164–1175.
- (271) Wang, C.; Wu, H.; Chen, Z.; McDowell, M. T.; Cui, Y.; Bao, Z. Self-Healing Chemistry Enables the Stable Operation of Silicon Microparticle Anodes for High-Energy Lithium-Ion Batteries. *Nat. Chem.* **2013**, 5 (12), 1042–1048.
- (272) Choi, S.; Kwon, T.; Coskun, A.; Choi, J. W. Highly Elastic Binders Integrating Polyrotaxanes for Silicon Microparticle Anodes in Lithium Ion Batteries. *Science* **2017**, *357* (6348), 279–283.
- (273) Wu, H.; Yu, G.; Pan, L.; Liu, N.; McDowell, M. T.; Bao, Z.; Cui, Y. Stable Li-Ion Battery Anodes by in-Situ Polymerization of Conducting Hydrogel to Conformally Coat Silicon Nanoparticles. *Nat. Commun.* **2013**, *4* (1), 1943.
- (274) Chen, Z.; Wang, C.; Lopez, J.; Lu, Z.; Cui, Y.; Bao, Z. High-Areal-Capacity Silicon Electrodes with Low-Cost Silicon Particles Based on Spatial Control of Self-Healing Binder. *Adv. Energy Mater.* **2015**, *5* (8), 1401826.
- (275) Chen, Z.; To, J. W. F.; Wang, C.; Lu, Z.; Liu, N.; Chortos, A.; Pan, L.; Wei, F.; Cui, Y.; Bao, Z. A Three-Dimensionally Interconnected Carbon Nanotube-Conducting Polymer Hydrogel Network for High-Performance Flexible Battery Electrodes. *Adv. Energy Mater.* **2014**, *4* (12), 1400207.
- (276) Chen, J.; Fan, X.; Li, Q.; Yang, H.; Khoshi, M. R.; Xu, Y.; Hwang, S.; Chen, L.; Ji, X.; Yang, C.; He, H.; Wang, C.; Garfunkel, E.; Su, D.; Borodin, O.; Wang, C. Electrolyte Design for LiF-Rich Solid-Electrolyte Interfaces to Enable High-Performance Microsized Alloy Anodes for Batteries. *Nat. Energy* **2020**, *5* (5), 386–397.
- (277) Li, A.-M.; Wang, Z.; Pollard, T. P.; Zhang, W.; Tan, S.; Li, T.; Jayawardana, C.; Liou, S.-C.; Rao, J.; Lucht, B. L.; Hu, E.; Yang, X.-Q.; Borodin, O.; Wang, C. High Voltage Electrolytes for Lithium-Ion Batteries with Micro-Sized Silicon Anodes. *Nat. Commun.* **2024**, *15* (1), 1206.
- (278) Li, A.-M.; Wang, Z.; Lee, T.; Zhang, N.; Li, T.; Zhang, W.; Jayawardana, C.; Yeddala, M.; Lucht, B. L.; Wang, C. Asymmetric Electrolyte Design for High-Energy Lithium-Ion Batteries with Micro-Sized Alloying Anodes. *Nat. Energy* **2024**, *9* (12), 1551–1560.
- (279) Kim, N.; Kim, Y.; Sung, J.; Cho, J. Issues Impeding the Commercialization of Laboratory Innovations for Energy-Dense Si-Containing Lithium-Ion Batteries. *Nat. Energy* **2023**, *8* (9), 921–933. (280) Tan, D. H. S.; Chen, Y.-T.; Yang, H.; Bao, W.; Sreenarayanan, B.; Doux, J.-M.; Li, W.; Lu, B.; Ham, S.-Y.; Sayahpour, B.; Scharf, J.; Wu, E. A.; Deysher, G.; Han, H. E.; Hah, H. J.; Jeong, H.; Lee, J. B.; Chen, Z.;

- Meng, Y. S. Carbon-Free High-Loading Silicon Anodes Enabled by Sulfide Solid Electrolytes. *Science* **2021**, 373 (6562), 1494–1499.
- (281) Ham, S.-Y.; Sebti, E.; Cronk, A.; Pennebaker, T.; Deysher, G.; Chen, Y.-T.; Oh, J. A. S.; Lee, J. B.; Song, M. S.; Ridley, P.; Tan, D. H. S.; Clément, R. J.; Jang, J.; Meng, Y. S. Overcoming Low Initial Coulombic Efficiencies of Si Anodes through Prelithiation in All-Solid-State Batteries. *Nat. Commun.* **2024**, *15* (1), 2991.
- (282) Yan, W.; Mu, Z.; Wang, Z.; Huang, Y.; Wu, D.; Lu, P.; Lu, J.; Xu, J.; Wu, Y.; Ma, T.; Yang, M.; Zhu, X.; Xia, Y.; Shi, S.; Chen, L.; Li, H.; Wu, F. Hard-Carbon-Stabilized Li-Si Anodes for High-Performance All-Solid-State Li-Ion Batteries. *Nat. Energy* **2023**, *8* (8), 800–813.
- (283) Wang, Z.; Shen, X.; Chen, S.; Qiao, R.; Sun, B.; Deng, J.; Song, J. Large-Scale Fabrication of Stable Silicon Anode in Air for Sulfide Solid State Batteries via Ionic-Electronic Dual Conductive Binder. *Adv. Mater.* **2024**, *36* (32), No. e2405025.
- (284) Huo, H.; Jiang, M.; Bai, Y.; Ahmed, S.; Volz, K.; Hartmann, H.; Henss, A.; Singh, C. V.; Raabe, D.; Janek, J. Chemo-Mechanical Failure Mechanisms of the Silicon Anode in Solid-State Batteries. *Nat. Mater.* **2024**, 23 (4), 543–551.
- (285) Wang, C.; Liu, Y.; Jeong, W. J.; Chen, T.; Lu, M.; Nelson, D. L.; Alsaç, E. P.; Yoon, S. G.; Cavallaro, K. A.; Das, S.; Majumdar, D.; Gopalaswamy, R.; Xia, S.; McDowell, M. T. The Influence of Pressure on Lithium Dealloying in Solid-State and Liquid Electrolyte Batteries. *Nat. Mater.* 2025, 24, 1–10.
- (286) Chen, Y.; Jang, J.; Oh, J. A. S.; Ham, S.; Yang, H.; Lee, D.; Vicencio, M.; Lee, J. B.; Tan, D. H. S.; Chouchane, M.; Cronk, A.; Song, M.; Yin, Y.; Qian, J.; Chen, Z.; Meng, Y. S. Enabling Uniform and Accurate Control of Cycling Pressure for All-Solid-State Batteries. *Adv. Energy Mater.* **2024**, *14*, 2304327.
- (287) Didier, C.; Pang, W. K.; Guo, Z.; Schmid, S.; Peterson, V. K. Phase Evolution and Intermittent Disorder in Electrochemically Lithiated Graphite Determined Using in Operando Neutron Diffraction. *Chem. Mater.* **2020**, 32 (6), 2518–2531.
- (288) Wirth, K. G.; Hauck, J. B.; Rothstein, A.; Kyoseva, H.; Siebenkotten, D.; Conrads, L.; Klebl, L.; Fischer, A.; Beschoten, B.; Stampfer, C.; Kennes, D. M.; Waldecker, L.; Taubner, T. Experimental Observation of ABCB Stacked Tetralayer Graphene. *ACS Nano* **2022**, *16* (10), 16617–16623.
- (289) Persson, K.; Sethuraman, V. A.; Hardwick, L. J.; Hinuma, Y.; Meng, Y. S.; van der Ven, A.; Srinivasan, V.; Kostecki, R.; Ceder, G. Lithium Diffusion in Graphitic Carbon. *J. Phys. Chem. Lett.* **2010**, *1* (8), 1176–1180
- (290) Asenbauer, J.; Eisenmann, T.; Kuenzel, M.; Kazzazi, A.; Chen, Z.; Bresser, D. The Success Story of Graphite as a Lithium-Ion Anode Material Fundamentals, Remaining Challenges, and Recent Developments Including Silicon (Oxide) Composites. *Sustain. Energy Fuels* **2020**, *4* (11), 5387–5416.
- (291) Ruffieux, P.; Wang, S.; Yang, B.; Sánchez-Sánchez, C.; Liu, J.; Dienel, T.; Talirz, L.; Shinde, P.; Pignedoli, C. A.; Passerone, D.; Dumslaff, T.; Feng, X.; Müllen, K.; Fasel, R. On-Surface Synthesis of Graphene Nanoribbons with Zigzag Edge Topology. *Nature* **2016**, *S31* (7595), 489–492.
- (292) Zhu, K.; Kramer, D.; Peng, C. Edge and Lithium Concentration Effects on Intercalation Kinetics for Graphite Anodes. *J. Energy Chem.* **2024**, *90*, 337–347.
- (293) Yamada, Y.; Kawai, M.; Yorimitsu, H.; Otsuka, S.; Takanashi, M.; Sato, S. Carbon Materials with Zigzag and Armchair Edges. ACS Appl. Mater. Interfaces 2018, 10 (47), 40710–40739.
- (294) Way, A. J.; Jacobberger, R. M.; Arnold, M. S. Seed-Initiated Anisotropic Growth of Unidirectional Armchair Graphene Nanoribbon Arrays on Germanium. *Nano Lett.* **2018**, *18* (2), 898–906.
- (295) Wu, Y.; Shen, B.; Zhu, Z.; He, Y.; Wei, Z.; Wei, J.; Jiang, H.; Hu, Y.; Li, C. Multifunctional Lithium Compensation Agent Based on Carbon Edges Catalysis and Its Application in Anode-Free Lithium Batteries. *Chem. Eng. J.* **2023**, 458, 141411.
- (296) Song, X. Y.; Kinoshita, K.; Tran, T. D. Microstructural Characterization of Lithiated Graphite. *J. Electrochem. Soc.* **1996**, *143* (6), L120–L123.

- (297) Sivakkumar, S. R.; Nerkar, J. Y.; Pandolfo, A. G. Rate Capability of Graphite Materials as Negative Electrodes in Lithium-Ion Capacitors. *Electrochim. Acta* **2010**, *55* (9), 3330–3335.
- (298) Yao, F.; Güneş, F.; Ta, H. Q.; Lee, S. M.; Chae, S. J.; Sheem, K. Y.; Cojocaru, C. S.; Xie, S. S.; Lee, Y. H. Diffusion Mechanism of Lithium Ion through Basal Plane of Layered Graphene. *J. Am. Chem. Soc.* 2012, 134 (20), 8646–8654.
- (299) Zou, L.; Kang, F.; Li, X.; Zheng, Y.-P.; Shen, W.; Zhang, J. Investigations on the Modified Natural Graphite as Anode Materials in Lithium Ion Battery. *J. Phys. Chem. Solids* **2008**, *69* (5–6), 1265–1271.
- (300) Lee, J.; Kim, C.; Cheong, J. Y.; Kim, I.-D. An Angstrom-Level d-Spacing Control of Graphite Oxide Using Organofillers for High-Rate Lithium Storage. *Chem.* **2022**, *8* (9), 2393–2409.
- (301) Zhao, W.; Tan, P. H.; Liu, J.; Ferrari, A. C. Intercalation of Few-Layer Graphite Flakes with FeCl₃: Raman Determination of Fermi Level, Layer by Layer Decoupling, and Stability. *J. Am. Chem. Soc.* **2011**, 133 (15), 5941–5946.
- (302) Ma, J.; Yang, C.; Ma, X.; Liu, S.; Yang, J.; Xu, L.; Gao, J.; Quhe, R.; Sun, X.; Yang, J.; Pan, F.; Yang, X.; Lu, J. Improvement of Alkali Metal Ion Batteries via Interlayer Engineering of Anodes: From Graphite to Graphene. *Nanoscale* **2021**, *13* (29), 12521–12533.
- (303) Sonia, F. J.; Jangid, M. K.; Aslam, M.; Johari, P.; Mukhopadhyay, A. Enhanced and Faster Potassium Storage in Graphene with Respect to Graphite: A Comparative Study with Lithium Storage. *ACS Nano* **2019**, *13* (2), 2190–2204.
- (304) Qiu, T.; Yu, Z.; Xie, W.; He, Y.; Wang, H.; Zhang, T. Preparation of Onion-like Synthetic Graphite with a Hierarchical Pore Structure from Anthracite and Its Electrochemical Properties as the Anode Material of Lithium-Ion Batteries. *Energy Fuels* **2022**, *36* (15), 8256–8266.
- (305) Cheng, Q.; Yuge, R.; Nakahara, K.; Tamura, N.; Miyamoto, S. KOH Etched Graphite for Fast Chargeable Lithium-Ion Batteries. *J. Power Sources* **2015**, 284, 258–263.
- (306) Li, Y.; Liu, Q.; Li, W.; Meng, H.; Lu, Y.; Li, C. Synthesis and Supercapacitor Application of Alkynyl Carbon Materials Derived from CaC2 and Polyhalogenated Hydrocarbons by Interfacial Mechanochemical Reactions. ACS Appl. Mater. Interfaces 2017, 9 (4), 3895—3901.
- (307) Zhang, C.; Zhong, X.; Chen, P.; Sun, S.; Jiang, Y.; Yan, X. Facile Synthesis of Porous Graphite by Calcium Carbide and Nitrogen Gas for Lithium-Ion Batteries. *J. Energy Storage* **2023**, *66*, 107386.
- (308) Chen, J.; Zou, G.; Zhang, Y.; Song, W.; Hou, H.; Huang, Z.; Liao, H.; Li, S.; Ji, X. Activated Flake Graphite Coated with Pyrolysis Carbon as Promising Anode for Lithium Storage. *Electrochim. Acta* **2016**, *196*, 405–412.
- (309) Sharif, M.; Faghihi-Sani, M. A.; Golestani-Fard, F.; Saberi, A.; Soltani, A. K. Coating of Graphite Flakes with MgO/Carbon Nanocomposite via Gas State Reaction. *J. Alloy. Compd.* **2010**, *500* (1), 74–77.
- (310) Liu, H.; Gu, S.; Cao, H.; Li, X.; Li, Y. A Dense Packing Structure Constructed by Flake and Spherical Graphite: Simultaneously Enhanced in-Plane and through-Plane Thermal Conductivity of Polypropylene/Graphite Composites. *Compos. Commun.* **2020**, *19*, 25–29.
- (311) Tu, S.; Zhang, B.; Zhang, Y.; Chen, Z.; Wang, X.; Zhan, R.; Ou, Y.; Wang, W.; Liu, X.; Duan, X.; Wang, L.; Sun, Y. Fast-Charging Capability of Graphite-Based Lithium-Ion Batteries Enabled by Li₃P-Based Crystalline Solid-Electrolyte Interphase. *Nat. Energy* **2023**, 8 (12), 1365–1374.
- (312) Wang, H.; Yoshio, M.; Abe, T.; Ogumi, Z. Characterization of Carbon-Coated Natural Graphite as a Lithium-Ion Battery Anode Material. *J. Electrochem. Soc.* **2002**, *149* (4), A499–A503.
- (313) Du, P.; Fan, X.; Zhang, B.; Cao, L.; Ren, J.; Ou, X.; Guo, X.; Liu, Q. The Lithiophobic-to-Lithiophilic Transition on the Graphite towards Ultrafast-Charging and Long-Cycling Lithium-Ion Batteries. *Energy Storage Mater.* **2022**, *50*, 648–657.
- (314) Cheng, Y.; Lin, C.; Chu, Y.; Abouimrane, A.; Chen, Z.; Ren, Y.; Liu, C.; Tzeng, Y.; Auciello, O. Electrically Conductive Ultrananocrystalline Diamond-Coated Natural Graphite-Copper Anode

- for New Long Life Lithium-Ion Battery. Adv. Mater. 2014, 26 (22), 3724-3729.
- (315) Mundszinger, M.; Farsi, S.; Rapp, M.; Golla-Schindler, U.; Kaiser, U.; Wachtler, M. Morphology and Texture of Spheroidized Natural and Synthetic Graphites. *Carbon* **2017**, *111*, 764–773.
- (316) Billaud, J.; Bouville, F.; Magrini, T.; Villevieille, C.; Studart, A. R. Magnetically Aligned Graphite Electrodes for High-Rate Performance Li-Ion Batteries. *Nat. Energy* **2016**, *1* (8), 16097.
- (317) Zhang, L.; Zeng, M.; Wu, D.; Yan, X. Magnetic Field Regulating the Graphite Electrode for Excellent Lithium-Ion Batteries Performance. ACS Sustain. Chem. Eng. 2019, 7 (6), 6152–6160.
- (318) Poizot, P.; Laruelle, S.; Grugeon, S.; Dupont, L.; Tarascon, J.-M. Nano-Sized Transition-Metal Oxides as Negative-Electrode Materials for Lithium-Ion Batteries. *Nature* **2000**, 407 (6803), 496–499.
- (319) Gregorczyk, K. E.; Liu, Y.; Sullivan, J. P.; Rubloff, G. W. In Situ Transmission Electron Microscopy Study of Electrochemical Lithiation and Delithiation Cycling of the Conversion Anode RuO₂. ACS Nano **2013**, 7 (7), 6354–6360.
- (320) Xie, K.; Wu, P.; Zhou, Y.; Ye, Y.; Wang, H.; Tang, Y.; Zhou, Y.; Lu, T. Nitrogen-Doped Carbon-Wrapped Porous Single-Crystalline CoO Nanocubes for High-Performance Lithium Storage. *ACS Appl. Mater. Interfaces* **2014**, *6* (13), 10602–10607.
- (321) Liu, Y.; Zhao, Y.; Yu, Y.; Ahmad, M.; Sun, H. Facile Synthesis of Single-Crystal Mesoporous CoNiO₂ Nanosheets Assembled Flowers as Anode Materials for Lithium-Ion Batteries. *Electrochim. Acta* **2014**, *132*, 404–409
- (322) Wang, L.; Liang, W.; He, S.; Liu, M.; Zhao, Y.; Zhang, W.; Chen, Y.; Lai, X.; Bi, J.; Gao, D. Realization of Superior Electrochemical Performances for ZnMoO₄ Anode Material through the Construction Strategy of 3D Flower-like Single Crystalline. *J. Alloy. Compd.* **2020**, *816*, 152673.
- (323) Liu, X.; Zhang, T.; Qu, Y.; Tian, G.; Yue, H.; Zhang, D.; Feng, S. Carbonized Polydopamine Coated Single-Crystalline NiFe₂O₄ Nano-octahedrons with Enhanced Electrochemical Performance as Anode Materials in a Lithium Ion Battery. *Electrochim. Acta* **2017**, 231, 27–35.
- (324) Fang, S.; Bresser, D.; Passerini, S. Transition Metal Oxide Anodes for Electrochemical Energy Storage in Lithium- and Sodium-Ion Batteries. *Transition Metal Oxides for Electrochemical Energy Storage* **2022**, 55–99.
- (325) Zheng, M.; Tang, H.; Li, L.; Hu, Q.; Zhang, L.; Xue, H.; Pang, H. Hierarchically Nanostructured Transition Metal Oxides for Lithium-Ion Batteries. *Adv. Sci.* **2018**, *5* (3), 1700592.
- (326) Lu, X.; Zhao, L.; He, X.; Xiao, R.; Gu, L.; Hu, Y.; Li, H.; Wang, Z.; Duan, X.; Chen, L.; Maier, J.; Ikuhara, Y. Lithium Storage in Li₄Ti₅O₁₂ Spinel: The Full Static Picture from Electron Microscopy. *Adv. Mater.* **2012**, *24* (24), 3233–3238.
- (327) Ohzuku, T.; Ueda, A.; Yamamoto, N. Zero-Strain Insertion Material of $\text{Li}[\text{Li}_{1/3}\text{Ti}_{5/3}]\text{O}_4$ for Rechargeable Lithium Cells. *J. Electrochem. Soc.* **1995**, *142* (5), 1431–1435.
- (328) Tanaka, Y.; Ikeda, M.; Sumita, M.; Ohno, T.; Takada, K. First-Principles Analysis on Role of Spinel (111) Phase Boundaries in Li_{4+3x}Ti₅O₁₂ Li-Ion Battery Anodes. *Phys. Chem. Chem. Phys.: PCCP* **2016**, *18* (33), 23383–23388.
- (329) Aldon, L.; Kubiak, P.; Womes, M.; Jumas, J. C.; Olivier-Fourcade, J.; Tirado, J. L.; Corredor, J. I.; Perez Vicente, C. Chemical and Electrochemical Li-Insertion into the Li₄Ti₅O₁₂ Spinel. *Chem. Mater.* **2004**, *16* (26), 5721–5725.
- (330) Zhang, H.; Yang, Y.; Xu, H.; Wang, L.; Lu, X.; He, X. $\text{Li}_4\text{Ti}_5\text{O}_{12}$ Spinel Anode: Fundamentals and Advances in Rechargeable Batteries. *InfoMat* **2022**, *4* (4), No. e12228.
- (331) Lan, T.; Zhou, J.; Xie, T.; Huang, K.; Ong, S.; Yang, H.; Jiang, H.; Zeng, Y.; Zhang, H.; Guo, X.; Wan, L.; Zhang, Y.; Guo, H. PVA-Assisted Spray Deposited Porous $\text{Li}_4\text{Ti}_5\text{O}_{12}$ Thin Film as High-Rate and Long-Cycle Anode for Lithium-Ion Thin-Film Batteries. *J. Colloid Interface Sci.* **2024**, *676*, 1–12.
- (332) Zhang, J.; Feng, Q.; Cheng, W.; Zhang, L.; Huang, J.; Wang, Y.; Kong, X. In Situ Synthesis of Porous Plate-Like Li₄Ti₅O₁₂ Lithium-Ion Battery Anode with Advanced Li+ Storage Mechanism and Enhanced Electrochemical Kinetics. *Adv. Sustain. Syst.* **2023**, *7* (11), 2300243.

- (333) Li, Y.; Gao, H.; Yang, W. Enhancements of the Structures and Electrochemical Performances of $\text{Li}_4\text{Ti}_5\text{O}_{12}$ Electrodes by Doping with Non-Metallic Elements. *Electrochim. Acta* **2022**, *409*, 139993.
- (334) Lakshmi-Narayana, A.; Dhananjaya, M.; Julien, C. M.; Joo, S. W.; Ramana, C. V. Enhanced Electrochemical Performance of Rare-Earth Metal-Ion-Doped Nanocrystalline Li₄Ti₅O₁₂ Electrodes in High-Power Li-Ion Batteries. *ACS Appl. Mater. Interfaces* **2023**, *15* (17), 20925–20945.
- (335) Ye, J.; Ye, M.; Ye, W.; Feng, Z.; Xiong, D.; He, M. Zr-Doped Li₄Ti₅O₁₂ Particles Coated with Reduced Graphene Oxide Nanolayer as Anode for High-Rate Lithium-Ion Batteries. *J. Energy Storage* **2024**, *102*, 114165.
- (336) Pang, W. K.; Peterson, V. K.; Sharma, N.; Shiu, J.-J.; Wu, S. Lithium Migration in $\text{Li}_4\text{Ti}_5\text{O}_{12}$ Studied Using in Situ Neutron Powder Diffraction. *Chem. Mater.* **2014**, *26* (7), 2318–2326.
- (337) Lu, J.; Nan, C.; Peng, Q.; Li, Y. Single Crystalline Lithium Titanate Nanostructure with Enhanced Rate Performance for Lithium Ion Battery. *J. Power Sources* **2012**, 202, 246–252.
- (338) Chen, S.; Xin, Y.; Zhou, Y.; Ma, Y.; Zhou, H.; Qi, L. Self-Supported Li₄Ti₅O₁₂ Nanosheet Arrays for Lithium Ion Batteries with Excellent Rate Capability and Ultralong Cycle Life. *Energy Environ. Sci.* **2014**, *7* (6), 1924.
- (339) Pagani, F.; Stilp, E.; Pfenninger, R.; Reyes, E. C.; Remhof, A.; Balogh-Michels, Z.; Neels, A.; Sastre-Pellicer, J.; Stiefel, M.; Döbeli, M.; Rossell, M. D.; Erni, R.; Rupp, J. L. M.; Battaglia, C. Epitaxial Thin Films as a Model System for Li-Ion Conductivity in Li₄Ti₅O₁₂. ACS Appl. Mater. interfaces 2018, 10 (51), 44494–44500.
- (340) Jin, X.; Han, Y.; Zhang, Z.; Chen, Y.; Li, J.; Yang, T.; Wang, X.; Li, W.; Han, X.; Wang, Z.; Liu, X.; Jiao, H.; Ke, X.; Sui, M.; Cao, R.; Zhang, G.; Tang, Y.; Yan, P.; Jiao, S. Mesoporous Single-Crystal Lithium Titanate Enabling Fast-Charging Li-Ion Batteries. *Adv. Mater.* 2022, 34 (18), No. e2109356.
- (341) Song, Z.; Li, H.; Liu, W.; Zhang, H.; Yan, J.; Tang, Y.; Huang, J.; Zhang, H.; Li, X. Ultrafast and Stable Li-(De)Intercalation in a Large Single Crystal H-Nb₂O₅ Anode via Optimizing the Homogeneity of Electron and Ion Transport. *Adv. Mater.* **2020**, *32* (22), No. e2001001.
- (342) Huang, H.; Kuai, H.; Ding, X.; Hu, B.; Chen, Y.; Zhou, Q.; Xiong, X. Single Crystal H-Nb $_2O_5$ Growing along the [001] Crystal Direction for Ultrafast Lithium Storage. *J. Mater. Chem. A* **2023**, *11* (2), 642–648.
- (343) Griffith, K. J.; Wiaderek, K. M.; Cibin, G.; Marbella, L. E.; Grey, C. P. Niobium Tungsten Oxides for High-Rate Lithium-Ion Energy Storage. *Nature* **2018**, *559* (7715), *556*–*563*.
- (344) Guo, Y.; Guo, C.; Li, P.; Song, W.; Huang, W.; Yan, J.; Liao, X.; He, K.; Sha, W.; Zeng, X.; Tang, X.; Ren, Q.; Wang, S.; Amine, K.; Nie, A.; Liu, T.; Yuan, Y. Improving the Fast-Charging Capability of NbWO-Based Li-Ion Batteries. *Nat. Commun.* **2025**, *16* (1), 2441.
- (345) Wang, S.; Zhao, L.; Dong, Y.; Zhu, H.; Yang, Y.; Xu, H.; Wang, B.; Yuan, Y.; Ren, Y.; Huang, X.; Quan, W.; Li, Y.; Huang, Y.; Settens, C. M.; He, Q.; Sun, Y.; Wang, H.; Xiao, Z.; Liu, W.; Xiao, X.; Fu, R.; Li, Q.; Chu, Y. S.; Zhang, Z.; Liu, Q.; Minor, A. M.; Zhang, J.; Tang, Z.; Li, J. Pre-Zeolite Framework Super-MIEC Anodes for High-Rate Lithium-Ion Batteries. *Energy Environ. Sci.* 2023, 16 (1), 241–251.
- (346) Liu, H.; Zhu, Z.; Yan, Q.; Yu, S.; He, X.; Chen, Y.; Zhang, R.; Ma, L.; Liu, T.; Li, M.; Lin, R.; Chen, Y.; Li, Y.; Xing, X.; Choi, Y.; Gao, L.; Cho, H. S.; An, K.; Feng, J.; Kostecki, R.; Amine, K.; Wu, T.; Lu, J.; Xin, H. L.; Ong, S. P.; Liu, P. A Disordered Rock Salt Anode for Fast-Charging Lithium-Ion Batteries. *Nature* 2020, 585 (7823), 63–67.
- (347) Lu, W.; Lieber, C. M. Nanoelectronics from the Bottom Up. *Nat. Mater.* **2007**, *6* (11), 841–850.
- (348) Yu, H.-D.; Regulacio, M. D.; Ye, E.; Han, M.-Y. Chemical Routes to Top-down Nanofabrication. *Chem. Soc. Rev.* **2013**, 42 (14), 6006–6018.
- (349) Ghalehbandi, S. M.; Malaki, M.; Gupta, M. Accumulative Roll Bonding—A Review. *Appl. Sci.* **2019**, *9* (17), 3627.
- (350) Saito, Y.; Utsunomiya, H.; Tsuji, N.; Sakai, T. Novel Ultra-High Straining Process for Bulk Materials—Development of the Accumulative Roll-Bonding (ARB) Process. *Acta Mater.* **1999**, 47 (2), 579–583.

- (351) Chen, Y.; Wang, Z.; Li, X.; Yao, X.; Wang, C.; Li, Y.; Xue, W.; Yu, D.; Kim, S. Y.; Yang, F.; Kushima, A.; Zhang, G.; Huang, H.; Wu, N.; Mai, Y.-W.; Goodenough, J. B.; Li, J. Li Metal Deposition and Stripping in a Solid-State Battery via Coble Creep. *Nature* **2020**, *578* (7794), 251–255.
- (352) Tan, J.; Ma, L.; Yi, P.; Wang, Y.; Li, Z.; Fang, Z.; Li, X.; He, S.; Wang, X.; Ye, M.; Shen, J. Scalable Customization of Crystallographic Plane Controllable Lithium Metal Anodes for Ultralong-Lasting Lithium Metal Batteries. *Adv. Mater.* **2024**, *36* (30), No. e2403570.
- (353) Zheng, J.; Deng, Y.; Yin, J.; Tang, T.; Garcia-Mendez, R.; Zhao, Q.; Archer, L. A. Textured Electrodes: Manipulating Built-In Crystallographic Heterogeneity of Metal Electrodes via Severe Plastic Deformation. *Adv. Mater.* **2022**, 34 (1), No. e2106867.
- (354) Wang, H.; Liu, Y.; Zhu, M.; Chen, Y.; Chen, D.; Lin, Z.; Wang, K.; Xu, Z.; Chen, S.; Xing, G.; Malyi, O. I.; Tang, Y.; Zhang, Y. Emulating "Curvature-Enhanced Adsorbate Coverage" for Superconformal and Orientated Zn Electrodeposition in Zinc-ion-Batteries. *Angew. Chem., Int. Ed.* **2025**, *64* (2), No. e202414473.
- (355) Wang, Y.; Chen, M.; Zhou, F.; Ma, E. High Tensile Ductility in a Nanostructured Metal. *Nature* **2002**, *419* (6910), 912–915.
- (356) Jin, S.; Huang, M.; Kwon, Y.; Zhang, L.; Li, B.-W.; Oh, S.; Dong, J.; Luo, D.; Biswal, M.; Cunning, B. V.; Bakharev, P. V.; Moon, I.; Yoo, W. J.; Camacho-Mojica, D. C.; Kim, Y.-J.; Lee, S. H.; Wang, B.; Seong, W. K.; Saxena, M.; Ding, F.; Shin, H.-J.; Ruoff, R. S. Colossal Grain Growth Yields Single-Crystal Metal Foils by Contact-Free Annealing. *Science* 2018, 362 (6418), 1021–1025.
- (357) Chen, Z.; Wu, Q.; Han, X.; Wang, C.; Chen, J.; Hu, T.; He, Q.; Zhu, X.; Yuan, D.; Chen, J.; Zhang, Y.; Yang, L.; Ma, Y.; Zhao, J. Converting Commercial Zn Foils into Single (002)-Textured Zn with Millimeter-Sized Grains for Highly Reversible Aqueous Zinc Batteries. *Angew. Chem.* **2024**, *136* (17), No. e202401507.
- (358) Shen, T.; Wei, T.; Zhang, S.; Liu, H.; Li, C.; Li, Z.; Yang, M.; Liu, C.; Pei, Y. Single-Crystalline Zn(002) Facet Enables Ultrastable Anode-Electrolyte Interface. *Small Struct.* **2025**, *6* (1), 2400325.
- (359) Hao, Z.; Li, G.; Zheng, C.; Liu, X.; Wu, S.; Li, H.; Zhang, K.; Yan, Z.; Chen, J. The Dependence of Solid Electrolyte Interphase on the Crystal Facet of Current Collector in Li Metal Battery. *Angew. Chem.* **2024**, 136 (37), No. e202407064.
- (360) Song, X.; Bai, L.; Wang, C.; Wang, D.; Xu, K.; Dong, J.; Li, Y.; Shen, Q.; Yang, J. Synergistic Cooperation of Zn(002) Texture and Amorphous Zinc Phosphate for Dendrite-Free Zn Anodes. *ACS Nano* **2023**, *17* (15), 15113–15124.
- (361) Chen, S.; Ouyang, K.; Liu, Y.; Cui, M.; Pu, G.; Wang, Y.; Zhang, K.; Huang, Y. Non-Epitaxial Electrodeposition of Overall 99% (002) Plane Achieves Extreme and Direct Utilization of 95% Zn Anode and By-Product as Cathode. *Angew. Chem., Int. Ed.* **2024**, 63 (42), No. e202409303.
- (362) Wang, X.; Meng, J.; Lin, X.; Yang, Y.; Zhou, S.; Wang, Y.; Pan, A. Stable Zinc Metal Anodes with Textured Crystal Faces and Functional Zinc Compound Coatings. *Adv. Funct. Mater.* **2021**, *31* (48), 2106114.
- (363) Liu, Y.; Hu, J.; Lu, Q.; Hantusch, M.; Zhang, H.; Qu, Z.; Tang, H.; Dong, H.; Schmidt, O. G.; Holze, R.; Zhu, M. Highly Enhanced Reversibility of a Zn Anode by In-Situ Texturing. *Energy Storage Mater.* **2022**, *47*, 98–104.
- (364) Zhang, Y.; Han, X.; Liu, R.; Yang, Z.; Zhang, S.; Zhang, Y.; Wang, H.; Cao, Y.; Chen, A.; Sun, J. Manipulating the Zinc Deposition Behavior in Hexagonal Patterns at the Preferential Zn (100) Crystal Plane to Construct Surficial Dendrite-Free Zinc Metal Anode. *Small* **2022**, *18* (7), No. e2105978.
- (365) Ma, X.; Meng, Z.; Bellonia, M. V.; Spangenberger, J.; Harper, G.; Gratz, E.; Olivetti, E.; Arsenault, R.; Wang, Y. The Evolution of Lithium-Ion Battery Recycling. *Nat. Rev. Clean Technol.* **2025**, *1* (1), 75–94.
- (366) Zhao, Y.; Kang, Y.; Wozny, J.; Lu, J.; Du, H.; Li, C.; Li, T.; Kang, F.; Tavajohi, N.; Li, B. Recycling of Sodium-Ion Batteries. *Nat. Rev. Mater.* **2023**, 8 (9), 623–634.
- (367) Tan, D. H. S.; Xu, P.; Yang, H.; Kim, M.; Nguyen, H.; Wu, E. A.; Doux, J.-M.; Banerjee, A.; Meng, Y. S.; Chen, Z. Sustainable Design of

- Fully Recyclable All Solid-State Batteries. MRS Energy Sustain. 2020, 7 (1), 23.
- (368) Machala, M. L.; Chen, X.; Bunke, S. P.; Forbes, G.; Yegizbay, A.; de Chalendar, J. A.; Azevedo, I. L.; Benson, S.; Tarpeh, W. A. Life Cycle Comparison of Industrial-Scale Lithium-Ion Battery Recycling and Mining Supply Chains. *Nat. Commun.* **2025**, *16* (1), 988.
- (369) Yu, X.; Li, W.; Gupta, V.; Gao, H.; Tran, D.; Sarwar, S.; Chen, Z. Current Challenges in Efficient Lithium-Ion Batteries' Recycling: A Perspective. *Glob. Chall.* **2022**, *6* (12), 2200099.
- (370) Wang, X.; Gaustad, G.; Babbitt, C. W. Targeting High Value Metals in Lithium-Ion Battery Recycling via Shredding and Size-Based Separation. *Waste Manag.* **2016**, *51*, 204–213.
- (371) Sommerville, R.; Shaw-Stewart, J.; Goodship, V.; Rowson, N.; Kendrick, E. A Review of Physical Processes Used in the Safe Recycling of Lithium Ion Batteries. *Sustain. Mater. Technol.* **2020**, 25, No. e00197. (372) Gupta, V.; Appleberry, M.; Li, W.; Chen, Z. Direct Recycling
- Industrialization of Li-Ion Batteries: The Pre-Processing Barricade. *Next Energy* **2024**, *2*, 100091.
- (373) Rajaeifar, M. A.; Raugei, M.; Steubing, B.; Hartwell, A.; Anderson, P. A.; Heidrich, O. Life Cycle Assessment of Lithium-ion Battery Recycling Using Pyrometallurgical Technologies. *J. Ind. Ecol.* **2021**, 25 (6), 1560–1571.
- (374) Makuza, B.; Tian, Q.; Guo, X.; Chattopadhyay, K.; Yu, D. Pyrometallurgical Options for Recycling Spent Lithium-Ion Batteries: A Comprehensive Review. *J. Power Sources* **2021**, *491*, 229622.
- (375) Liang, Z.; Cai, C.; Peng, G.; Hu, J.; Hou, H.; Liu, B.; Liang, S.; Xiao, K.; Yuan, S.; Yang, J. Hydrometallurgical Recovery of Spent Lithium Ion Batteries: Environmental Strategies and Sustainability Evaluation. ACS Sustain. Chem. Eng. 2021, 9 (17), 5750–5767.
- (376) Dalini, E. A.; Karimi, Gh.; Zandevakili, S.; Goodarzi, M. A Review on Environmental, Economic and Hydrometallurgical Processes of Recycling Spent Lithium-Ion Batteries. *Miner. Process. Extr. Met. Rev.* **2021**, *42* (7), 451–472.
- (377) Kim, D.; Joo, H.; Kim, C.; Kim, S.; Kim, W.-Y.; Han, S.; Park, J.; Park, S.; Jung, H.; Park, S.; Kwon, K. A Comprehensive Review on the Resynthesis of Ternary Cathode Active Materials from the Leachate of Li-Ion Batteries. *J. Energy Chem.* **2024**, *95*, 446–463.
- (378) Chen, M.; Zheng, Z.; Wang, Q.; Zhang, Y.; Ma, X.; Shen, C.; Xu, D.; Liu, J.; Liu, Y.; Gionet, P.; O'Connor, I.; Pinnell, L.; Wang, J.; Gratz, E.; Arsenault, R.; Wang, Y. Closed Loop Recycling of Electric Vehicle Batteries to Enable Ultra-High Quality Cathode Powder. Sci. Rep. 2019, 9 (1), 1654.
- (379) Zheng, Z.; Chen, M.; Wang, Q.; Zhang, Y.; Ma, X.; Shen, C.; Xu, D.; Liu, J.; Liu, Y.; Gionet, P.; O'Connor, I.; Pinnell, L.; Wang, J.; Gratz, E.; Arsenault, R.; Wang, Y. High Performance Cathode Recovery from Different Electric Vehicle Recycling Streams. ACS Sustain. Chem. Eng. 2018, 6 (11), 13977–13982.
- (380) Xu, P.; Tan, D. H. S.; Jiao, B.; Gao, H.; Yu, X.; Chen, Z. A Materials Perspective on Direct Recycling of Lithium-Ion Batteries: Principles, Challenges and Opportunities. *Adv. Funct. Mater.* **2023**, 33 (14), 2213268.
- (381) Gao, H.; Tran, D.; Chen, Z. Seeking Direct Cathode Regeneration for More Efficient Lithium-Ion Battery Recycling. *Curr. Opin. Electrochem.* **2022**, *31*, 100875.
- (382) Gao, H.; Yan, Q.; Xu, P.; Liu, H.; Li, M.; Liu, P.; Luo, J.; Chen, Z. Efficient Direct Recycling of Degraded LiMn₂O₄ Cathodes by One-Step Hydrothermal Relithiation. *ACS Appl. Mater. Interfaces* **2020**, *12* (46), 51546–51554.
- (383) Gupta, V.; Yu, X.; Gao, H.; Brooks, C.; Li, W.; Chen, Z. Scalable Direct Recycling of Cathode Black Mass from Spent Lithium-Ion Batteries. *Adv. Energy Mater.* **2023**, *13* (6), 2203093.
- (384) Yu, X.; Yu, S.; Lin, J.; Gupta, V.; Gao, H.; Li, W.; Appleberry, M.; Liu, P.; Chen, Z. Multifunctional Scavenger Boosts Cathode Interfacial Stability with Reduced Water Footprint for Direct Recycling of Spent Lithium-Ion Batteries. *Adv. Mater.* **2024**, *36* (41), No. e2408463.
- (385) Li, Y.; Lv, W.; Zhao, H.; Xie, Y.; Ruan, D.; Sun, Z. Regeneration of Anode Materials from Complex Graphite Residue in Spent Lithium-Ion Battery Recycling Process. *Green Chem.* **2022**, 24 (23), 9315–9328.

- (386) Abdollahifar, M.; Doose, S.; Cavers, H.; Kwade, A. Graphite Recycling from End-of-Life Lithium-Ion Batteries: Processes and Applications. *Adv. Mater. Technol.* **2023**, *8* (2), 220368.
- (387) Chen, W.; Salvatierra, R. V.; Li, J. T.; Kittrell, C.; Beckham, J. L.; Wyss, K. M.; La, N.; Savas, P. E.; Ge, C.; Advincula, P. A.; Scotland, P.; Eddy, L.; Deng, B.; Yuan, Z.; Tour, J. M. Flash Recycling of Graphite Anodes. *Adv. Mater.* **2023**, 35 (8), No. e2207303.
- (388) Li, T.; Tao, L.; Xu, L.; Meng, T.; Clifford, B. C.; Li, S.; Zhao, X.; Rao, J.; Lin, F.; Hu, L. Direct and Rapid High-Temperature Upcycling of Degraded Graphite. *Adv. Funct. Mater.* **2023**, *33* (43), 2302951.
- (389) Niu, B.; Xiao, J.; Xu, Z. Advances and Challenges in Anode Graphite Recycling from Spent Lithium-Ion Batteries. *J. Hazard. Mater.* **2022**, 439, 129678.
- (390) Rey, I.; Vallejo, C.; Santiago, G.; Iturrondobeitia, M.; Lizundia, E. Environmental Impacts of Graphite Recycling from Spent Lithium-Ion Batteries Based on Life Cycle Assessment. *ACS Sustain. Chem. Eng.* **2021**, *9* (43), 14488–14501.
- (391) Gao, H.; Yan, Q.; Tran, D.; Yu, X.; Liu, H.; Li, M.; Li, W.; Wu, J.; Tang, W.; Gupta, V.; Luo, J.; Chen, Z. Upcycling of Spent LiNi_{0,33}Co_{0,33}Mn_{0,33}O₂ to Single-Crystal Ni-Rich Cathodes Using Lean Precursors. *ACS Energy Lett.* **2023**, *8* (10), 4136–4144.
- (392) Wang, J.; Jia, K.; Ma, J.; Liang, Z.; Zhuang, Z.; Zhao, Y.; Li, B.; Zhou, G.; Cheng, H.-M. Sustainable Upcycling of Spent LiCoO₂ to an Ultra-Stable Battery Cathode at High Voltage. *Nat. Sustain.* **2023**, 6 (7), 797–805.